



# **THERMAL TRANSPORT OF NANOFUIDS IN A MINICHANNEL**

A Dissertation

Presented to

the Faculty of the Department of Mechanical Engineering

University of Houston

In Partial Fulfillment

of the Requirements for the Degree

Doctor of Philosophy

in Mechanical Engineering

by

Leyuan Yu

August 2012

# THERMAL TRANSPORT OF NANOFUIDS IN A MINICHANNEL

---

Leyuan Yu

Approved:

---

Chair of Committee  
Dong Liu, Assistant Professor,  
Mechanical Engineering

Committee Members:

---

Larry C. Witte, Professor,  
Mechanical Engineering

---

Ralph Metcalfe, Professor,  
Mechanical Engineering

---

Ashutosh Agrawal, Assistant Professor,  
Mechanical Engineering

---

Manolis Doxastakis, Assistant Professor,  
Chemical and Biomolecular Engineering

---

Suresh K. Khator, Associate Dean,  
Cullen College of Engineering

---

Pradeep Sharma, Professor and Chair,  
Mechanical Engineering

## ACKNOWLEDGEMENTS

I gratefully acknowledge the financial support from the University of Houston, the Cooling Technologies Research Center (a National Science Foundation Industry/University Cooperative Research Center) at Purdue University and the National Science Foundation (Grant No. 0927340).

I would like to thank the members of my advisory committee, Professor Larry C. Witte, Professor Ralph Metcalfe, Professor Ashutosh Agrawal and Professor Manolis Doxastakis for their time and contributions. Also, I would like to thank Dr. Hollingsworth for his advice and help.

I would like to thank my dear friends and fellow graduate colleagues for their friendship and help. I want to thank Aritra Sur, Guoliang He, Shuangqi Song, Mircea Ionescu, and Holley Love with whom I have had the pleasure of working with during my stay at the University of Houston.

I would like to express my sincere gratitude to my advisor, Dr. Dong Liu, for his great guidance and constant encouragement during my graduate study. He has been such a dedicated mentor, and his professionalism will play a very important role in my future career.

Finally, I am especially grateful to my family, my parents, and parents in law for their support and dedication. In particular, I would like to thank my wife, Jing, for her tremendous love, companionship, encouragement and support over these years.

# **THERMAL TRANSPORT OF NANOFUIDS IN A MINICHANNEL**

An Abstract

of a

Dissertation

Presented to

the Faculty of the Department of Mechanical Engineering

University of Houston

In Partial Fulfillment

of the Requirements for the Degree

Doctor of Philosophy

in Mechanical Engineering

by

Leyuan Yu

August 2012

## ABSTRACT

Nanofluids have been proposed as a promising candidate for advanced heat transfer fluids in a variety of important engineering applications ranging from energy storage, electronics cooling to thermal processing of materials. However, the thermal transport mechanisms for nanofluids are far from being well understood. In particular, a consensus is lacking on if and how the dispersed nanoparticles alter the single-phase and two-phase heat transfer mechanisms of nanofluids in forced convective flows, and the applicability of established fluid mechanics and heat transfer theories for predicting thermal transport of nanofluids has also been called into question.

The present research aims at conducting a systematic study of single-phase convective heat transfer and two-phase flow boiling of nanofluids in a circular minichannel. The goals are to experimentally characterize the effective thermophysical properties, pressure drop and heat transfer behaviors of nanofluids with respect to their constituent base fluids, and to explore the effects of the particle-fluid interactions on the convective transport physics in nanofluids.

In this work, both aqueous  $\text{Al}_2\text{O}_3$ -water and non-aqueous  $\text{Al}_2\text{O}_3$ -Polyalphaolefin (PAO) nanofluids were synthesized. The effective thermophysical properties of the nanofluids, especially the viscosity and thermal conductivity, were first measured and compared to predictions from the effective medium theories (EMTs). Special attention was given to the effects of the nanoparticle size and aspect ratio, the aggregation and the dispersion state of the nanoparticles. Once these effects were considered properly, no abnormal changes were found in the effective thermophysical properties of nanofluids. Then, an experimental investigation was conducted to study the single-phase forced

convective heat transfer of the nanofluids through a circular minichannel. The friction factor and convective heat transfer coefficient were measured for the nanofluids over a wide range of Reynolds number, covering the laminar, transition and early stage of fully developed turbulent flows. Some interesting phenomena were observed, such as the developing flow behaviors and delayed transition to turbulence for  $\text{Al}_2\text{O}_3$ -water nanofluids, and the *abnormal* heat transfer characteristics of  $\text{Al}_2\text{O}_3$ -PAO nanofluids, which can be attributed to the nanoparticle-fluid interaction and the shear-induced alignment and orientational motion of nanoparticles. Based on the convective heat transfer experimental data, the thermal performance and effectiveness of nanofluids for practical cooling applications were critically evaluated using different figures of merit (FOM), and it was found the nanofluids do not offer any enhanced thermal performance when the increased pumping power consumption and the negative effect of reduced specific heat on heat transfer are taken into account. And lastly, convective flow boiling and two-phase flow of  $\text{Al}_2\text{O}_3$ -water nanofluids were studied with an emphasis on the effect of nanoparticle deposition on two-phase flow instabilities. It was discovered the onset of flow instabilities can be suppressed by the nanofluids.

# TABLE OF CONTENTS

Acknowledgements.....	iv
Abstract.....	v
Table of Contents.....	viii
List of Figures.....	xii
List of Tables .....	xviii
<b>Chapter 1. Introduction .....</b>	<b>1</b>
<b>Chapter 2. Nanofluids Synthesis and Characterization.....</b>	<b>4</b>
2.1 Nanofluids Synthesis .....	4
2.2 Geometrical Characterization of Nanofluids .....	6
2.3 Thermophysical Properties of Nanofluids .....	9
2.3.1 Viscosity .....	10
2.3.1.1 Theory.....	10
2.3.1.2 Experimental results.....	13
2.3.2 Thermal Conductivity .....	17
2.3.2.1 Theory .....	17
2.3.2.2 Experimental Results .....	18
2.3.2.3 Further Discussion .....	20
2.4 Summary.....	25

<b>Chapter 3. Single-Phase Thermal Transport of Aqueous Nanofluids in a</b>	
<b>Minichannel .....</b>	<b>26</b>
3.1 Literature Survey .....	26
3.2 Convective Flow and Heat Transfer .....	40
3.2.1 Experimental Apparatus.....	40
3.2.2 Test Procedures .....	41
3.2.3 Data Reduction.....	42
3.2.4 Measurement Uncertainties .....	43
3.2.5 Experimental Results with Water .....	44
3.2.6 Experimental Results for Al <sub>2</sub> O <sub>3</sub> -water Nanofluids .....	50
3.3 Summary .....	58
<b>Chapter 4. Single-Phase Thermal Transport of Al<sub>2</sub>O<sub>3</sub>-PAO Nanofluids in a</b>	
<b>Minichannel .....</b>	<b>60</b>
4. 1 Introduction.....	60
4. 2 Experiments .....	63
4. 2.1 Experimental Results for PAO.....	64
4. 2.2 Experimental Results for Al <sub>2</sub> O <sub>3</sub> -PAO Nanofluids.....	66
4.3 Summary.....	75
<b>Chapter 5. Thermal Effectiveness of Laminar Forced Convection of Nanofluids ..</b>	<b>76</b>
5.1 Introduction.....	76
5.2 Selection Criteria of Coolants.....	78

5.3 Thermal Performance of Nanofluids .....	82
5.4 Summary .....	101
<b>Chapter 6. Flow Boiling Heat Transfer in A Minichannel .....</b>	<b>103</b>
6.1 Introduction.....	103
6.2 General Features of Flow Boiling Heat Transfer.....	110
6.3 Flow Boiling Heat Transfer Experiments.....	111
6.3.1 Experimental Apparatus.....	111
6.3.2 Preparation of Nanofluids .....	114
6.3.3 Contact angle Measurement.....	114
6.3.4 Test Procedures .....	116
6.3.5 Data Reduction.....	117
6.4 Experimental Results .....	119
6.4.1 Boiling Curves .....	119
6.4.2 Pressure Drop.....	121
6.4.3 Onset Nucleate of Boiling.....	123
6.4.4 Analytical Model for ONB .....	125
6.5 Two-Phase Flow Instability .....	131
6.5.1 Classifications of Two-phase Flow Instabilities .....	132
6.5.1.1 Density-wave Oscillations .....	136
6.5.1.2 Pressure-drop Type Oscillations.....	136

6.5.1.3 Thermal Oscillations.....	137
6.5.2 Two-phase Flow Instability .....	139
6.6 Summary.....	151
<b>Chapter 7. Conclusions and Future Work .....</b>	<b>153</b>
<b>References.....</b>	<b>156</b>

## LIST OF FIGURES

Figure 2. 1. Effective particle size versus sonication time .....	8
Figure 2. 2. DLS measurement of effective particle size.....	8
Figure 2. 3. TEM of Al <sub>2</sub> O <sub>3</sub> nanorods. ....	9
Figure 2. 4. Effective viscosity of nanofluid at various volume concentrations at 25°C. 14	
Figure 2. 5. The effective viscosity of nanofluids at various nanoparticle .....	16
Figure 2. 6. Effective thermal conductivity of nanofluid at various temperatures .....	19
Figure 2. 7. The effective thermal conductivity of NF1 as a function of nanoparticle volume fraction .....	21
Figure 2. 8. The effective thermal conductivity of NF2 as a function of nanoparticle volume fraction. ....	22
Figure 2. 9. Four possible particle configurations in particle suspensions. ....	22
Figure 2. 10. Effective thermal conductivity for various particle configurations.....	24
Figure 2. 11. Shear-induced alignment of rod-like nanoparticles in convective flow through a channel.....	25
Figure 3. 1. Schematic of the experimental apparatus.....	40
Figure 3. 2. Friction factor vs. Reynolds number (water).....	45
Figure 3. 3. Local Nusselt number vs. the $x^*$ (water, heat flux $q'' = 6.5 \text{ kW/m}^2$ ).....	46
Figure 3. 4. Average Nusselt number vs. Reynolds number .....	48

Figure 3. 5. Friction factor vs. Reynolds number for nanofluids at various volume concentrations .....	51
Figure 3. 6. Local convective heat transfer of nanofluids (heat flux $q'' = 6.5 \text{ kW/m}^2$ )...	54
Figure 3. 7. Average Nusselt number vs. Reynolds number in the laminar flow region..	55
Figure 3. 8. Average Nusselt number vs. Reynolds number in the transition and turbulent flow regions (heat flux $q'' = 6.5 \text{ kW/m}^2$ ). .....	57
Figure 3. 9. Average Nusselt number versus Reynolds number over the entire flow range (nanofluids, heat flux $q''=6.5 \text{ kW/m}^2$ ).....	58
Figure 4. 1. Friction factor of PAO versus Reynolds number. ....	64
Figure 4. 2. Local Nusselt number for PAO versus $x^*$ (heat flux $q'' = 6.5 \text{ kW/m}^2$ ).....	65
Figure 4. 3. Pressure drop across the minichannel versus flow rate.....	66
Figure 4. 4. Friction factor of nanofluids as a function of Reynolds number.....	67
Figure 4. 5. Local convective heat transfer of PAO (heat flux $q'' = 6.5 \text{ kW/m}^2$ ). ....	69
Figure 4. 6. Local Nusselt number for NF1 as a function of $x^*$ (heat flux $q'' = 6.5 \text{ kW/m}^2$ ) for: (a) 0.65 v%, and (b) 1.3 v%. .....	73
Figure 4. 7. Local Nusselt number for NF2 as a function of $x^*$ (heat flux $q''= 6.5 \text{ kW/m}^2$ ) for: (a) 0.65 v%, and (b) 1.3 v%. .....	74
Figure 5. 1. Effective thermophysical properties of nanofluids (shown as the ratio to those of the base fluids): (a) $\text{Al}_2\text{O}_3$ -water nanofluids, and (b) $\text{Al}_2\text{O}_3$ -PAO nanofluids. ....	85

Figure 5. 2. Evaluation of $(FOM)_h$ of $Al_2O_3$ -water nanofluids presented in terms of convective heat transfer coefficient using different bases of comparison: (a) $Q$ -based; (b) $Re$ -based and (c) $P$ -based (heat flux $q'' = 6.5 \text{ kW/m}^2$ ).....	86
Figure 5. 3. Evaluation of $(FOM)_T$ of $Al_2O_3$ -water nanofluids presented in terms of $(T_{w,o} - T_{in})$ using different bases of comparison: (a) $Q$ -based and (b) $P$ -based .....	89
Figure 5. 4. Evaluation of $(FOM)_p$ of $Al_2O_3$ -water nanofluids presented in terms of $c_p h / P$ using different bases of comparison: (a) $Q$ -based and (b) $P$ -based .....	91
Figure 5. 5. Evaluation of $(FOM)_Q$ of $Al_2O_3$ -water nanofluids presented in terms of $q / P$ using different bases of comparison: (a) $Q$ -based and (b) $P$ -based .....	92
Figure 5. 6. Evaluation of $(FOM)_h$ of $Al_2O_3$ -PAO nanofluids presented in terms of convective heat transfer coefficient using different bases of comparison: (a) $Q$ -based; (b) $Re$ -based and (c) $P$ -based (heat flux $q'' = 6.5 \text{ kW/m}^2$ ).....	94
Figure 5. 7. Evaluation of $(FOM)_T$ of $Al_2O_3$ -PAO nanofluids presented in terms of $(T_{w,o} - T_{in})$ using different bases of comparison: (a) $Q$ -based; (b) $Re$ -based and (c) $P$ -based (heat flux $q'' = 6.5 \text{ kW/m}^2$ ).....	96
Figure 5. 8. Assessment of $(FOM)_p$ of $Al_2O_3$ -PAO nanofluids presented in terms of $c_p h / P$ using different bases of comparison: (a) $Q$ -based; (b) $Re$ -based and (c) $P$ -based (heat flux $q'' = 6.5 \text{ kW/m}^2$ ).....	98

Figure 5. 9. Assessment of $(FOM)_Q$ of $Al_2O_3$ -PAO nanofluids presented in terms of $q/P$ using different bases of comparison: (a) $Q$ -based; (b) $Re$ -based and (c) $P$ -based (heat flux $q'' = 6.5 \text{ kW/m}^2$ ).....	100
Figure 6. 1. Boiling curve. ....	110
Figure 6.2. Schematic of experimental apparatus for flow boiling.....	112
Figure 6. 3. PID-regulated preheater for inlet subcooling control. ....	112
Figure 6. 4. Temporal variation of the inlet fluid temperature after running through the PID-regulated preheater (131.3mL/min). ....	113
Figure 6. 5. Oxygen concentration and temperature of water variation with time. ....	115
Figure 6. 6. Contact angle measurements on a stainless steel surface for (a) water, (b) 0.01 v% $Al_2O_3$ -water nanofluid, and (c) 0.1 v% $Al_2O_3$ -water nanofluid. ....	116
Figure 6. 7. Heat loss in experiment estimated from single phase data ( $G = 1374.7 \text{ kg/m}^2\text{s}$ , $T_{f,in} = 80.8^\circ\text{C}$ ). ....	118
Figure 6. 8. Boiling curves for: (a) water, (b) 0.01 v% nanofluid, and (c) 0.1 v% nanofluid.....	120
Figure 6. 9. Two-phase pressure drop of (a) water and (b) nanofluids.....	122
Figure 6. 10. Comparison of Boiling curve. ....	124
Figure 6. 11. Distribution of nucleation sites on a boiling surface before (a) and after (b) deposition of nanoparticles. ....	125

Figure 6. 12. Onset of nucleate boiling (a) an embryo bubble residing on the cavity, and (b) ONB superheat criterion.....	128
Figure 6. 13. Size range of active nucleation sites as a function of wall temperature for different contact angles.....	131
Figure 6. 14. Ledinegg instability.....	133
Figure 6. 15. Density wave type oscillations.....	137
Figure 6. 16. Pressure-drop type oscillations.....	138
Figure 6. 17. Oscillation boundaries.....	139
Figure 6. 18. Different parameters of water variation with time at $G = 2038.7 \text{ kg/m}^2\text{s}$ , $T_{in}=92.3 \text{ }^\circ\text{C}$ , $q''=29.9 \text{ W/cm}^2$ .....	141
Figure 6. 19. Pressure-drop type oscillations of water at $G = 1054.4 \text{ kg/m}^2\text{s}$ , $T_{in}=91.9 \text{ }^\circ\text{C}$ , $q''=29.9 \text{ W/cm}^2$ .....	142
Figure 6. 20. Different parameters of 0.01 v% nanofluids variation with time at $G = 2007.4 \text{ kg/m}^2\text{s}$ , $T_{in} = 92.3^\circ\text{C}$ , $q''=29.9 \text{ W/cm}^2$ (stable region).....	143
Figure 6. 21. Two-phase flow oscillations of 0.01 v% nanofluids at $G = 1052.4 \text{ kg/m}^2\text{s}$ , $T_{in} = 92.7^\circ\text{C}$ , $q''=29.9 \text{ W/cm}^2$ .....	144
Figure 6. 22. Different parameters of 0.1 v% nanofluids variation with time at $G=2028.5 \text{ kg/m}^2\text{s}$ , $T_{in}=92.3 \text{ }^\circ\text{C}$ , $q''=29.9 \text{ W/cm}^2$ (stable region).....	145
Figure 6. 23. Two-phase flow oscillations of 0.1 v% nanofluids at $G = 1065.9 \text{ kg/m}^2\text{s}$ ,.....	146
Figure 6. 24. Two-phase flow oscillations at $G = 1065.9 \text{ kg/m}^2\text{s}$ ,.....	147

Figure 6. 25. Two-phase flow characteristics under different heat fluxes: (a) water, (b) 0.01 v% nanofluid, and (c) 0.1 v% nanofluid..... 149

Figure 6. 26. Comparison of two phase flow characteristics between water and nanofluids under different heat flux..... 151

## LIST OF TABLES

Table 3. 1. Single-Phase Heat Transfer with Nanofluids.....	28
Table 3. 2. Selected conventional heat transfer correlations from the literature .....	49
Table 6. 1. Boiling and Two-Phase Heat Transfer with Nanofluids.....	105
Table 6. 2. Two-phase flow instabilites .....	135

## CHAPTER 1. INTRODUCTION

Nanofluids are engineered colloids that are formulated by stably dispersing solid nanoparticles (of 1 to 100 nm diameter) into a base fluid. The early discovery that thermal conductivity of nanofluids can be enhanced disproportionately even at very low nanoparticle concentrations [1-6] has generated great interests in nanofluids due to the implications for basic research and engineering applications [7]. Nanofluids have thus been considered as a promising example of advanced heat transfer fluids that can be tailored to possess desired thermophysical properties. However, thermal transport processes in nanofluids have not been well understood. In particular, a consensus is lacking on if and how the dispersed nanoparticles alter the single-phase and two-phase heat transfer mechanisms of nanofluids in forced convective flows, and the applicability of established fluid mechanics and heat transfer theories for predicting thermal transport of nanofluids has been called into question.

The present research aims at conducting a systematic study of single-phase convective heat transfer and two-phase flow boiling of nanofluids in a circular minichannel. The goals are to experimentally characterize the pressure drop and heat transfer behaviors of nanofluids with respect to their constituent base fluids, and to explore the effects of the particle-fluid interactions on the convective transport physics in nanofluids.

In this work, both aqueous water-based and non-aqueous Polyalphaolefin (PAO)-based nanofluids were synthesized using both spherical and rod-like  $\text{Al}_2\text{O}_3$  nanoparticles as the filler particles. The effective thermophysical properties of the  $\text{Al}_2\text{O}_3$ -water and  $\text{Al}_2\text{O}_3$ -PAO nanofluids, especially the viscosity and thermal conductivity, were first

characterized and compared to predictions from various effective medium theories (EMTs). Special attention was given to the effects of the nanoparticle size and aspect ratio, the aggregation and the dispersion state of nanoparticles. Then, an experimental investigation was conducted to study the single-phase forced convective heat transfer of the nanofluids through a circular minichannel. The friction factor and convective heat transfer coefficient were measured for the nanofluids over a wide range of Reynolds numbers, covering the laminar, transition and early stage of fully developed turbulent flows. Some interesting observations were made and discussed, such as the developing flow behaviors and delayed transition to turbulence for  $\text{Al}_2\text{O}_3$ -water nanofluids, and the effect of shear-induced alignment and orientational motion of nanoparticles on the transport phenomena of  $\text{Al}_2\text{O}_3$ -PAO nanofluids. Based on the convective heat transfer experimental data, the thermal performance and effectiveness of nanofluids for practical cooling applications were critically evaluated using different figures of merit (FOM). At last, convective flow boiling and two-phase flow of  $\text{Al}_2\text{O}_3$ -water nanofluids were studied experimentally with an emphasis on the effect of nanoparticle deposition on two-phase flow instabilities.

This dissertation is organized as follows. An overview of the literature relevant to each chapter is covered in the beginning of the chapter. Chapter 2 describes the synthesis of nanofluids and the experimental characterization of their effective thermophysical properties. Chapter 3 details the single-phase convective heat transfer and flow behavior of  $\text{Al}_2\text{O}_3$ -water nanofluids in a minichannel over the laminar, transition and turbulent flow regimes. Chapter 4 presents the single-phase thermal transport of  $\text{Al}_2\text{O}_3$ -PAO nanofluids containing both spherical and non-spherical nanoparticles in the laminar

region. Chapter 5 discusses the critical evaluation of thermal performance and effectiveness of nanofluids for cooling applications. Chapter 6 describes the flow boiling heat transfer and two-phase flow of  $\text{Al}_2\text{O}_3$ -water nanofluids. Finally, the conclusions of the present study and recommendations for future work are summarized in Chapter 7.

## **CHAPTER 2. NANOFUIDS SYNTHESIS AND CHARACTERIZATION**

Nanofluids are engineered colloids that are formulated by dispersing solid nanoparticles of 1 to 100 nm diameters into a base fluid. Commonly used base fluids include water, organic fluids (e.g., ethanol and ethylene glycol), oils, and lubricants. Materials for the solid nanoparticles include metals (e.g., gold and copper), and oxides (e.g., alumina, silica, zirconia, titania and copper oxide). Other materials such as carbon nanotubes and functionalized nanoparticles have also been used to prepare nanofluids. Since the early work of Choi in 1995 [8], extensive research efforts have been devoted to exploring the thermophysical properties. The most dramatic discovery of nanofluids has been the disproportionate enhancement of thermal conductivity at very low particle concentrations. Consequently, they have been generally considered as a promising candidate for advanced heat transfer fluids.

### **2.1 NANOFUIDS SYNTHESIS**

Nanofluids can be synthesized using either a one-step or two-step approach. In the first approach, which is also termed the direct evaporation-condensation (DEC) method, nanoparticles are simultaneously formed and dispersed in a fluid in a single process where the source material is vaporized and condensed directly into a flowing fluid under vacuum conditions [9-12]. The DEC method is preferred for producing nanofluids containing high-conductivity metal nanoparticles since it avoids oxidation of the nanoparticles. While it offers highly uniform and stable suspensions by minimizing particle agglomeration, the DEC method is only applicable to low-vapor-pressure fluids as a result of the need for processing in a vacuum. The two-step approach is the most

popular technique in preparing nanofluids, particularly for metal oxide nanoparticles [13], where the nanoparticles are first synthesized by either physical synthesis techniques such as the inert-gas-condensation (IGC) process [14] or chemical synthesis methods such as chemical vapor deposition[15], and then dispersed into a fluid in a second processing step. The two-step approach is advantageous for mass production of nanofluids because nanoparticles can now be economically produced in bulk. The biggest challenge in synthesizing nanofluids is the agglomeration of individual nanoparticles due to the attractive van der Waals forces between particles, which cause nanoparticles to aggregate and rapidly settle out of the base fluid. Physical or chemical dispersion techniques must be employed to overcome particle agglomeration and to improve the stability of nanofluids. In physical techniques, ultrasonic agitation, or ultrasonication, is widely used to break down nanoparticle aggregates by means of the addition of sonic energy. Chemical methods have long been used to stabilize colloidal suspensions by creating repulsive interaction between nanoparticles. This can be accomplished by the addition of surfactants, or by adjusting the pH value of the nanofluids via the introduction of an acid or alkali. In addition, surface functionalization of the nanoparticles has also been used to improve the dispersion behavior of nanofluids [16, 17].

In this work, two types of nanofluids were studied, including the aqueous  $\text{Al}_2\text{O}_3$ -water nanofluids and the non-aqueous  $\text{Al}_2\text{O}_3$ -Polyalphaolefin (PAO) nanofluids. The aqueous  $\text{Al}_2\text{O}_3$ -water nanofluids were prepared by dispersing commercial  $\gamma$ -phase  $\text{Al}_2\text{O}_3$  nanoparticles of 40 nm nominal diameter (Alfa Aesar) in deionized water. The volume concentrations investigated for single phase heat transfer were 1 and 2, 3.5 and 5 v%, respectively. The volume concentrations studied for flow boiling heat transfer were 0.01

v% and 0.1 v%. To stabilize the nanofluids, both physical and chemical dispersion techniques were employed. The normal procedures are as follows. The powder-like nanoparticles were first dispersed in the base fluid with a magnetic stirrer. A trace amount of nitric acid was then added to adjust the pH value of the suspension to 3.0, which creates repulsive electrostatic interaction between nanoparticles that alleviates the particle aggregation. Following that, the nanofluid sample was homogenized with a high-shear homogenizer (Barnant Model 700-5400) for 3 hours. As the last step, an ultrasonicator (Biologics 150 VT) was used to further break down the finer nanoparticle aggregates for 2 hours.

Polyalphaolefin (PAO) based nanofluids were formulated by dispersing boehmite alumina nanoparticles in 2 centiStokes (cSt) PAO under ultrasonication. Two types of Al<sub>2</sub>O<sub>3</sub>-PAO nanofluids were prepared. The first type (referred to as NF1) contains spherical nanoparticles, and the second type (referred to as NF2) contains nanorods. Due to the hydrophobic nature of PAO, special dispersants of minuscule amount were added to alleviate the aggregation of nanoparticles to stabilize the nanofluids. All the nanofluids samples were found stable without visible sedimentation for at least 7 days during the experiment period.

## **2.2 GEOMETRICAL CHARACTERIZATION OF NANOFLUIDS**

To assess the efficacy of ultrasonication, the dependence of effective particle size on the sonication duration was examined using validated DLS instrument (Malvern NanoZS). Figure 2.1 shows the effective particle size for Al<sub>2</sub>O<sub>3</sub>-water nanofluids measured at 15-minute intervals over a period of 2 hours. It shows the particle size decreases rapidly from, initially, 186 nm to 146 nm within the first 30 minutes, and

reaches a constant value of 135 nm at the end of ultrasonication. The size distribution of nanoparticles is shown in Figure 2.2. The effective particle size was found to be 135 nm, considerably larger than the nominal diameter (40 nm) specified by the vendor (Alfa Aesar). It indicates that the particle agglomeration cannot be entirely broken even after intensive mechanical and chemical dispersing. Strictly speaking, the effective particle size is slightly outside the upper bound of nanoparticles used in nanofluids (particle size from 1 to 100 nm), however, it is still well within the typical particle size range reported in the nanofluid literature. Similarly, the diameter of the spherical nanoparticles contained in Al<sub>2</sub>O<sub>3</sub>-PAO nanofluid NF1 was also measured using the DLS technique and was found to be about 60 nm.

The diameter and length of the non-spherical nanorods contained in Al<sub>2</sub>O<sub>3</sub>-PAO nanofluid NF2 were measured using transmission electron microscopy (TEM) (JEOL 1230 HC TEM). Before the TEM measurement, the sample was prepared by diluting the nanofluid containing 0.65 v% nanorods with pure 2 cSt PAO at a ratio of 1:10 and sonicating the mixture for 4 hours. The measured diameters of the individual nanorods ( $d$ ) range from 5 nm to 11 nm, and the lengths ( $L$ ) range from 80 nm to 106 nm. Taking the average measurements from 10 TEM images, the mean diameter and length of the nanorods were  $d = 7.0$  nm and  $L = 85$  nm, respectively, which correspond to an average aspect ratio of  $r = L/d \sim 12$  (Figure 2.3).

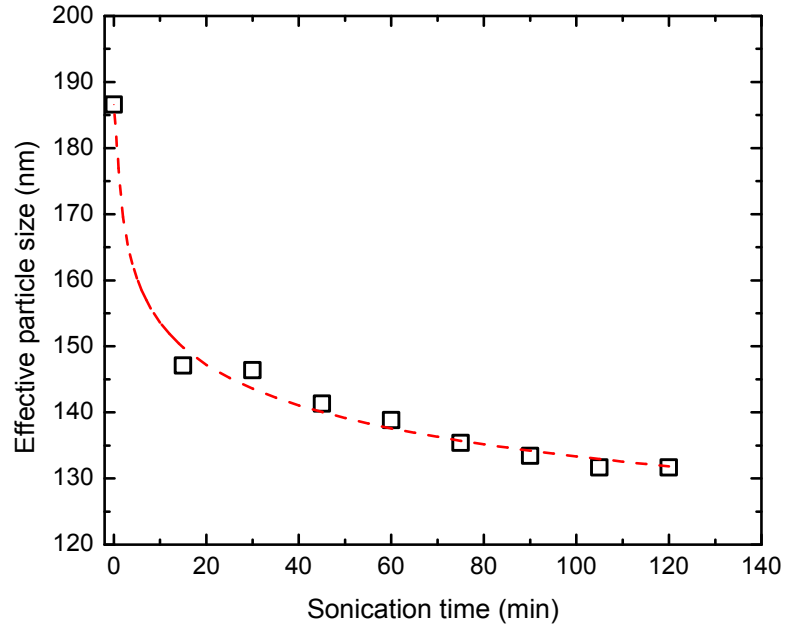


**Figure 2. 1.** Effective particle size versus sonication time (0.1 v% Al<sub>2</sub>O<sub>3</sub>-water nanofluid, pH=3 ).

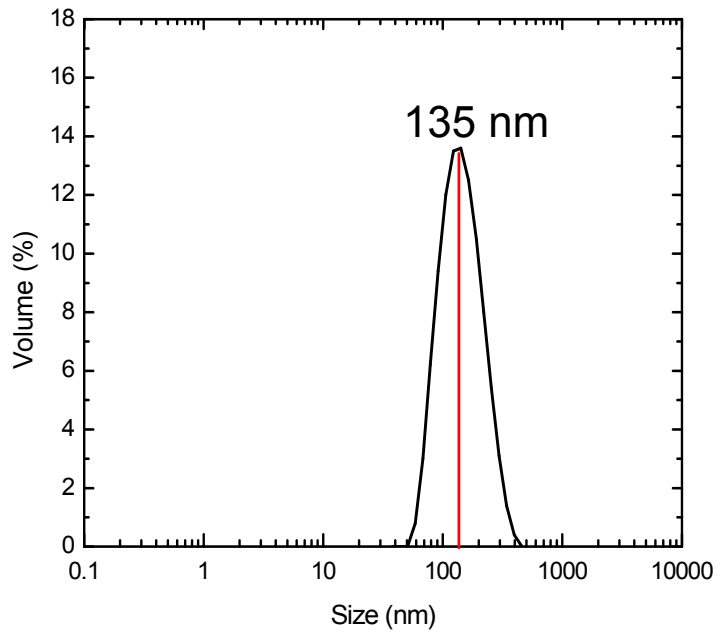


**Figure 2. 2.** DLS measurement of effective particle size (0.1 % Al<sub>2</sub>O<sub>3</sub> nanofluid, pH = 3).

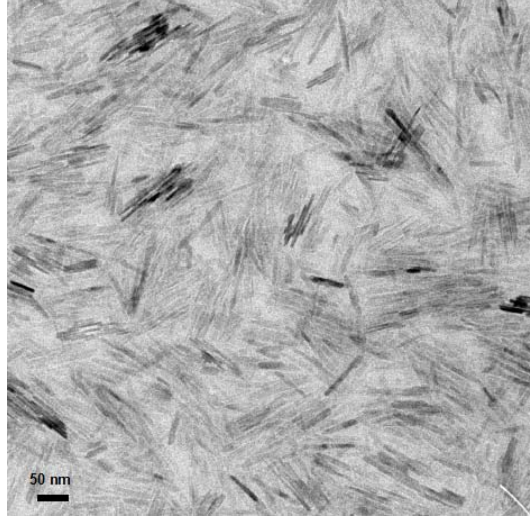


**Figure 2. 3.** TEM of Al<sub>2</sub>O<sub>3</sub> nanorods.

## 2.3 THERMOPHYSICAL PROPERTIES OF NANOFLUIDS

Thermophysical properties that are crucial to convective heat transfer include density  $\rho$ , specific heat  $c_p$ , viscosity  $\mu$ , and thermal conductivity  $k$ . In this work, the effective density and the effective specific heat of a nanofluid are estimated as

$$\rho = \phi \cdot \rho_p(T) + (1 - \phi) \cdot \rho_f(T) \quad , \quad (2.1)$$

$$c_p = \frac{\phi \cdot [\rho_p(T)c_{p,p}(T)] + (1 - \phi) \cdot [\rho_f(T)c_{p,f}(T)]}{\rho(T)} \quad , \quad (2.2)$$

where  $\phi$  is the particle volume concentration,  $\rho$  the density of the nanofluids,  $\rho_p$  the nanoparticle density,  $\rho_f$  the density of base fluid,  $c_p$  the specific heat of nanofluids,  $c_{p,p}$  the nanoparticle specific heat, and  $c_{p,f}$  is the specific heat of base fluid.

## 2.3.1 VISCOSITY

### 2.3.1.1 THEORY

For suspensions of spherical particles, the relative viscosity can be expressed by the Batchelor equation [18] as a function of nanoparticle volume fraction

$$\mu_r = \frac{\mu}{\mu_f} = 1 + [\mu]\phi + k_H\phi^2 + O(\phi^3) \quad , \quad (2.3)$$

where the intrinsic viscosity is  $[\mu] = 2.5$  and the Huggins coefficient is  $k_H = 6.2$  [19, 20]. The first two terms at the RHS of Eq. (2.3) are related to the particle diffusion; the third term arises in concentrated suspensions, and the coefficient  $k_H$  is very sensitive to the rheological structure of the suspension [21]. At infinite dilution, Eq. (2.3) reduces to the well-known Einstein equation,  $\mu_r = 1 + 2.5\phi$ .

Addition of particles, particularly anisotropic particles such as spheroids, rods or discs, into a base fluid results in an effective viscosity that is higher than the viscosity of the base fluid. This is due to the Brownian and hydrodynamic motions of the dispersant particles. In suspensions of rod-like particles, the impact of translational Brownian motion of the particles is negligible on the viscosity, as compared to that due to the rotational Brownian motion. As such, the effective viscosity is mainly affected by the competition between the shear force and the rotational Brownian motion, represented by the rotational Peclet number

$$Pe_{rot} = \frac{\dot{\gamma}}{D_r} \quad , \quad (2.4)$$

where  $\dot{\gamma}$  is the shear rate, and  $D_r$  is the rotational diffusion constant of the particles. It is easy to see the low shear limit (as encountered under the static conditions) corresponds to

$Pe_{rot} \ll 1$ . If the particle concentration is sufficiently high, the particles will overlap and interact hydrodynamically, and the rotational freedom is restricted. Recasting the particle volume concentration in terms of the number density  $v$ , it yields  $v = \phi / \left( \frac{\pi}{4} d^2 L \right)$  for a dispersion of rod-like particles with a diameter  $d$  and a length  $L$ . The minimum overlap concentration is given by [22]

$$v^* = \frac{1}{L^3}. \quad (2.5)$$

If the particle dispersion is infinitely dilute ( $v < 0.1 v^*$ ), each particle can rotate freely and the relative viscosity of the nanofluid is

$$\mu_r = 1 + [\mu] \phi, \quad (2.6)$$

where  $[\mu]$  can be calculated from one of the following equations [23, 24]

$$[\mu] = \frac{4}{15} \frac{r^2}{\ln r}, \quad \text{for } r \gg 1 \quad (2.7)$$

or

$$[\mu] = \frac{r^2}{5} \left[ \frac{1}{3(\ln 2r - 1.5)} + \frac{1}{\ln 2r - 0.5} \right] + 1.6, \quad \text{for } r > 15. \quad (2.8)$$

At higher shear rate, i.e.,  $Pe_{rot} \geq r^3$ , the orientation distribution of the particles due to shear forces dominates over the Brownian motion, and  $[\mu]$  can be estimated by the equation by Hinch and Leal [25]

$$[\mu] = 0.315 \frac{r}{\ln r}. \quad (2.9)$$

If  $v \geq 0.1 v^*$ , the rod-rod hydrodynamic interaction starts to contribute to the effective viscosity of the suspension. For instance,  $0.1 v^*$  corresponds to a particle volume concentration of 0.055% for nanorods with  $L = 85$  nm and  $d = 7$  nm in this work. When

the particle concentration falls in the range of  $0.1v^* < v < v^*$ , the suspension can still be considered dilute. The relative viscosity at low shear limit ( $Pe_{rot} \ll 1$ ) is estimated from the Berry-Russel equation [26]

$$\mu_r = 1 + [\mu]\phi + k_H [\mu]^2 \phi^2, \quad (2.10)$$

where  $k_H = \frac{2}{5}(1 - 0.00142Pe_{rot}^2)$  and  $[\mu]$  can be found from Eqs. (2.7) or (2.8). At higher particle concentrations,  $v^* < v < (dL^2)^{-1}$ , or equivalently,  $0.55\% < \phi < 6.5\%$  for the PAO-nanofluids in the present study, the particle suspension is considered semi-dilute. In this concentration range, the rotational volumes of adjacent rods will overlap and the rods are entangled. The low-shear viscosity of such particle suspensions is given by [22]

$$\mu_r = 1 + \frac{r^2}{15 \ln r} \phi + \frac{36r^6}{5\pi^2 \beta \ln r} \phi^3, \quad (2.11)$$

where  $\beta$  is a numerical factor ( $\beta = 10^3 - 10^4$ ). When the particle concentration further increases to the maximum packing fraction,  $\phi_m$ , the Krieger-Dougherty correlation [27] can be used to estimate the relative viscosity

$$\mu_r = [1 - (\phi / \phi_m)]^{-[\mu]\phi_m}, \quad (2.12)$$

where  $\phi_m = 5.4/r$  for  $r \gg 1$  [28, 29].

In addition to the hydrodynamic interaction between particles, two more effects must be considered in the study of the effective viscosity of nanofluids: the particle aggregation and the shear flow. Most nanoparticles naturally adhere to each other, although the aggregation can be suppressed to some degree with stabilizing agents. As a consequence, the particle volume fraction,  $\phi$ , should be replaced by an effective volume fraction,  $\phi_a$ , as suggested by Chen et al. [30, 31]

$$\phi_a = \phi \left( \frac{a_a}{a} \right)^{3-M}, \quad (2.13)$$

where  $a$  is the primary nanoparticle size,  $a_a$  is the effective size of the aggregates; and  $M$  is the fractal index. The value of  $M$  varies between 1.6 and 2.3, and is approximately 1.8 for spherical nanoparticles. Since  $(a_a/a) > 1$ , the particle aggregation results in  $\phi_a$  that is higher than  $\phi$ , which, in turn, leads to a higher viscosity of the nanofluids. On the other hand, when a shear flow is applied, the rod-like particles tend to align spontaneously with the flow field. Thus the impact of the rotational motion of nanoparticles on viscosity will diminish as the shear rate increases. In fact, the shear thinning behavior was observed in nanofluids at high particle volume fraction under high shear conditions [30, 31]. Therefore, the effective viscosity of nanofluids in forced convective flow is expected to be lower than the values measured at the static conditions.

### 2.3.1.2 EXPERIMENTAL RESULTS

The effective viscosity of Al<sub>2</sub>O<sub>3</sub>-water nanofluids was measured at 25°C using a capillary viscometer (Cannon-Ubbelohde 9721-R53). The normalized results with reference to the viscosity of pure water are presented in Figure 2. 4. It is seen that the effective viscosity exceeds that of water and increases with the nanoparticle volume concentration. Nonetheless, the viscosity increment is moderate and can be well predicted by the Batchelor correlation[18]

$$\mu = \mu_f (T) \left( 1 + 2.5\phi + 6.2\phi^2 \right). \quad (2.14)$$

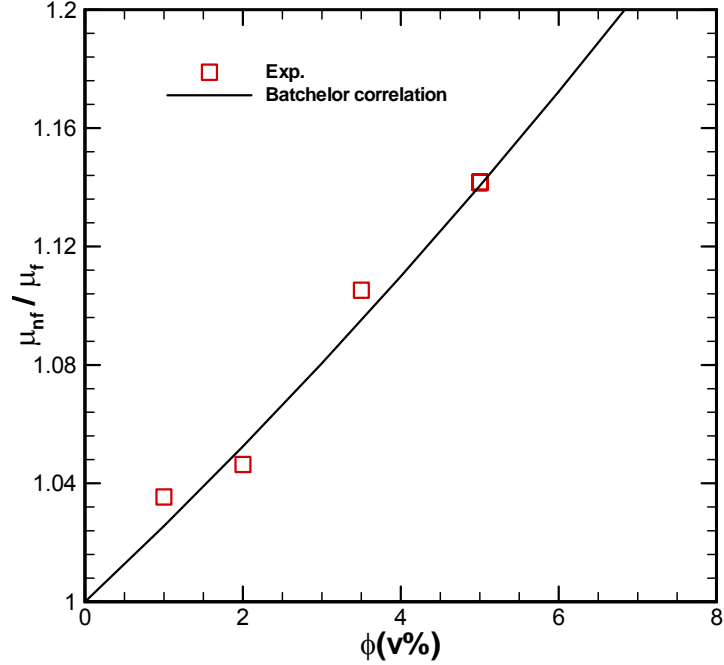


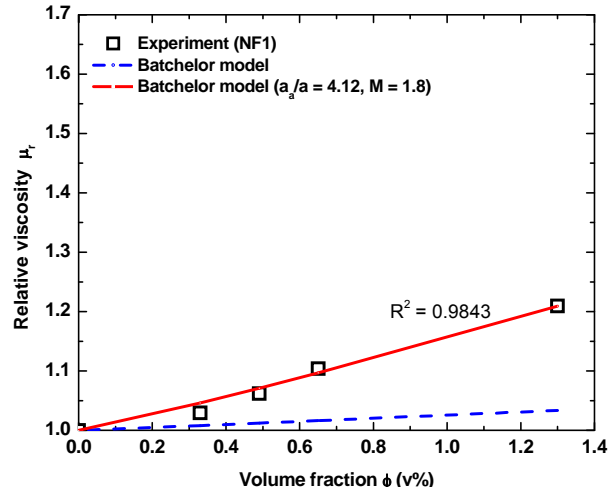
**Figure 2. 4.** Effective viscosity of nanofluid at various volume concentrations at 25°C.

The viscosity of Al<sub>2</sub>O<sub>3</sub>-PAO nanofluids was measured at 25°C using the same capillary viscometer under static conditions, which correspond to the low shear limit, for particle volume fractions of 0.33, 0.49, 0.65, and 1.3 v%, respectively. Figure 2. 5(a) shows the measured data of NF1 as well as the comparison with theoretical predictions. The viscosity of nanofluids clearly increases with the nanoparticle volume fraction. The original Batchelor equation (Eq. (2.3)) underpredicts the experimental data, but it can be used in combination with the effective volume fraction calculated from Eq. (2.13) to better correlate the viscosity data of nanofluids. In doing so, the actual value of  $a_d/a$  needs to be determined a priori, however, here it is employed as a fitting parameter. It is found that the selection of  $a_d/a = 4.12$  and  $M = 1.8$  yields a good agreement between the predictions and the measured data with a coefficient of determination of  $R^2 = 0.9843$ .

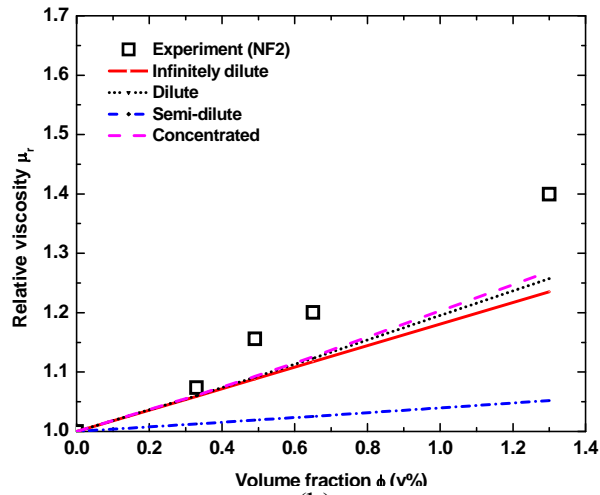
For simplicity, an empirical correlation was proposed for the relative viscosity of nanofluids containing spherical nanoparticles

$$\mu_r = 1 + 13.67\phi + 185.42\phi^2, \quad \text{for NF1.} \quad (2.15)$$

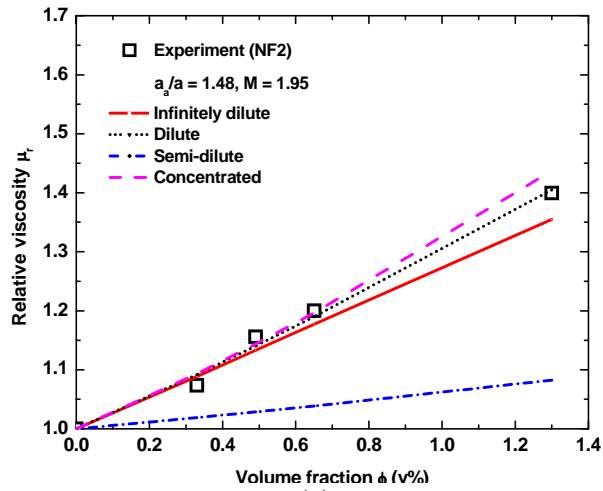
Figure 2. 5(b) illustrates the measured relative viscosity of NF2 as a variation of the nanoparticle volume fraction. As compared to the results for NF1 in Figure 2. 5(a), the viscosity of NF2 is distinctly higher at the same particle concentration, and the difference widens as the concentration increases. Similar observations were reported by Chen et al. [32] and Zhou et al. [33]. The results suggest the important role played by the particle geometry and aspect ratio in affecting the rheological properties of nanofluids. Also shown in Figure 2. 5(b) are the predictions from the theoretical models developed for suspensions of rod-like particles. Unfortunately, they all underestimate the measurement data. Considering again the aggregation effect, the effective volume fraction of rod-like particles can be estimated from Eq. (2.13), where  $a_e/a = 1.48$  and  $M = 1.95$  were chosen. Using the effective volume fraction, the modified theoretical predictions are compared again with the experimental data in Figure 2. 5(c). It is seen the dilute suspension model yields the best overall prediction ( $R^2 = 0.9920$ ) of the relative viscosity of nanofluids.



(a)



(b)



(c)

**Figure 2. 5.** The effective viscosity of nanofluids at various nanoparticle volume fractions.

An empirical correlation similar to Eq. (2.15) was proposed for the relative viscosity of nanofluids containing nanorods

$$\mu_r = 1 + 27.29\phi + 296.92\phi^2, \quad \text{for NF2.} \quad (2.16)$$

It is noted that Eqs. (2.15) and (2.16) are valid for  $\phi \leq 1.3$  v%.

The viscosities of nanofluids at elevated temperatures were not investigated in this work. Instead, they were estimated by

$$\mu(T) = \mu_r \cdot \mu_f(T). \quad (2.17)$$

## 2.3.2 THERMAL CONDUCTIVITY

### 2.3.2.1 THEORY

The Hamilton-Crosser model [34] is one of the most widely-cited correlations to predict effective thermal conductivity of solid-liquid mixtures,

$$k_r = \frac{k}{k_f} = \frac{k_p + (n-1)k_f - (n-1)(k_f - k_p)\phi}{k_p + (n-1)k_f + (k_f - k_p)\phi}, \quad (2.18)$$

where the shape factor is  $n = 3/\psi$ ,  $\psi$  is the sphericity defined as the ratio of the surface area of a sphere (with the same volume as the given particle) to the surface area of the particle. For spherical particles,  $\psi = 1$ , Eq. (2.18) reduces to the classical Maxwell model

$$k_r = \frac{1 + 2\beta\phi}{1 - \beta\phi}, \quad (2.19)$$

where  $\beta = (k_p - k_f)/(k_p + 2k_f)$ . To account for the interfacial thermal resistance, the Maxwell-Garnett model [35] yields

$$k_r = \frac{(1+2\alpha) + 2\phi(1-\alpha)}{(1+2\alpha) - \phi(1-\alpha)}, \quad (2.20)$$

where  $\alpha = 2R_b k_f / D$  and  $R_b$  is the interfacial resistance. While  $R_b$  is difficult to measure directly, molecular dynamics simulations suggest it is typically of the order of  $10^{-8} \sim 10^{-9}$  m<sup>2</sup>K/W [15].

For dilute suspensions containing randomly dispersed spheroidal particles, Nan et al. [35] developed an effective thermal conductivity model

$$k_r = 1 + \frac{\phi(2\beta_{11} + \beta_{33})}{3 - \phi(2\beta_{11}L_{11} + \beta_{33}L_{33})}, \quad (2.21)$$

where

$$\beta_{ii} = (k_{ii} - k_f) / [k_f + L_{ii}(k_{ii} - k_f)], \quad (2.22)$$

The depolarization factors for prolate spheroids are

$$L_{11} = \frac{r^2}{2(r^2 - 1)} - \frac{r}{2(r^2 - 1)^{3/2}} \cosh^{-1} r \quad \text{and} \quad L_{33} = 1 - 2L_{11}, \quad (2.23)$$

and the equivalent thermal conductivities along the two spheroidal axes are

$$k_{11} = \frac{k_p}{1 + 2k_p R_b / D} \quad \text{and} \quad k_{33} = \frac{k_p}{1 + 2k_p R_b / L}. \quad (2.24)$$

### 2.3.2.2 EXPERIMENTAL RESULTS

The effective thermal conductivity of nanofluids was measured using a thermal property analyzer (KD2 Pro), which is based on the transient hot wire method [10, 36].

A sample measurement for Al<sub>2</sub>O<sub>3</sub>-water nanofluids in Figure 2. 6 shows that the thermal conductivity of nanofluid is enhanced as compared to that of water and can be

reasonably correlated by the Buongiorno model (Eq. (2.25)) [37] over the temperature range measured

$$k = k_f(T)(1 + 4.5503\phi). \quad (2.25)$$

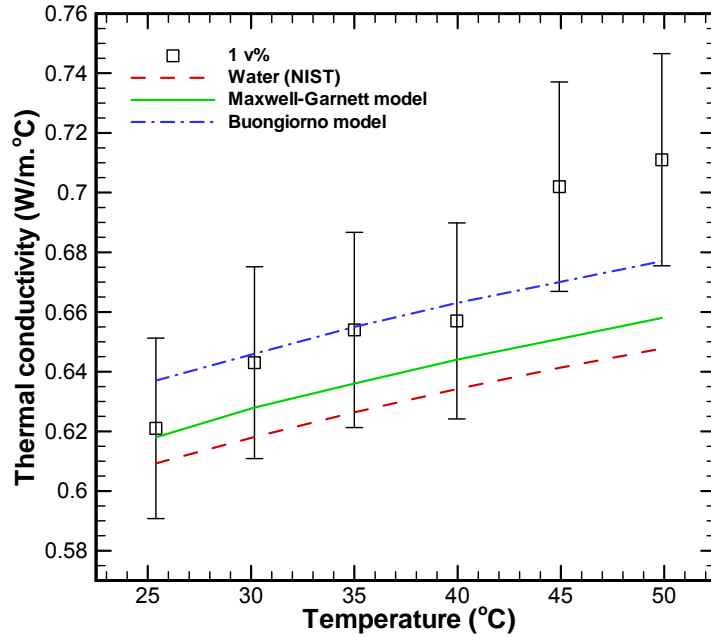


**Figure 2. 6.** Effective thermal conductivity of nanofluid at various temperatures (error bar  $\pm 5\%$ ).

It is noted that, in Eq. (2.25), the temperature dependence has been considered in the thermophysical properties of the nanofluids[38, 39].

Figure 2. 7 illustrates the comparison of the measured effective thermal conductivity of  $\text{Al}_2\text{O}_3$ -PAO nanofluid NF1 with the predictions from Eqs. (2.18) and (2.20). In their original forms, both the Hamilton-Crosser model and the Maxwell-Garnett model significantly under-predict the experimental data, as manifested in Figure 2. 7(a). If the particle aggregation effect is considered, the effective volume fraction of NF1 used in the viscosity calculation (with  $a_a/a = 4.12$  and  $M = 1.8$ ) can be applied in

estimating the effective thermal conductivity. The new results are plotted in Figure 2. 7(b). The Hamilton-Crosser model is seen to overestimate the thermal conductivity. The accuracy of the Maxwell-Garnett model is affected by the choice of  $R_b$ , which is used here as a fitting parameter. By using regression analysis, it is found that for  $R_b = 6.5 \times 10^{-8} \text{ m}^2\text{K/W}$ , the Maxwell-Garnett model can offer the best match with the experimental data with  $R^2 = 0.9962$ . For simplicity, the experimental data are correlated by a linear function of the nanoparticle volume fraction

$$k / k_f = 1 + 7.6661\phi, \quad \text{for NF1.} \quad (2.26)$$

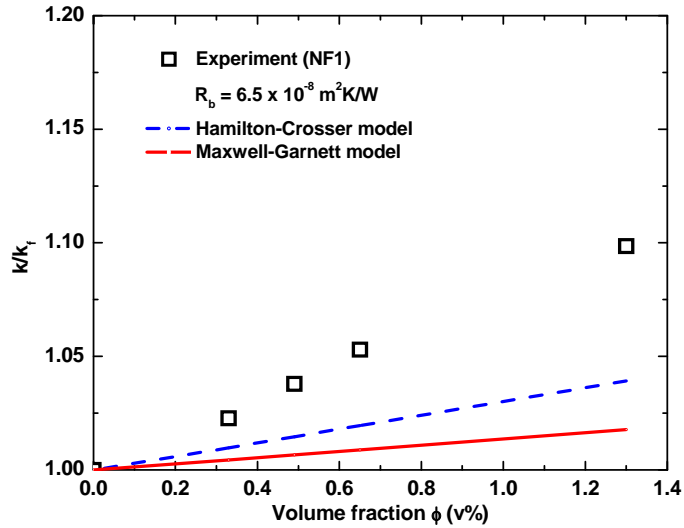
Figure 2. 7 shows the comparison of the measured thermal conductivity of  $\text{Al}_2\text{O}_3$ -PAO nanofluid NF2 with predictions from the Nan et al. model [40]. Clearly, this model fails to predict the experimental data satisfactorily. However, when the effective volume fraction (with  $a_d/a = 1.48$  and  $M = 1.95$ ) and  $R_b = 1.24 \times 10^{-8} \text{ m}^2\text{K/W}$  are used, the modified model offers a much better prediction of the experimental data ( $R^2 = 0.9582$ ). In light of the complexity of the Nan et al. model (Eqs. (2.21) through (2.24)), a simple correlation was proposed to predict the effective thermal conductivity of nanofluids containing nanorods

$$k / k_f = 1 + 9.4539\phi, \quad \text{for NF2.} \quad (2.27)$$

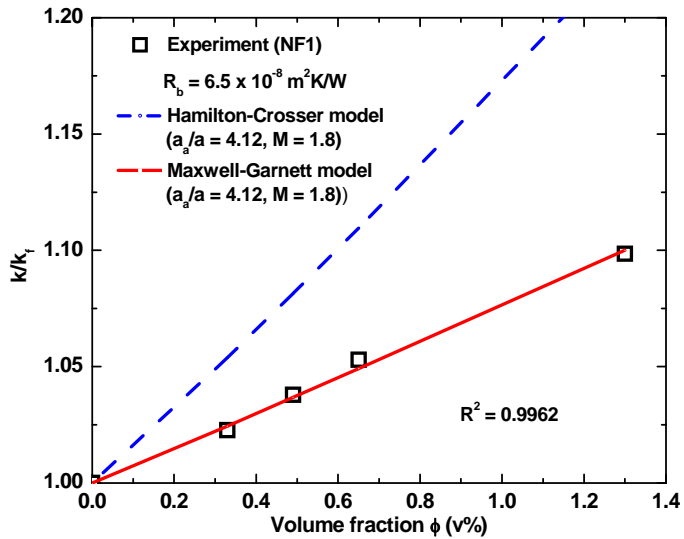
### 2.3.2.3 FURTHER DISCUSSION

In the above discussions, the nanofluids are regarded as a matrix-based composite material, whose effective thermal conductivity depends on the constituent materials, the volume fraction and the size/shape of the filler nanoparticles. On the other hand, as a heat transfer parameter, the thermal conductivity of nanofluids is also critically affected by the distribution and the relative orientation of nanoparticles with respect to the

temperature field [40]. As depicted in Figure 2.9, there are four possible particle configurations in the particle-fluid suspension, namely, the parallel, series, Hashin-Shtrikman (or H-S) and EMT configurations.



(a)



(b)

**Figure 2.7.** The effective thermal conductivity of NF1 as a function of nanoparticle volume fraction.

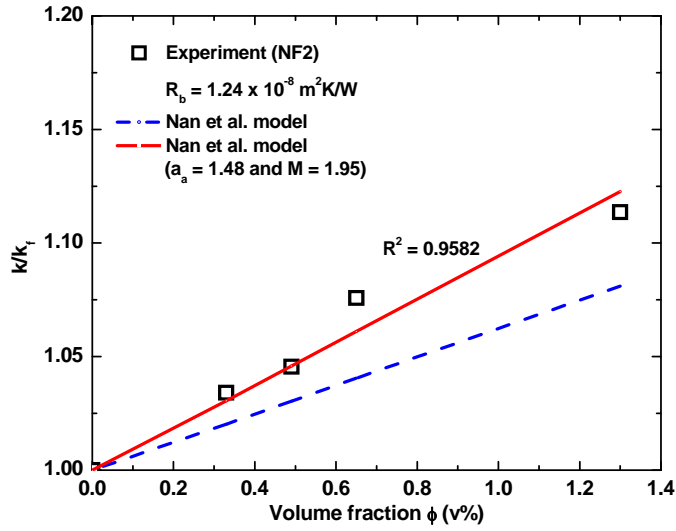


**Figure 2. 8.** The effective thermal conductivity of NF2 as a function of nanoparticle volume fraction.

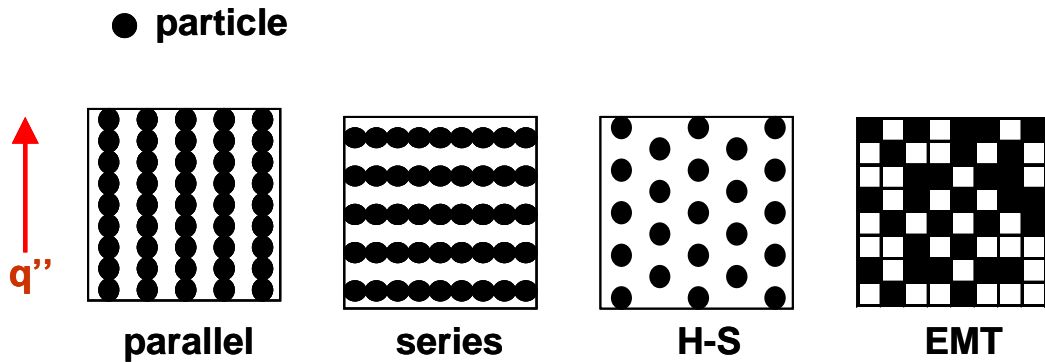


**Figure 2. 9.** Four possible particle configurations in particle suspensions.

In each representative cell, the heat flux is applied from the bottom boundary to the top boundary. When the particles are continuously configured in parallel with or perpendicular to the direction of the temperature gradient, the effective thermal conductivity can be described by the parallel or the series model [41, 42]

Parallel model  $k = (1 - \phi)k_f + \phi k_p,$  (2.28)

$$\text{Series model} \quad k = \frac{1}{(1-\phi)/k_f + \phi/k_p}. \quad (2.29)$$

The parallel and series models represent the upper and lower bounds over all possible structures of a heterogeneous material, respectively. In the H-S configuration, the discrete particles are uniformly distributed without direct contact with each other. The corresponding effective thermal conductivity is given by [43]

$$k_e = k_p + \frac{1-\phi}{\frac{1}{k_m - k_p} + \frac{\phi}{3k_p}}. \quad (2.30)$$

In real particle suspensions, the particle distribution is neither continuous nor uniform. More likely, it takes the form of the EMT structure, i.e., a random distribution. For such kind of particle dispersion, the effective thermal conductivity is predicted by the EMT model [44, 45],

$$k = \{(3\phi - 1)k_p + [3(1 - \phi) - 1]k_f + \sqrt{[(3\phi - 1)k_p + [3(1 - \phi) - 1]k_f]^2 + 8k_f k_p}\} / 4. \quad (2.31)$$

For the four particle configurations of the Al<sub>2</sub>O<sub>3</sub>-PAO nanofluids ( $k_p/k_f = 348$ ), the theoretical predictions of the effective thermal conductivity are plotted in Fig. 7 over the full range of volume fraction ( $0 \leq \phi \leq 1$ ). At any given composition, the highest possible thermal conductivity is obtained in the parallel structure, where heat is conducted through the parallel pathways formed by the aligned particles. In contrast, the lowest possible thermal conductivity occurs in the series structure.

In almost all heat transfer experiments of nanofluids (including the present one), the effective thermal conductivity was measured under static conditions, where the nanoparticles were assumed to disperse either randomly or uniformly in the base fluid. However, the measured thermal conductivity data of NF2, presented as the inset in

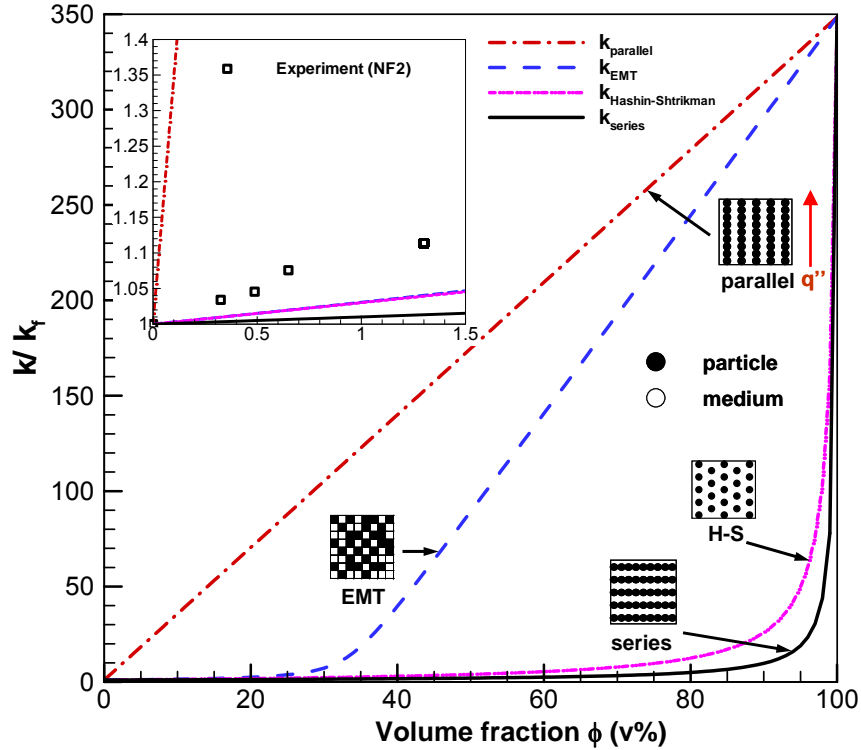


**Figure 2. 10.** Effective thermal conductivity for various particle configurations.

Figure 2. 10, lie between the predictions of the parallel model and the EMT/H-S model, suggesting the actual distribution of the nanorods is neither completely orderly nor completely random. Furthermore, when the nanofluid is flowing through a circular channel, a velocity gradient exists along the radial direction, and therefore, the resulting shear stress will strongly align the non-spherical particles with the flow direction, as schematically depicted in Figure 2. 11 [21]. After the flow becomes hydrodynamically fully developed, a particle-fluid structure similar to the series configuration in Figure 2. 10 will be formed. Consequently, it is reasonable to expect that the actual thermal conductivity of nanofluids containing rod-like particles in the convective flow would be less than that is measured under static conditions. The reduced effective

thermal conductivity will adversely affect the convective heat transfer performance of the nanofluids.

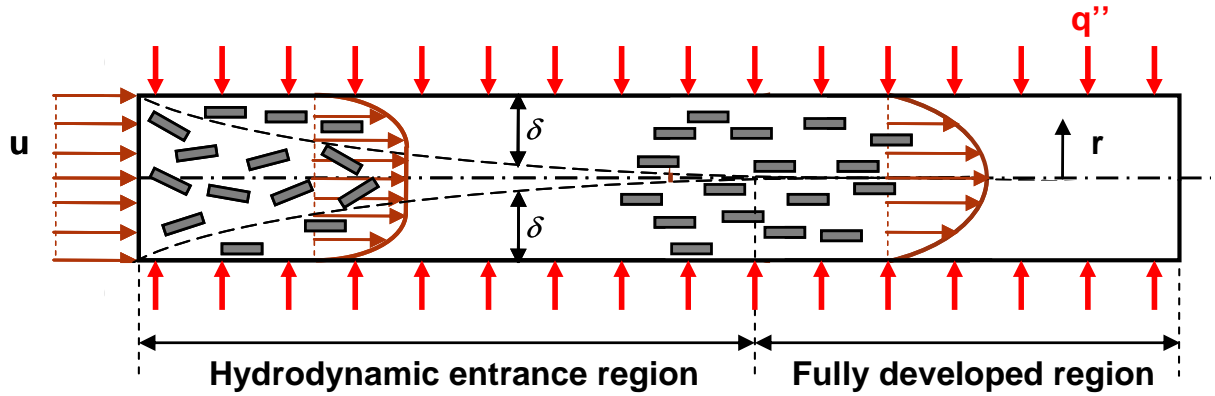


**Figure 2. 11.** Shear-induced alignment of rod-like nanoparticles in convective flow through a channel.

## 2.4 SUMMARY

An experimental study was conducted to investigate the thermophysical properties of  $\text{Al}_2\text{O}_3$ -water and  $\text{Al}_2\text{O}_3$ -PAO nanofluids containing both spherical and rod-like nanoparticles. The effective viscosity and effective thermal conductivity of the nanofluids were measured, and were compared to predictions from several existing theories in the literature. It was found that the presence of nanoparticles alters the effective thermophysical properties of nanofluids, and the particle size and aspect ratio are the important influencing factors. Additionally, the effective viscosity and thermal conductivity of nanofluids in the shear flow are also affected by the dispersion state, the aggregation of nanoparticles as well as the interaction particles between and fluid.

## **CHAPTER 3. SINGLE-PHASE THERMAL TRANSPORT OF AQUEOUS NANOFLUIDS IN A MINICHANNEL**

Single-phase forced convection of nanofluids has drawn particular interest due to its direct engineering relevance in a variety of applications ranging from energy storage, electronics cooling to thermal processing of materials [32, 37, 46-61]. It was found that, in both laminar and turbulent flows, convective heat transfer is enhanced in nanofluids compared to the base fluids. Most studies showed that the heat transfer enhancement increases with increasing nanoparticle concentration and  $Re$ . Moreover, the enhancement generally surpasses what can be expected from the thermal conductivity enhancement alone. Thus the applicability of the established heat transfer correlations for predicting the thermal transport of nanofluids has been called into question. This chapter presents a thorough experimental investigation of single-phase convection of  $Al_2O_3$ -water nanofluids in a circular minichannel. The objectives are 1) to characterize the pressure drop and heat transfer behaviors of nanofluids with respect to their constituent base fluid; 2) to validate the applicability of established conventional correlations in predicting the flow and heat transfer of nanofluids; and 3) to explore the fundamental mechanisms underlying the convective transport in nanofluids.

### **3.1 LITERATURE SURVEY**

Single-phase convective heat transfer of nanofluids has been studied due to its direct relevance to various engineering applications. While the effective thermal conductivity of a nanofluid may be higher relative to the base fluid, the convective heat transfer coefficient also depends on other properties, such as the density, viscosity and specific

heat of the nanofluids. Table 3. 1(a) to (c) provide a compilation of the data collected for single-phase convective heat transfer of nanofluids from experimental, numerical and theoretical studies in the literature [32, 37, 46-54, 56-67]. Convective heat transfer in nanofluids has been found to be improved under both laminar and turbulent flow conditions, with the enhancement increasing as the particle volume concentration or the particle thermal conductivity increases. However, the heat transfer enhancement observed has usually exceeded the thermal conductivity enhancement, indicating that additional mechanisms of heat transfer enhancement are present in convection beyond those corresponding to increased thermal conductivity alone. In addition, the applicability of established heat transfer correlations, even with the effective thermophysical properties of nanofluids factored in, has been called into question in some studies[17]. Considering the limited experimental data available in the literature, firm conclusions are yet to be drawn regarding the transport mechanisms in convective heat transfer with nanofluids.

**Table 3. 1. (a) Single-Phase Heat Transfer with Nanofluids (Experiments).**

Reference	Nanofluid	Particle Size and Concentration	Experimental Conditions	Key Findings	Mechanisms and Models
Li and Xuan [46, 47]	Cu-water	< 100 nm 0.3-2 v%	Forced convection Re = 800-25000  Tube dimensions not reported	<ul style="list-style-type: none"> <li>Heat transfer with nanofluids (2 v%) is 60% higher than for pure water.</li> <li>Heat transfer coefficient and Nusselt number increase with increasing nanoparticle concentration.</li> <li>Dittus-Boelter correlation does not predict Nusselt number even with effective thermal properties of nanofluids used.</li> <li>Measured friction factor is almost identical to that of pure water.</li> </ul>	<ul style="list-style-type: none"> <li>Heat transfer enhancement is attributed to increased thermal conductivity and intensified energy exchange due to chaotic motion of nanoparticles.</li> <li>Proposed correlations: Laminar <math>Nu_{nf} = 0.4328(1.0 + 11.285 \rho^{0.754} P_{ef}^{0.218}) Re_{nf}^{0.333} Pr_{nf}^{0.4}</math> Turbulent <math>Nu_{nf} = 0.0059(1.0 + 7.6286 \rho^{0.6886} P_{ef}^{0.001}) Re_{nf}^{0.9238} Pr_{nf}^{0.4}</math></li> </ul>
Yang et al. [48]	Graphite-ATF Graphite-oils	d = 1-2 μm l = 20-40 nm 2, 2.5 wt%  (l is the length)	Forced convection Re = 10-100  Tube dimensions not reported	<ul style="list-style-type: none"> <li>Nanofluids of 2.5 wt% loading increase heat transfer coefficient h by 22% at 50°C and 15% at 70°C; nanofluids of 2 wt% loading have no appreciable impact on h.</li> <li>Experimental measurements of h exhibit the same 1/3-power dependence on Re as in the Seider-Tate correlation. However, the correlation overpredicts h if enhanced effective thermal conductivity is used.</li> <li>Correlations by Oliver [39] and Eubank-Proctor [40] bracket the measured Nu data.</li> </ul>	<ul style="list-style-type: none"> <li>Weaker heat transfer enhancement with 2% nanofluids is attributed to lack of percolation of nanoparticles at lower concentrations.</li> <li>Nanofluids enhance heat transfer coefficient via increased thermal conductivity and movement of nanoparticle relative to the fluid.</li> <li>Temperature-dependence of heat transfer enhancement is caused by disruption of particle-particle interactions due to reduced shear force at elevated temperatures.</li> </ul>
Wen and Ding[49]	γAl <sub>2</sub> O <sub>3</sub> -water (SDBS added)	27-56 nm 0.6-1.6 v%	Forced convection Re = 500-2100  Circular tube (copper) D = 6.4 mm	<ul style="list-style-type: none"> <li>Nanofluids improve heat transfer by 47%.</li> <li>Heat transfer enhancement increases with Re and nanoparticle concentration and is more pronounced in the entrance region.</li> <li>Heat transfer enhancement cannot be explained by the higher effective thermal conductivity.</li> <li>Shah correlation [68] cannot predict measured Nusselt number.</li> </ul>	<ul style="list-style-type: none"> <li>Nanoparticle migration causes non-uniform distribution of particle concentration and reduces thermal boundary layer thickness.</li> <li>Heat transfer enhancement in entrance region is mainly due to decreased thermal boundary layer thickness rather than increased thermal conductivity.</li> </ul>

Reference	Nanofluid	Particle Size and Concentration	Experimental Conditions	Key Findings	Mechanisms and Models
Ding et al.[50]	CNT-water (with 0.25 wt% gum-Arabic)	Size not reported 0-0.5% wt%	Forced convection Re = 800-1200  Circular tube (stainless steel) D = 4.5 mm L = 970 mm	<ul style="list-style-type: none"> <li>Convective heat transfer is enhanced by over 350% with 0.5% CNT concentration at Re = 800.</li> <li>Heat transfer enhancement increases with Re and nanoparticle concentration, and is more pronounced in the entrance region.</li> </ul>	<ul style="list-style-type: none"> <li>Heat transfer enhancement attributed to: <ul style="list-style-type: none"> <li>enhanced thermal conductivity both at static and dynamic conditions;</li> <li>reduced boundary layer thickness due to particle migration caused by non-uniform shear rate; and</li> <li>high aspect ratio of CNTs.</li> </ul> </li> </ul>
He et al.[51]	TiO <sub>2</sub> -water	95,145,210 nm 1.0-4.9 wt% (0.24-1.18 v%)	Forced convection Re = 900-5900  Circular tube (copper) D = 3.97 mm L = 1834 mm	<ul style="list-style-type: none"> <li>Thermal conductivity increases with increasing particle concentration and decreasing particle size.</li> <li>Nanofluids exhibit shear thinning at high shear rate. Viscosity increases with particle concentration and particle size.</li> <li>Heat transfer is enhanced with increasing particle concentration. Enhancement in laminar regime (12% at Re = 1500) is less than that in turbulent flow (40% at Re = 5900).</li> <li>Pressure drop can be predicted by conventional theory only at low Re.</li> </ul>	<ul style="list-style-type: none"> <li>Convective heat transfer is affected by the viscosity and the particle migration.</li> </ul>
Heris et al.[52]	$\gamma$ Al <sub>2</sub> O <sub>3</sub> -water	20 nm 0.2-2.5% v%	Forced convection Re = 500-2000  Annular tube (copper) D = 6 mm, L = 1 m	<ul style="list-style-type: none"> <li>Convective heat transfer is enhanced with increase in nanoparticle concentration. The maximum enhancement is 41% at Pe = 6000 for 2.5 v% nanofluid.</li> </ul>	—

Reference	Nanofluid	Particle Size and Concentration	Experimental Conditions	Key Findings	Mechanisms and Models
Chen et al.[32]	Titanate nanotubes-water	260 nm 0.5, 1, 2.5 wt%	Forced convection Re = 1100-2300  Circular tube (copper) D = 3.97 mm L = 2m	<ul style="list-style-type: none"> <li>Convective heat transfer enhancement increases with nanotube concentration and Re.</li> <li>Heat transfer enhancement is more appreciable in the entrance region and decreases with axial distance.</li> <li>Nanoparticles with larger aspect ratios lead to higher heat transfer enhancement.</li> </ul>	<ul style="list-style-type: none"> <li>Thermal conductivity accounts for a small portion of observed heat transfer enhancement.</li> <li>Nanofluids improve surface wettability which may help to enhance heat transfer.</li> <li>Particle migration and non-uniform shear may lead to particle depletion and shear thinning which reduce the effective viscosity near the wall and enhance heat transfer.</li> </ul>
Williams et al.[37]	Al <sub>2</sub> O <sub>3</sub> -water Zr O <sub>2</sub> -water	Al <sub>2</sub> O <sub>3</sub> - 46 nm 0.9, 1.8, 3.6 v%  ZrO <sub>2</sub> - 60 nm 0.2, 0.5, 0.9 v%	Forced convection Re = 9000-6300  Circular tube (stainless steel) D = 9.4 mm L = 2.819m	<ul style="list-style-type: none"> <li>The Maxwell-Garnett model [42] brackets the measured thermal conductivity.</li> <li>The Dittus-Boelter correlation predicts the measured Nu within ±10% if temperature- and concentration-dependent properties are used.</li> <li>The Blasius correlation predicts the measured pressure drop data to within ±20%.</li> </ul>	<ul style="list-style-type: none"> <li>Conventional theory can reliably predict thermal transport with nanofluids as long as the effective properties of nanofluids are used.</li> </ul>
Putra et al.[53]	Al <sub>2</sub> O <sub>3</sub> -water CuO-water	Al <sub>2</sub> O <sub>3</sub> - 131.2 nm CuO - 87.3 nm 1-4 v%	Natural convection	<ul style="list-style-type: none"> <li>Nanofluids behave as Newtonian fluids between 1% and 4% particle concentration.</li> <li>Heat transfer decreases with increasing particle concentration. The deterioration increases with aspect ratio of the flow cavity.</li> <li>Decrease in convective heat transfer is worse for CuO-water than Al<sub>2</sub>O<sub>3</sub>-water.</li> </ul>	—

Reference	Nanofluid	Particle Size and Concentration	Experimental Conditions	Key Findings	Mechanisms and Models
Duangthongsuk and Wongwises[54]	TiO <sub>2</sub> -water	21 nm 0.2 v%	Forced convection Re = 5000-17000  Circular tube (copper) D = 8.13 mm L = 1.5 m	<ul style="list-style-type: none"> <li>Thermal properties (specific heat, viscosity and thermal conductivity) are calculated from various models and are found to be drastically different.</li> <li>The selection of property model has little effect on predicted Nusselt number and heat transfer coefficient. The reason is attributed to low nanoparticle concentration.</li> </ul>	—
Jung et al.[62]	Al <sub>2</sub> O <sub>3</sub> -water Al <sub>2</sub> O <sub>3</sub> -(50% water + 50% ethylene glycol)	170 nm 0.6, 1.8, 2.4 v%	Forced convection Re = 5-300  Rectangular microchannels (Si) 50 × 50 μm <sup>2</sup> 100 × 100 μm <sup>2</sup>	<ul style="list-style-type: none"> <li>Convective heat transfer coefficient increases with nanoparticle concentration and Re.</li> <li>Entrance effect is more pronounced at high Re.</li> <li>Nusselt number in microchannels is no longer constant in laminar flow regime and is considerably less than theoretical predictions.</li> <li>Pressure drop can be predicted by the Blasius correlation.</li> </ul>	<ul style="list-style-type: none"> <li>A modified Dittus-Boelter correlation is proposed. <ul style="list-style-type: none"> <li><math>Nu = 0.014 \phi^{0.095} Re^{0.4} Pr^{0.6}</math></li> </ul> </li> </ul>
Wen and Ding[55]	TiO <sub>2</sub> -water (HNO <sub>3</sub> and NaOH added, pH = 3)	170 nm 0.19-0.57 v%	Natural convection GrPr = 20,000-200,000  Circular discs (Aluminum) D = 240 mm separated by a 10-mm gap	<ul style="list-style-type: none"> <li>Nusselt number decreases with increasing nanoparticle concentration, suggesting a different heat transfer mechanism for natural convection of nanofluids.</li> </ul>	<ul style="list-style-type: none"> <li>Reasons for heat transfer deterioration <ul style="list-style-type: none"> <li>Increase in viscosity <math>\mu_f = 13.47 \mu_0 e^{35.98\phi}</math>;</li> <li>Lack of inter-particle interaction due to low pH value needed to stabilize nanofluids; and</li> <li>Sedimentation of nanoparticle aggregates on heating surface creating extra thermal resistance.</li> </ul> </li> </ul>

Reference	Nanofluid	Particle Size and Concentration	Experimental Conditions	Key Findings	Mechanisms and Models
Nnanna[56]	Al <sub>2</sub> O <sub>3</sub> -water	22 nm 0.002-0.079 v%	Natural convection Ra = 10 <sup>7</sup> -3 × 10 <sup>7</sup>  35 mm × 40.32 mm × 215 mm aluminum cavity	<ul style="list-style-type: none"> <li>• Thermal response of nanofluids shows similar temporal and spatial evolution of temperature profile to that of the base fluid.</li> <li>• Rayleigh number decreases with increasing particle concentration, due to reduction in volumetric expansion coefficient and increase of viscosity.</li> <li>• Effective Nu increases at small particle concentration (0.2 ≤ φ ≤ 2%), and decreases for higher particle concentrations (φ ≥ 2%).</li> </ul>	<ul style="list-style-type: none"> <li>• A correlation for effective Nu is proposed</li> </ul> $Nu = \Gamma e^{-Ra \lambda (e^{-m\phi})}$

**Table 3. 1 (b) Single-Phase Convective Heat Transfer with Nanofluids (Numerical Studies).**

Reference	Problem Settings	Assumptions	Thermal Properties	Key Findings
Khanafer [57]	Natural convection in a 2D enclosure	<ul style="list-style-type: none"> <li>• Newtonian, incompressible and laminar flow</li> <li>• Nanofluids treated as a single-phase fluid</li> <li>• Boussinesq approximation used for thermal properties</li> </ul>	<ul style="list-style-type: none"> <li>• Viscosity computed using Brinkman model</li> <li>• Effective thermal conductivity taken as sum of effective stagnant thermal conductivity and enhancement due to thermal dispersion</li> </ul>	<ul style="list-style-type: none"> <li>• Temperature and velocity profiles show that nanofluids behave more like a single-phase fluid than a solid-fluid two-phase mixture.</li> <li>• Natural convective heat transfer is enhanced at all Grashof numbers and increases with increasing particle concentration.</li> <li>• Nanoparticles change flow structure dramatically.</li> <li>• Selection of thermal-property models substantially impact simulation of nanofluids heat transfer.</li> <li>• Heat transfer correlation proposed for natural convection of nanofluids in 2D cavity:  <math display="block">Nu = 0.5163(0.4436 + \phi^{1.0809})Gr^{0.3123} (10^3 \leq Gr \leq 10^5, 0 \leq \phi \leq 25\%)</math> </li> </ul>
Santra et al. [63, 69]	Natural convection in a 2D square enclosure	<ul style="list-style-type: none"> <li>• Steady, incompressible and laminar flow</li> <li>• Non-Newtonian</li> <li>• Boussinesq approximation for thermal properties</li> <li>• Nanofluids treated as a single-phase fluid</li> </ul>	<ul style="list-style-type: none"> <li>• Shear stress and shear rate calculated from Ostwald-de Waele model [43]</li> <li>• Thermal conductivity determined from Patel model [44] and treated as temperature-dependent</li> </ul>	<ul style="list-style-type: none"> <li>• Natural convective heat transfer decreases considerably for increase in nanoparticle concentration for all Rayleigh numbers simulated.</li> </ul>
Abu-Nada et al. [64]]	Natural convection in a 2D concentric annulus	<ul style="list-style-type: none"> <li>• Same as in [28]</li> </ul>	<ul style="list-style-type: none"> <li>• Thermal conductivity is calculated using Hamilton-Crosser model [48]</li> </ul>	<ul style="list-style-type: none"> <li>• Heat transfer is enhanced by nanoparticles with high thermal conductivity at high Rayleigh number.</li> <li>• Heat transfer deteriorates with nanoparticles of low thermal conductivity at intermediate Rayleigh number.</li> </ul>

Reference	Problem Settings	Assumptions	Thermal Properties	Key Findings
Maiga et al. [65]	Forced convective flow in a circular tube  Boundary condition: Uniform heat flux	<ul style="list-style-type: none"> <li>• Nanofluids treated as a single-phase fluid</li> <li>• Steady state and incompressible</li> <li>• k-ε model used for turbulent flow</li> </ul>	<ul style="list-style-type: none"> <li>• Density and specific heat averaged over concentration</li> <li>• Viscosity and thermal conductivity obtained by curve-fitting experimental data in the literature</li> </ul>	<ul style="list-style-type: none"> <li>• Convective heat transfer is enhanced in both laminar and turbulent flows and the enhancement increases along the streamwise direction at high particle concentration.</li> <li>• Wall shear stress increases with increasing particle concentration, but the increment becomes independent of Re for turbulent flow.</li> <li>• Al<sub>2</sub>O<sub>3</sub>-ethylene glycol offers much better heat transfer enhancement than Al<sub>2</sub>O<sub>3</sub>-water.</li> </ul>
Maiga et al. [66]	Forced convective flows in a circular tube and a radial channel (two parallel coaxial disks)	<ul style="list-style-type: none"> <li>• Same as in [65]</li> <li>• Only laminar flow considered</li> </ul>	<ul style="list-style-type: none"> <li>• Same as in [65]</li> </ul>	<ul style="list-style-type: none"> <li>• Convective heat transfer increases with particle concentration and the enhancement decreases along the streamwise direction.</li> <li>• Wall shear stress increases with increasing particle concentration.</li> <li>• Al<sub>2</sub>O<sub>3</sub>-ethylene glycol offers much better heat transfer enhancement than Al<sub>2</sub>O<sub>3</sub>-water.</li> </ul>
Maiga et al. [67]	Same as in [65]	<ul style="list-style-type: none"> <li>• Same as in [65]</li> </ul>	<ul style="list-style-type: none"> <li>• Same as in [65]</li> </ul>	<ul style="list-style-type: none"> <li>• Convective heat transfer is enhanced by nanofluids, and the enhancement increases along the streamwise direction.</li> <li>• A heat transfer correlation proposed for fully developed turbulent flow</li> </ul> $Nu_{fd} = 0.085 Re^{0.71} Pr^{0.35}$

**Table 3. 1 (c) Single-Phase Convective Heat Transfer with Nanofluids (Theoretical Studies).**

Reference	Subject	Assumptions	Procedures	Key Findings
Wen and Ding [58]	Effect of particle migration on convective heat transfer of nanofluids in minichannels	<ul style="list-style-type: none"> <li>• Steady-state fully developed pressure driven flow</li> <li>• Constant temperature or heat flux boundary conditions</li> </ul>	<ul style="list-style-type: none"> <li>• Total flux of nanoparticle migration in radial direction consists of the fluxes due to viscosity gradient, non-uniform shear rate, and Brownian motion, all related to volume concentration.</li> <li>• Viscosity and thermal conductivity dependent on volume concentration.</li> </ul>	<ul style="list-style-type: none"> <li>• Relative importance of shear/viscosity-induced heterogenization to Brownian diffusion-induced homogenization determines particle migration.</li> <li>• Non-uniform distribution of particles occurs over pipe cross-section for high Pe with particle concentration decreasing outwards from the center.</li> <li>• Non-uniform effective thermal conductivity distribution occurs due to concentration profile.</li> <li>• Nu increases with increasing Pe and particle concentration.</li> </ul>
Mansour et al. [59]	Effect of assessment of nanofluid properties on thermohydraulic performance of convective heat transfer	<ul style="list-style-type: none"> <li>• Steady-state fully developed pressure driven flow</li> <li>• Constant heat flux boundary condition</li> </ul>	<ul style="list-style-type: none"> <li>• Thermal properties assessed using models in the literature.</li> <li>• Pumping power and temperature difference between wall and bulk fluid calculated and compared for different thermal property models selected.</li> </ul>	<ul style="list-style-type: none"> <li>• Calculation of operational conditions (required pumping power for given heat transfer rate) or design parameters (required channel length for given flow rate and bulk temperature rise) strongly depends on the selection of thermal property models.</li> </ul>
Kim et al. [60]	Natural convection instability and heat transfer characteristics of nanofluids	<ul style="list-style-type: none"> <li>• Neglect Marangoni and Soret effects</li> </ul>	<ul style="list-style-type: none"> <li>• A correction factor used to characterize effects of nanofluid concentration and thermal properties on Rayleigh number and heat transfer coefficient.</li> </ul>	<ul style="list-style-type: none"> <li>• Natural convective heat transfer enhanced in nanofluids at all particle concentrations.</li> </ul>

---

Hwang et al. [61]	Natural convection instability and heat transfer characteristics of nanofluids in a rectangular cavity heated from below	<ul style="list-style-type: none"> <li>• Nanofluids follow Newtonian behavior</li> <li>• Rayleigh number and Nu calculated using same functional form as that of the base fluid but with effective thermal properties</li> </ul>	<ul style="list-style-type: none"> <li>• Thermal properties of nanofluids are assessed using various models in the literature.</li> <li>• Rayleigh number and Nusselt numbers calculated and compared based on different selections of viscosity and thermal conductivity models.</li> </ul>	<ul style="list-style-type: none"> <li>• Rayleigh number of nanofluids is lower than that of the base fluid for given temperature condition, making nanofluids more stable than the base fluid.</li> <li>• Ra decreases with increasing particle concentration due to increase of effective viscosity and thermal conductivity, which tend to stabilize the fluid in natural convection.</li> <li>• Ra increases with increasing particle size which decreases the effective viscosity and thermal conductivity.</li> <li>• Calculated heat transfer coefficient either decreases or increases with increasing particle concentration, depending on selection of viscosity and thermal conductivity models.</li> <li>• Natural convection heat transfer coefficient deteriorates with addition of nanoparticles according to Pak and Cho's correlation [46] for viscosity.</li> </ul>
-------------------	--	--	--	---

---

To further investigate the thermal transport mechanism, a few experimental studies on the single-phase pressure drop and convective heat transfer of nanofluids have been reported in the literature since 2009. Some selected ones will be briefly reviewed with the emphasis on assessing the applicability of conventional heat transfer correlations for and on exploring the heat transfer enhancement mechanisms in nanofluids. Hwang et al. [70] studied the pressure drop and convective heat transfer of  $\text{Al}_2\text{O}_3$ -water nanofluids in fully developed laminar flow ( $\text{Re} < 800$ ). The measured friction factor is in good agreement with the prediction from the Hagen-Poiseuille equation, but the substantial enhancement in convective heat transfer coefficient cannot be correlated by the Shah equation. Using a scaling analysis, it was shown that the heat transfer enhancement should be attributed to the modification of the velocity profile due to Brownian diffusion and thermophoresis, rather than the enhanced thermal conductivity and the direct energy transfer by the nanoparticle dispersion. Anoop et al. [39] conducted convective heat transfer experiments in the laminar developing region ( $300 < \text{Re} < 2200$ ) using  $\text{Al}_2\text{O}_3$ -water nanofluids with two nanoparticle sizes. The nanofluid with smaller nanoparticles exhibits higher heat transfer coefficient. The heat transfer enhancement in the entrance region exceeds that in the nearly developed region. It was postulated that these observations are caused by the property change in the developing region as well as the particle migration. Lai et al. [71] presented an experimental study of convective heat transfer of  $\text{Al}_2\text{O}_3$ -water nanofluids in both the developing and fully developed laminar regions. The results show the heat transfer coefficient increases with the flow rate and the nanoparticle volume concentration. The heat transfer enhancement is greater in the developing region and decreases along the axial locations, owing in part to the thinning

of thermal boundary layer in the nanofluids. The heat transfer enhancement in the fully developed region was attributed to the flattening of the velocity profile due to the shear-induced particle migration [49, 72]. Sharma et al. [73] studied the convective heat transfer of Al<sub>2</sub>O<sub>3</sub>-water nanofluids in the transition flow region ( $3500 < Re < 9000$ ) in a tube with and without twisted tape inserts. Buongiorno et al. [74, 75] investigated convective heat transfer of Al<sub>2</sub>O<sub>3</sub>-water and ZrO<sub>2</sub>-water nanofluids in both the laminar ( $140 < Re < 1900$ ) and fully developed turbulent regions ( $9000 < Re < 63,000$ ). The pressure drop and Nusselt number were found to be predicted well by conventional models as long as the concentration- and temperature-dependent thermophysical properties were considered for the nanofluids. The authors concluded the heat transfer enhancement was simply caused by the changes in thermophysical properties and the nanofluids can be treated as a homogeneous mixture. In their experimental investigation of turbulent convection heat transfer, Torri and Yang [76] observed significant heat transfer enhancement in aqueous suspensions of nanodiamond particles, and concluded the reduced thermal boundary layer thickness, the thermal conduction under dynamic conditions and the particle migration may be responsible for the heat transfer enhancement. Duangthongsuk and Wongwises [77] experimentally investigated the convective heat transfer of TiO<sub>2</sub>-water nanofluids in turbulent flow ( $4000 < Re < 16,000$ ). They observed that the heat transfer coefficient decreases with increasing nanoparticle concentration, and at the highest concentration, it can drop below that of the base fluid. It was postulated that the effect of increased viscosity may override the enhancement in thermal conductivity, thereby leading to a decrease in the heat transfer performance. Besides the foregoing studies conducted in a single tube configuration, convective heat

transfer of nanofluids has also been investigated in microchannel heat sinks. Jung et al. [62] reported the pressure drop and convective heat transfer measurements of nanofluids in a microchannel heat sink under laminar flow conditions ( $Re < 300$ ). The measured Nusselt number was considerably lower than the theoretical prediction for fully developed laminar flow ( $Nu = 4.36$ ) and can be correlated well with a modified Dittus-Boelter correlation. Wu et al. [78] carried out an experimental study on the laminar flow and heat transfer of  $Al_2O_3$ -water nanofluids in a silicon microchannel heat sink. It was found that the Nusselt number increases with the increase in the nanoparticles concentration,  $Re$  and Prandtl number ( $Pr$ ).

From the literature survey, it is clear that the mechanisms for convective heat transfer enhancement in nanofluids still remain mysterious. The flow-induced particle migration has been attributed by several groups as a possible key mechanism for the enhanced laminar heat transfer in nanofluids. In this model, the balance of particle fluxes, due to the Brownian diffusion and the variations in local shear rate and viscosity, respectively, is considered in deriving the radial distribution of particles in an originally homogeneous flow field. The resulting non-uniform particle distribution gives rise to modified velocity and thermophysical property profiles in the channel, which serve to enhance the heat transfer. Physically, the particle migration concept is to assume the nanofluids are a heterogeneous solid-fluid two-phase mixture. Its success in predicting the laminar flow and heat transfer suggests the particle-fluid interaction missing in the widely-used homogeneous mixture model of nanofluids should be explored further to reveal the fundamental mechanisms of thermal transport in nanofluids. Additionally, the previous studies were performed for either laminar flow or fully developed turbulent flow

at very high  $Re$ , and there is a gap in the knowledge of the convective flow and heat transfer of nanofluids in the transition region ( $2200 < Re < 3500$ ).

### 3.2 CONVECTIVE FLOW AND HEAT TRANSFER

#### 3.2.1 EXPERIMENTAL APPARATUS

The experimental apparatus is schematically shown in Figure 3. 1. A gear pump (IDEX Micropump 67-GA-V21) was used to circulate the nanofluid through the test loop. The flow rate was measured by a turbine flowmeter (McMillan G111). A liquid-liquid heat exchanger (Lytron LL520G14) was used in conjunction with an air-cooled chiller (Neslab MERLIN 25) to reduce the temperature of the heated nanofluid to room temperature before it flows back to the reservoir. Readings of the flow rate, temperature and pressure measurements were collected by a data acquisition system (Agilent 34970A) and processed in a computer.

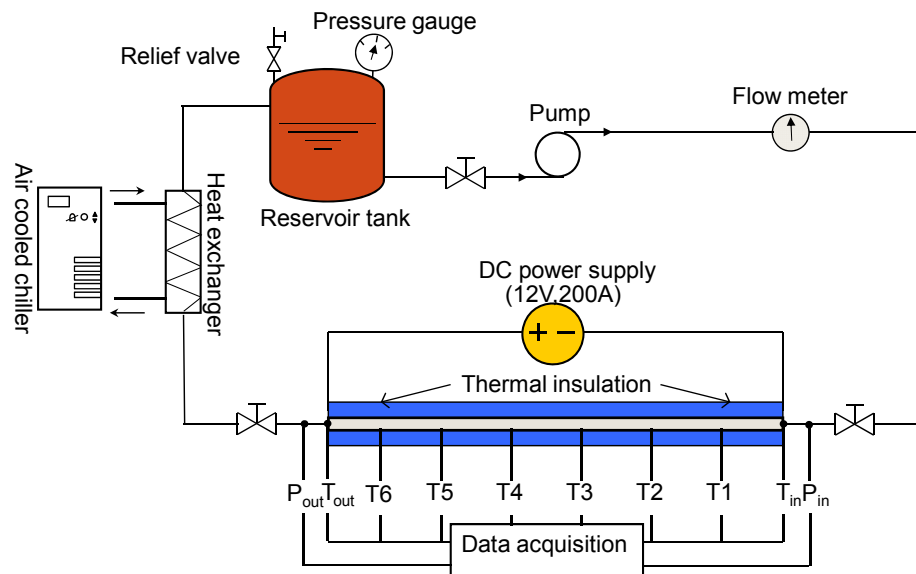


**Figure 3. 1.** Schematic of the experimental apparatus.

The test section is a circular minichannel made of stainless steel, which measures 1.09 mm in inner diameter and 0.25 mm in wall thickness. The total length is 306 mm ( $L/D = 281$ ). The test section is resistively heated by passing a DC current through it. For this purpose, it was connected to a DC power supply (Dynatronix CRS12-200) via two copper electrical connectors. The voltage drop across the minichannel was measured directly by the data acquisition system, and the current was obtained using an accurate shunt resistor. Six copper-constantan (T-type) thermocouples (Omega 5TC-TT-T40-36) were attached to the outer wall of the tube at 44 mm axial intervals (TC1 through TC6). The temperature readings from these thermocouples were extrapolated to yield the local temperatures at the inner wall. In order to minimize the heat loss to the ambient, the minichannel was wrapped in three layers of thermal insulating materials. The test section was connected to the flow loop with two plexiglass connectors which provide both electrical and thermal isolation from the rest of the loop. Two thermocouple probes (Omega TMT IN-020G-6) were accommodated in the plexiglass connectors to measure the fluid temperatures at the inlet and outlet of the channel. Two absolute pressure transducers (Omega PX319-050A5V and PX319-030A5V) were installed to measure the pressure drop across the minichannel.

### **3.2.2 TEST PROCEDURES**

Prior to each experiment run, the nanofluid was freshly prepared following the dispersing processes described before. In the pressure drop experiments, the flow rate was adjusted by a control valve. After the flow rate and the pressure signals stabilized, the data were read into the data acquisition system. The flow rate was then increased in small increments and the procedure repeated. In the heat transfer experiments, the power

input to the test tube was maintained at a constant level. The flow rate was first set to the maximum value and gradually decreased in subsequent experiments. Each steady-state value was calculated as an average of 100 readings for all flow rate, pressure, temperature, and power measurements. The Reynolds number obtained in this work ranges from 600 to 4500.

### 3.2.3 DATA REDUCTION

The pressure drop and flow rate were measured to obtain Re and the Darcy friction factor  $f$ , which are defined as

$$\text{Re} = \rho u D / \mu , \quad (3.1)$$

$$f = \frac{(\Delta P / L) D}{\rho u^2 / 2} . \quad (3.2)$$

It is noted that  $\Delta P$  in Eq. (3.2) is the pressure drop across the channel length and is calculated by subtracting the inlet and outlet pressure losses from the measured overall pressure drop [79, 80].

#### Heat Transfer

It is reasonable to assume a constant heat flux boundary condition on the channel wall, since the resistive heating method is used in this work. The wall heat flux can be calculated from the sensible heat gain by the fluid

$$q'' = \rho_f Q c_p (T_{f,out} - T_{f,in}) / A , \quad (3.3)$$

where the fluid properties are evaluated at the mean temperature

$$\bar{T}_f = (T_{f,in} + T_{f,out}) / 2 . \quad (3.4)$$

The local convective heat transfer coefficient is defined as

$$h(x) = q'' / [T_w(x) - T_f(x)] , \quad (3.5)$$

where the local wall temperature  $T_w$  is extrapolated from the temperature reading of  $T_{w,o}$  obtained at the outer wall of the minichannel following [81]

$$T_w(x) = T_{w,o}(x) + \frac{\rho_f Q C_p (T_{f,out} - T_{f,in})}{4\pi k_w L} - \frac{\rho_f Q C_p (T_{f,out} - T_{f,in}) D_o^2}{2\pi k_w (D_o^2 - D^2) L} \ln \frac{D_o}{D}. \quad (3.6)$$

Assuming the local fluid temperature follows a linear profile along the channel length,  $T_f$  can be calculated from the energy conservation

$$T_f(x) = T_{f,in} + q'' \pi D x / (\rho_f Q C_p). \quad (3.7)$$

Similarly, the average heat transfer coefficient is determined from

$$\bar{h} = q'' / [\bar{T}_w - \bar{T}_f], \quad (3.8)$$

where the average wall temperature is  $\bar{T}_w = \frac{1}{5} \sum_{i=1}^5 T_w(i)$  and the fluid temperature is calculated from Eq.(3.4) .

The Nusselt number can be calculated as

$$Nu = \frac{h \cdot D}{k}. \quad (3.9)$$

This definition applies for both the local and average Nusselt numbers, and the thermal conductivity is evaluated at the corresponding fluid temperatures.

### 3.2.4 MEASUREMENT UNCERTAINTIES

The temperature measurement uncertainty was  $\pm 0.3^\circ\text{C}$ . The uncertainty in the flow rate measurements was 1%. The error associated with the pressure transducers was 2%. A standard error analysis [82] revealed the uncertainties in the reported Reynolds number, friction factor and heat transfer coefficient were in the range of 5.8 – 28.9% and 2.2 – 9.6%, respectively.

### 3.2.5 EXPERIMENTAL RESULTS WITH WATER

Control experiments were first performed with the base fluid (water) to verify the integrity of the experimental facility and the test procedures. The results also provide the baseline information of the single-phase thermal transport of nanofluids in a circular minichannel.

The friction factor measurements were compared to predictions from conventional theory for fluid flow in a circular channel. In the laminar region, the Hagen-Poiseuille equation [81] was used for hydrodynamically fully developed flow condition

$$f \cdot \text{Re} = 64, \quad (3.10)$$

and the Shah equation [83] was used to account for the developing length effect

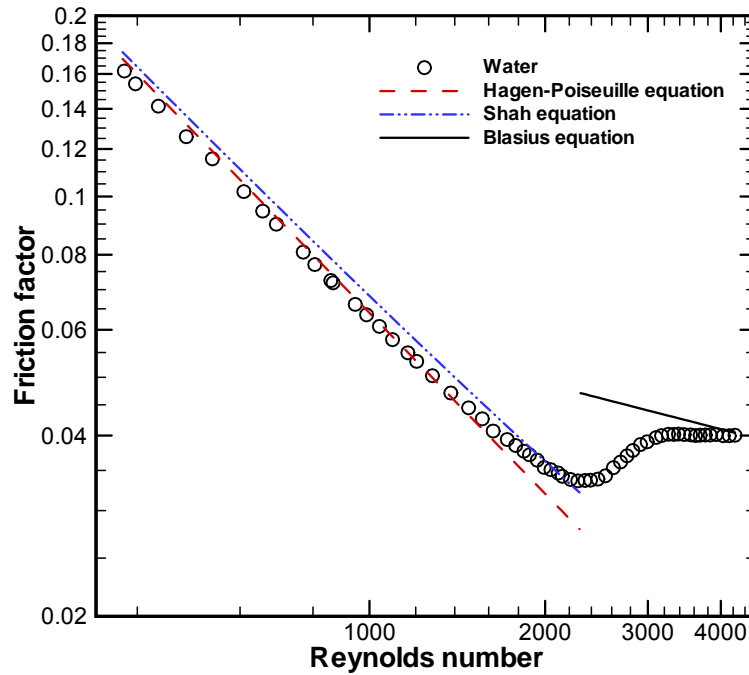
$$f_{app} \text{Re} \approx 4 \left( \frac{3.44}{\sqrt{\zeta}} + \frac{16 + 0.3125\zeta - 3.44/\sqrt{\zeta}}{1 + 2.12 \times 10^{-4} / \zeta^2} \right), \quad (3.11)$$

where  $\zeta = (x/D)/\text{Re}$ . For fully developed turbulent flow, the predictions were obtained from the Blasius solution [81]

$$f = 0.316 / \text{Re}^{0.25} \quad (\text{Re} < 2 \times 10^4). \quad (3.12)$$

Figure 3. 2 shows the measured friction factor of water as a variation of  $\text{Re}$ . At relatively low  $\text{Re}$  ( $< 1000$ ), the hydrodynamic entrance length ( $L^+ = 0.056 \text{ Re} \cdot D$ ) is only a small fraction of the total channel length ( $L^+/L < 0.20$ ), and the entrance region effect is minor. Hence the experimental data agree excellently with the Hagen-Poiseuille equation. Once  $\text{Re}$  exceeds 1500, the entrance region effect can no longer be neglected ( $L^+/L \sim 0.30$ ). Consequently, the friction factor starts to deviate from the fully developed flow and gradually approaches the hydrodynamically developing flow described by Eq. (3.11).

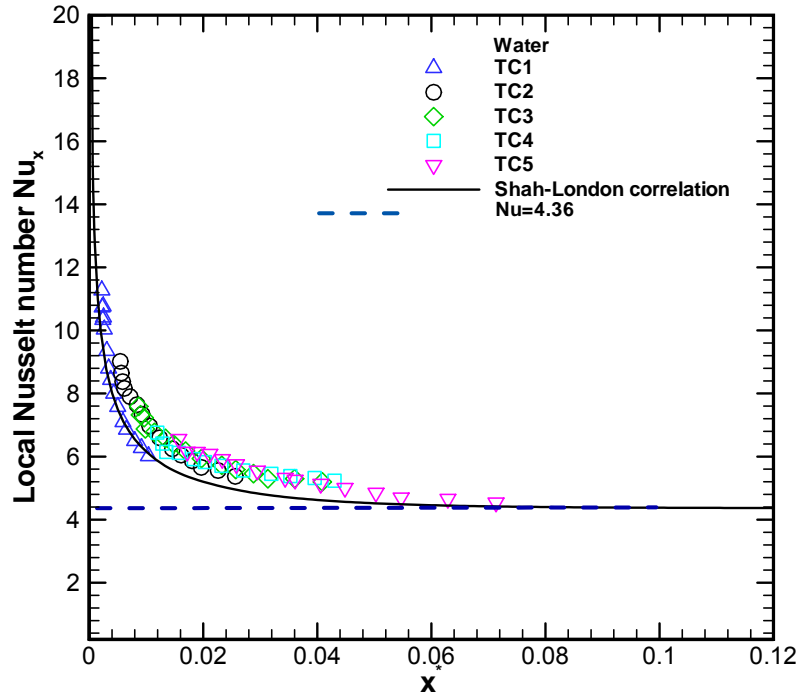
Further, Figure 3. 2 shows the transition from laminar to turbulent flow occurs at  $Re_{cr} \approx 2300$  and the transition region persists to  $Re \approx 3200$  where the fully developed turbulent flow begins to establish.



**Figure 3. 2.** Friction factor vs. Reynolds number (water).

The local Nusselt number measurements are depicted in Figure 3. 3 as a function of  $x^*$  ( $x^* = x/(D Re Pr)$ ). The entrance region behavior can be clearly identified. Nusselt numbers are, in principle, infinite at  $x^* = 0$ , and rapidly decay to their asymptotical (fully developed) value, i.e.,  $Nu = 4.36$ . The experimental data can be reasonably represented by the Shah-London correlation [68].

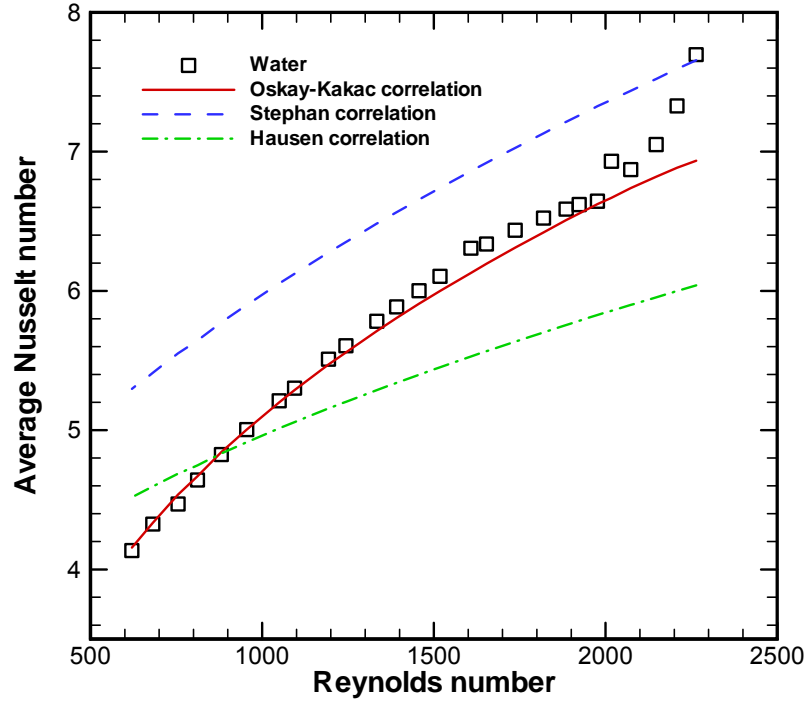
$$Nu_x = \begin{cases} 1.302 / (x^*)^{1/3} - 1 & \text{for } x^* \leq 0.00005 \\ 1.302 / (x^*)^{1/3} - 0.5 & \text{for } 0.0005 \leq x^* \leq 0.0015. \\ 4.364 + 8.68(1000x^*)^{-0.506} e^{-41x^*} & \text{for } x^* \geq 0.0015 \end{cases} \quad (3.13)$$



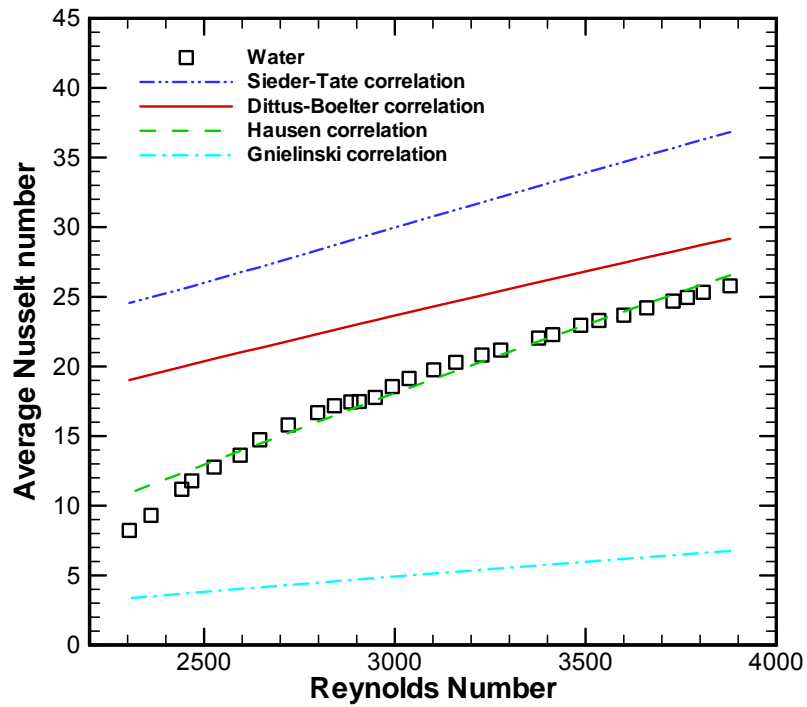
**Figure 3. 3.** Local Nusselt number vs. the  $x^*$  (water, heat flux  $q'' = 6.5 \text{ kW/m}^2$ ).

Figure 3. 4 presents the measured average Nusselt number as a function of  $Re$ . Predictions from some established heat transfer correlations for convective flow in a circular channel are also included for comparison purpose. The heat transfer correlations are enumerated in Table 3. 2, together with their corresponding hydrodynamic and thermal conditions and the applicable range. Figure 3. 4(a) shows that in the laminar region, the measured data of Nusselt number are in good agreement with the prediction from the Oskay-Kakac correlation, while the other laminar heat transfer correlations

provide much less satisfactory prediction of the experimental data. The transition to turbulent flow at  $Re_{cr} \approx 2300$  can also be found in Figure 3. 4 (a). Figure 3. 4(b) demonstrates that, among the turbulent heat transfer correlations, the Hausen correlation for thermally developing turbulent flow is the best in predicting the experimental data. The successes of the Oskay-Kakac and Hausen correlations can be attributed to the close match between their founding conditions and the present experiments.



(a)



(b)

**Figure 3. 4.** Average Nusselt number vs. Reynolds number  
(water, heat flux  $q'' = 6.5 \text{ kW/m}^2$ ).

**Table 3. 2. Selected conventional heat transfer correlations from the literature**

Correlation	Conditions	Range of validity
<b>Laminar Heat Transfer</b>		
Stephan correlation [84] $Nu = 4.364 + \frac{0.086(\text{Re Pr } D/L)^{1.33}}{1 + 0.1\text{Pr}(\text{Re } D/L)^{0.83}}$	Simultaneously developing (constant wall heat flux)	0.7 < Pr < 7 or Re Pr D/L < 33 for Pr > 7
Hausen correlation [81] $Nu = 3.66 + \frac{0.19(\text{Re Pr } D/L)^{0.8}}{1 + 0.117(\text{Re Pr } D/L)^{0.467}}$	Thermally developing (constant wall temperature)	Re < 2,200
Oskay-Kakac correlation [85] $Nu = 1.86(\text{Re Pr } D/L)^{1/3} \left( \frac{\mu_f}{\mu_w} \right)^{0.152}$	Thermally developing (constant wall heat flux)	800 < Re < 2,200 T <sub>w</sub> /T <sub>f</sub> < 3
<b>Turbulent Heat Transfer</b>		
Dittus-Boelter correlation [86] $Nu = 0.023\text{Re}^{0.8} \text{Pr}^{1/3}$	Fully developed turbulent	0.6 < Pr < 160 Re > 10,000, L/D > 10
Hausen correlation [87] $Nu = 0.116(\text{Re}^{2/3} - 125)\text{Pr}^{1/3} \left[ 1 + (D/L) \right]^{2/3} \left( \frac{\mu_f}{\mu_w} \right)^{0.14}$	Thermally developing turbulent	0.7 < Pr < 3 2,200 < Re < 10,000
Gnielinski correlation [88] $Nu = \frac{(f/8)(\text{Re}-1000)\text{Pr}}{1 + 12.7(f/8)^{1/2}(\text{Pr}^{2/3} - 1)}$ $f = \frac{1}{(1.82 \ln(\text{Re}) - 1.64)^2}$	Transitional and fully developed turbulent	3000 < Re < 5 × 10 <sup>4</sup>
Sieder-Tate correlation [89] $Nu = 0.027 \text{Re}^{0.8} \text{Pr}^{1/3} \left( \frac{\mu_f}{\mu_w} \right)^{0.14}$	Fully developed turbulent	0.7 < Pr < 16,700 Re > 10,000, L/D > 10

### 3.2.6 EXPERIMENTAL RESULTS FOR AL<sub>2</sub>O<sub>3</sub>-WATER NANOFLUIDS

Following similar test procedures, the pressure drop and convective heat transfer experiments were conducted for Al<sub>2</sub>O<sub>3</sub>-water nanofluids with volume concentrations of 1, 2, 3.5 and 5 v%, respectively.

Figure 3. 5 shows the measured friction factor for nanofluids as a function of  $Re$ . Several interesting features can be observed. First, in the laminar region, the friction factor of nanofluids shows an increasing trend with the volume concentration and is generally higher than that of pure water at the same  $Re$ . Second, at low  $Re$  where the flow field would be fully developed if water were the working fluid, the Shah equation for developing flows (Eq.(3.11)) outperforms the Hagen-Poiseuille equation (Eq. (3.10)) in predicting the friction factor of nanofluids. It suggests the entrance region in nanofluids is prolonged, or equivalently, the development of velocity boundary layer is retarded in nanofluids. Third, the onset of transition to turbulence is delayed in nanofluids. The transition occurs as the result of the amplified perturbations in the flow field that eventually trigger instability. While no strict theoretical limit exists for the critical  $Re$ , it is generally agreed that the onset of turbulence can occur at  $Re_{cr} = 2100 \sim 2300$  in a channel flow, unless special measures are taken to suppress the perturbations. Figure 3. 5 shows that, while  $Re_{cr}$  is almost exactly 2300 for water, it shifts toward a higher value as the nanofluid volume concentration increases. From the inset in Figure 3. 5,  $Re_{cr}$  reaches 2500 for the 5% nanofluid. Thus, the laminar flow behavior of nanofluids extends into the otherwise transition region for water ( $2300 < Re < 2500$ ), where the friction factor of nanofluids actually falls below that of water.

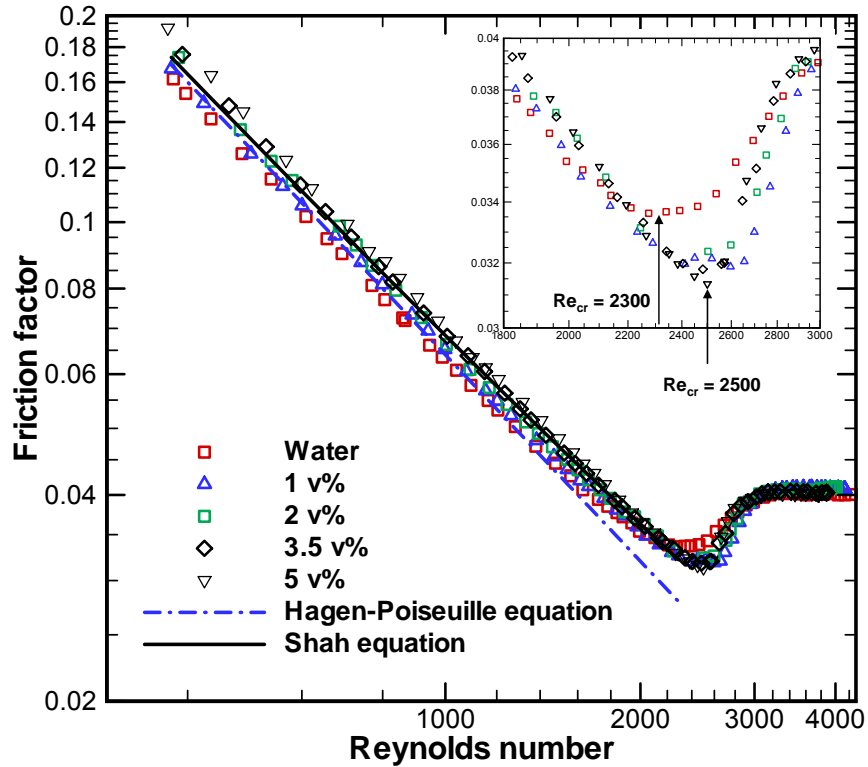


**Figure 3. 5.** Friction factor vs. Reynolds number for nanofluids at various volume concentrations.

The region with reduced friction factor further persists till fully developed turbulence begins to establish at  $Re \approx 3200$ . Afterward, the data for both nanofluids and water collapse together and become difficult to distinguish, indicating the vanishing influence of nanoparticles on the flow dynamics at high  $Re$ .

In the study of particle-laden turbulent flows, it has been long known that addition of small particles can modify the turbulence structures by changing the turbulent kinetic energy of the carrier fluid [90-92]. In particular, the changes in turbulent structure depend on the size of the particles relative to the length scale of turbulence, i.e., the Kolmogorov microscale,  $\eta$  [93-95]. Gore and Crowe [96] defined a critical parameter,  $d_p/\eta \approx 0.1$ , for gas-solid flows, above which turbulence intensity is enhanced and below

which it is attenuated. Hetsroni [97] also proposed that “small” particles suppress turbulence by acting as an additional source of dissipation, and “large” particles enhance turbulence due to wake shedding. Noticing the similarity between the friction factor results of nanofluids in Figure 3. 5 and the results obtained in particle-laden turbulent flows, it is interesting to examine, using a simple scaling analysis, the effect of the interaction between nanoparticle and the base fluid on the transition and turbulent flow behaviors.

The Kolmogorov microscale represents the finest structure in turbulence at which the kinetic energy is dissipated by viscosity, and can be estimated as

$$\eta \approx \frac{\nu}{u_{\tau}}. \quad (3.14)$$

where the wall shear velocity  $u_{\tau}$  is defined as  $u_{\tau} = (\tau_w / \rho_f)^{1/2}$ . The wall shear stress  $\tau_w$  can be obtained from the definition of the Darcy friction factor  $f = 8\tau_w / (\rho_f u^2)$  in conjunction with the Blasius equation (Eq. (3.12)). Now consider the experimental conditions in this study,  $D = 1.09$  mm,  $d_p = 135$  nm and  $\nu = 8.6 \times 10^{-7}$  m<sup>2</sup>/s for water, the relative sizes of  $d_p/\eta$  are found to be 0.003 and 0.005 for  $Re = 2550$  and 3200, respectively. It is noted that, while  $d_p/\eta \approx 0.1$  was originally proposed to determine the enhancement or attenuation of turbulence by particles in gas-solid flows, a smaller critical value can be expected for liquid-solid flows where the interaction between the liquid and the solid particles is much more intensive. Nevertheless, the above scaling analysis shows the nanoparticles should be considered “small” as compared to the length scale of turbulence ( $d_p/\eta \ll 0.1$ ) at  $Re < 3200$ , and the particle-fluid interaction will damp the instability and reduce the turbulence intensity and Reynolds stress in the flow. Consequently, the

transition to turbulence is delayed and the friction factor reduced to below that of the base fluid. As  $Re$  further increases, the Kolmogorov microscale will decrease as suggested by Eq. (3.14), and  $d_p/\eta$  will increase and eventually exceed the critical value. In that case, the nanoparticles become “large” with respect to the turbulence structures and the turbulent flow will be intensified. Due to the limit of the  $Re$  range in the present study, the intensified turbulence was not observed in Figure 3. 5, however, the recovery trend in the nanofluid data to that of the base fluid supports the arguments from the above analysis.

The local heat transfer coefficients measured for nanofluids at five axial locations (TC1 through TC5) are presented in Figure 3. 6 for  $Re = 870$  and  $1230$ , respectively. It can be found that convective heat transfer in nanofluids is enhanced and the increment increases in proportion to  $Re$  and the nanoparticle concentration. The heat transfer enhancement is more significant in the entrance region than at downstream locations. In Figure 3. 6 (a), the enhancement in heat transfer coefficient for the 5% nanofluid is 19% near the entrance and decreases to less than 9% near the channel exit. This trend also strengthens with increasing nanoparticle concentration and  $Re$ . The thermally developing flow shown in Figure 3. 6 is consistent with the pronounced hydrodynamic entrance region effect observed in Figure 3. 5.

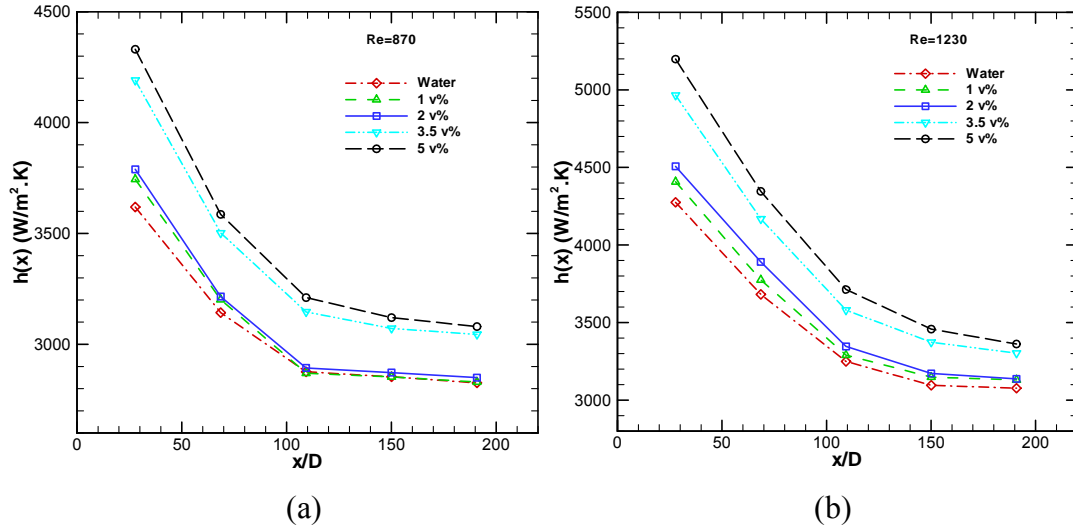


**Figure 3. 6.** Local convective heat transfer of nanofluids (heat flux  $q'' = 6.5 \text{ kW/m}^2$ ).

Figure 3. 7 shows the average Nusselt number for the nanofluids in the laminar region. The experimental data are bounded by predictions from the Oskay-Kakac correlation and the Stephan correlation, whereas the Hausen equation for laminar flow almost always underpredicts the measured data. Since the Oskay-Kakac correlation works well for the base fluid, its role as the lower bound in Figure 3. 7 for the measured nanofluid results, again, proves the heat transfer enhancement in nanofluids. As the nanoparticle concentration and Re increase, the convection in nanofluids is becoming more hydrodynamically and thermally developing, as manifested in Figure 3. 5 and Figure 3. 6. It is thus not surprising that the experimental data move toward the theoretical prediction from the Stephan correlation, which was developed for simultaneously developing flow conditions.

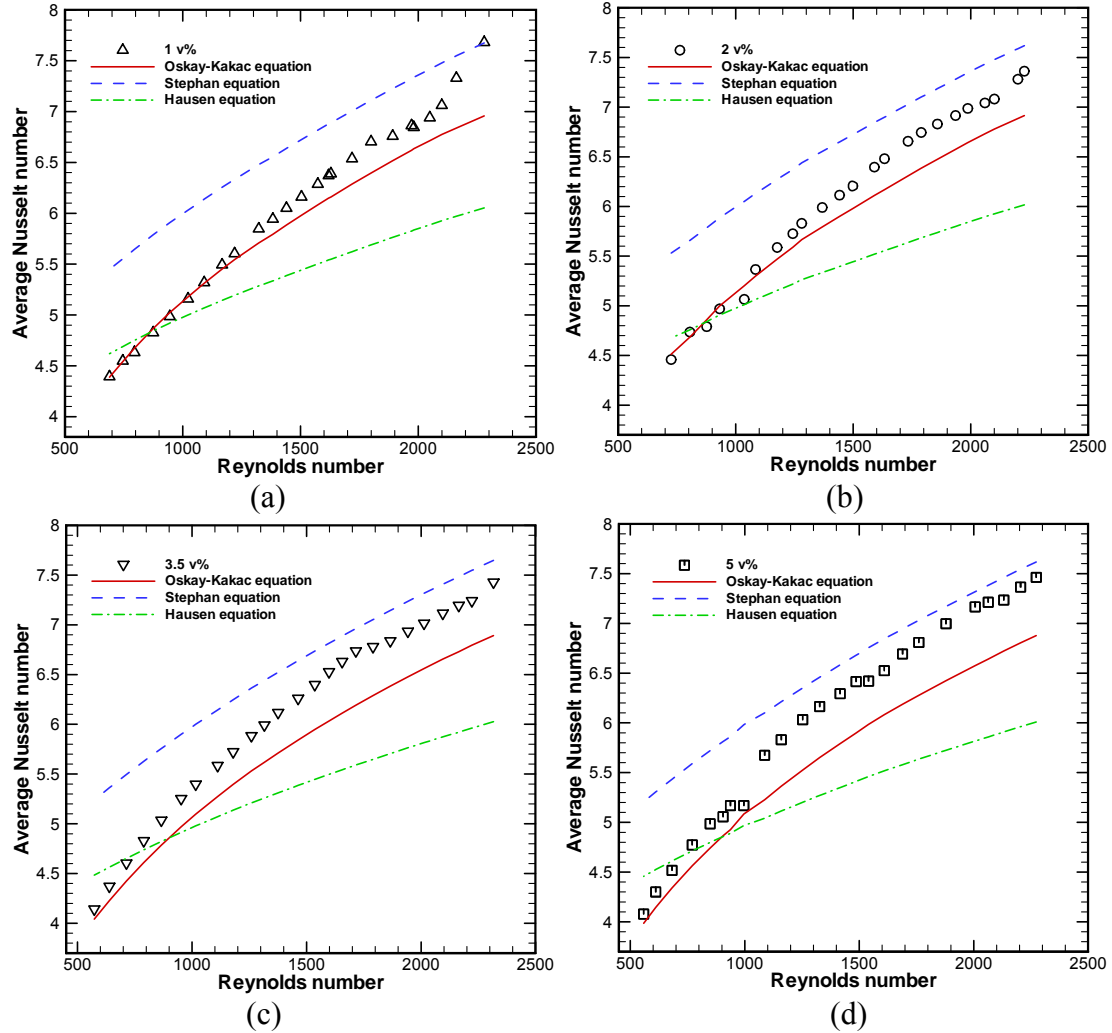


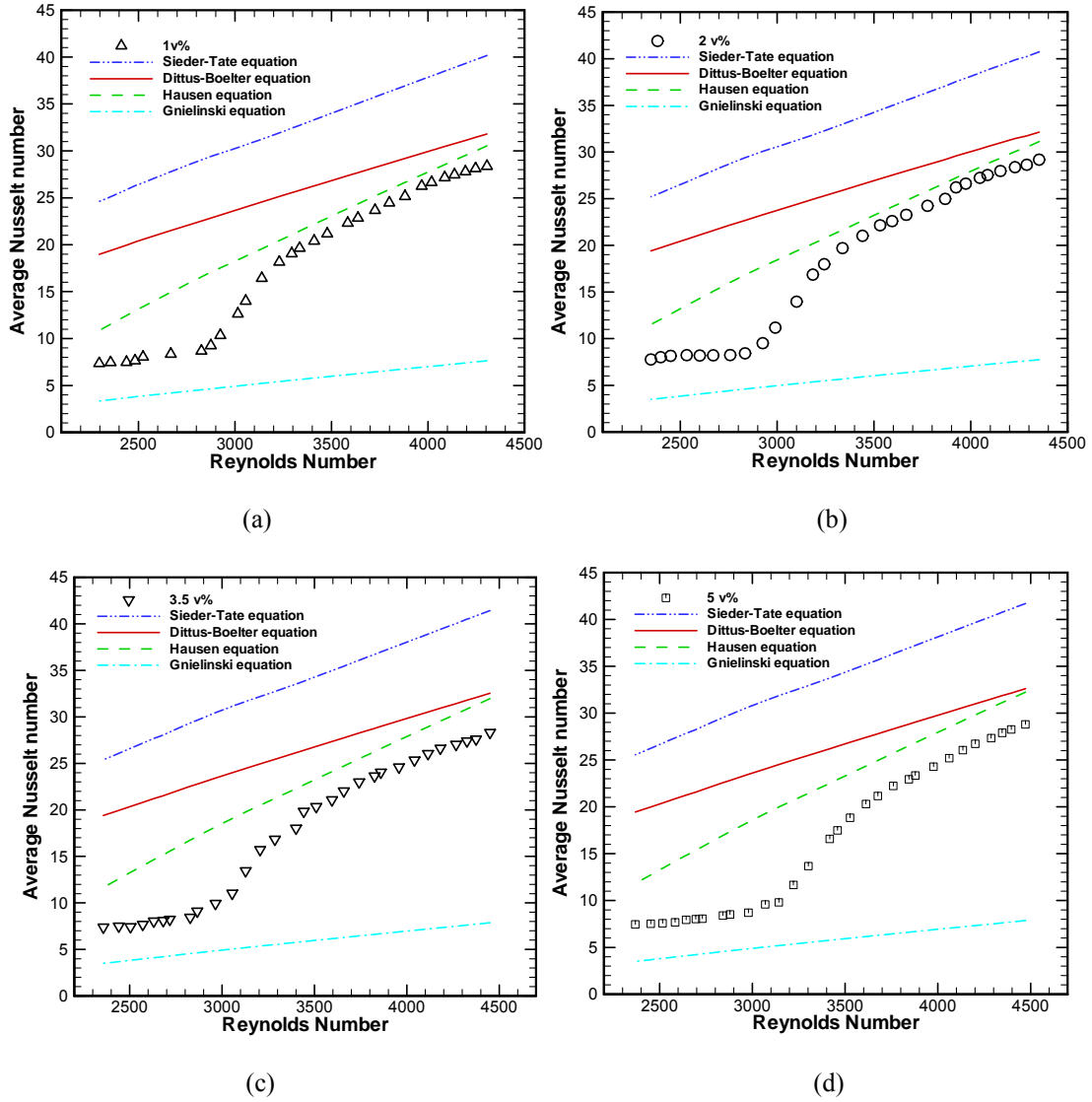
**Figure 3. 7.** Average Nusselt number vs. Reynolds number in the laminar flow region (heat flux  $q'' = 6.5 \text{ kW/m}^2$ ).

The average Nusselt number measured for the nanofluids in the transition and turbulent regions are presented in Figure 3. 8. As Re increases, there are two locations where the slope of the experimental data changes. The first one corresponds to the onset of transition to turbulence, and the second one is associated with the initial establishment of fully developed turbulent heat transfer. It can be observed that the delayed transition occurs at  $Re_{cr} \approx 2800$ . Throughout the transition and the early stage of fully developed turbulent regions (Re up to 4500), the measured Nusselt number falls short of the

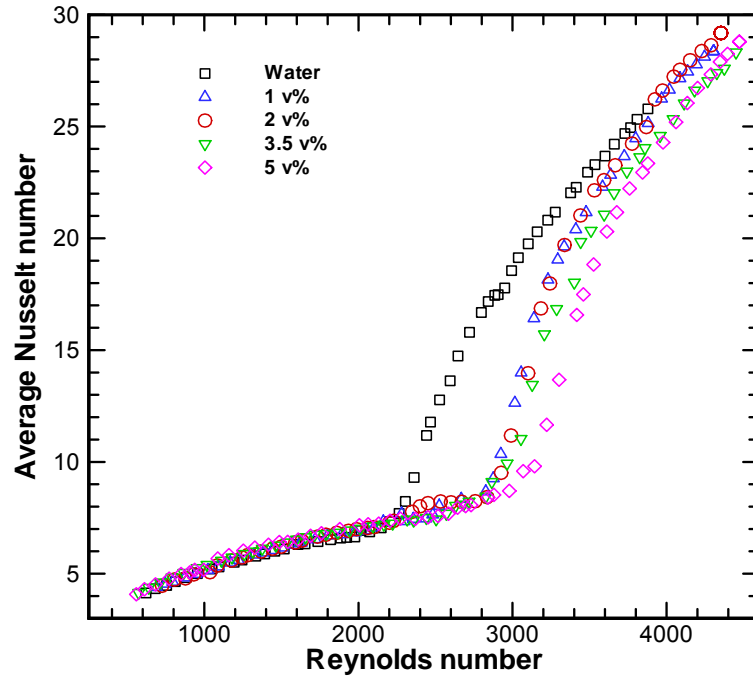
prediction from the Hausen equation, which represents the data of water well. Furthermore, the heat transfer reduction worsens as the nanoparticle concentration increases, as shown in Figure 3. 8 (a) through (d). It can be deduced that, rather than enhancing convective heat transfer, the presence of nanoparticles causes deterioration of heat transfer in the transition and the early stage of fully developed turbulent flows. This observation can be easily understood as the natural consequence of the suppressed turbulence discussed before. It is noted that, however, the heat transfer reduction observed in this work is not necessarily in conflict with the enhancement of turbulent heat transfer reported in the literature which was obtained at much higher Re in the fully developed turbulent region. Using the same argument, it can be expected that the size ratio  $d_p/\eta$  will surpass the critical value and the nanoparticles become “large” enough to intensify the turbulent heat transfer.

Figure 3. 9 provides an overview of the comparison of the average Nusselt number measured for nanofluids and the base fluid over the entire range of Re studied in the present work. It shows clearly that nanofluids enhance convective heat transfer modestly in laminar flow, however, they cause significant heat transfer deterioration in the transition and the early stage of fully developed turbulent regions. Both the enhancement and deterioration are seen to increase with the nanoparticle concentration. The delayed transition to turbulent heat transfer in nanofluids can also be identified in Figure 3. 9. Further, once the flow becomes fully turbulent, the difference in the measured Nusselt number between nanofluids and water tend to diminish as a result of the alleviated suppression of turbulence. Lastly, a piece of useful information may be deduced from Figure 3. 9 as a design guideline for utilizing nanofluids as an advanced

heat transfer fluid: nanofluids should be operated in either the laminar region or the fully developed turbulent region with sufficiently high Re for the sake of enhanced heat transfer performance.



**Figure 3. 8.** Average Nusselt number vs. Reynolds number in the transition and turbulent flow regions (heat flux  $q'' = 6.5 \text{ kW/m}^2$ ).



**Figure 3. 9.** Average Nusselt number versus Reynolds number over the entire flow range (nanofluids, heat flux  $q''=6.5 \text{ kW/m}^2$ )

### 3.3 SUMMARY

An experimental investigation was conducted to study the single-phase convective heat transfer of  $\text{Al}_2\text{O}_3$ -water nanofluids in a circular minichannel. Both the pressure drop and heat transfer coefficient were measured over a wide range of  $Re$ , covering the laminar, transition and early stage of fully developed turbulent flows. The key findings can be summarized as follows.

- 1) Nanofluids exhibit pronounced entrance region behaviors, both hydrodynamically and thermally, in the laminar region. The convective heat transfer of nanofluids is enhanced in the laminar flow with the penalty of increased pressure drop. The increments in both heat transfer and pressure drop are proportional to the nanoparticle volume concentration. No dramatic heat transfer enhancement as

reported in the early literature was observed in the nanoparticle concentration range considered in this work.

- 2) The critical  $Re$  at which the onset of transition to turbulence occurs is delayed in nanofluids, due to the particle-fluid interaction, which damps the instabilities in the flow. The suppression of turbulence is alleviated as the flow becomes fully developed turbulent. Correspondingly, the convective heat transfer of nanofluids deteriorates in the transition and the early stage of fully developed turbulent regions, and gradually recovers after the fully developed turbulence is intensified.
- 3) Established conventional correlations cannot fully predict the single-phase pressure drop and heat transfer of nanofluids, particularly in the transition and turbulent regions, even when the effective thermophysical properties are taken into consideration.
- 4) Nanofluids should be used in either the laminar flow or the fully developed turbulent flow with sufficiently high  $Re$  in order to yield enhanced heat transfer performance for engineering applications.

## **CHAPTER 4. SINGLE-PHASE THERMAL TRANSPORT OF $\text{Al}_2\text{O}_3$ - PAO NANOFLUIDS IN A MINICHANNEL**

This chapter presents an experimental study of single-phase forced convection of  $\text{Al}_2\text{O}_3$ -PAO nanofluids containing spherical and rod-like particles through a circular minichannel.

### **4.1 INTRODUCTION**

Wide discrepancies exist among the results from different research groups regarding how the dispersed nanoparticles alter the convective thermal transport of nanofluids. Moreover, the majority of the past studies were conducted for water-based nanofluids synthesized with spherical nanoparticles. Due to the simple spherical geometry of the particles, it is reasonable to neglect the effects of particle distribution and orientation on the effective thermophysical property and convective heat transfer of the nanofluids. However, when non-spherical nanoparticles, such as carbon nanotubes (CNTs) and titanate nanotubes (TNTs), are used to formulate the nanofluids, these effects can no longer be ignored because of the complex hydrodynamic interactions between the particle and the surrounding fluid medium. Also, the use of aqueous nanofluids is infeasible in many practical applications due to their limits in dielectric property and operating temperature range. Thus, there is a clear need to systematically study the convective thermal transport of non-aqueous nanofluids synthesized from non-spherical nanoparticles.

Several experimental studies were performed to study the effective thermophysical properties and convective heat transfer of nanofluids containing non-

spherical particles with high length-to-diameter ratio (aspect ratio). Cherkasova and Shan [98] studied the effects of particle aspect-ratio and dispersion state on the effective thermal conductivity of aqueous nanofluids with multi-walled nanotubes (MWNTs). They found the effective thermal conductivity decreases with reduced MWNT aspect ratio, and the conductivity enhancement was primarily due to the presence of individualized long nanotubes rather than the bundles of aggregated low aspect ratio nanotubes. The measured conductivity data showed a good agreement with the EMT predictions, and no anomalous increase was observed. Ding and his co-workers measured the rheological properties of ethylene-glycol (EG)-based nanofluids containing TNTs [99, 100]. Strong shear thinning behavior was found at high particle volume fractions in the EG-TNT nanofluids. The initial high viscosity was attributed to the resistance that arises when the Brownian rotation of the rod-like TNTs must be overcome for the nanotubes to align with the shear field, as well as the higher effective particle volume fraction caused by the particle aggregation than in a well-dispersed solution. Ding et al. [50] conducted convective heat transfer experiments of aqueous CNT nanofluids flowing through a circular tube. The authors found that the heat transfer enhancement was caused by the dynamic thermal conductivity of the nanofluids under shear conditions, which was much higher than the value measured at static conditions. They also suggested that the development of thermal boundary layer may be affected by shear thinning and the migration/aggregation of the long aspect ratio CNTs. Similar observations were made by Chen et al. [32] in their study of convective heat transfer of water-TNT nanofluids. Yang et al. [48] explored the effects of the Reynolds number, temperature, particle concentration on convective heat transfer of nanofluids through a

circular channel. Two kinds of nanofluids were formulated by dispersing disc-like graphite nanoparticles in a commercial automatic transmission fluid (ATF) and a mixture of synthetic base oils, respectively. The enhancement of heat transfer coefficient was much less than what was predicted by the Seider-Tate correlation with the effective thermal conductivity measured under static conditions. It was hypothesized that the shear-induced nanoparticle alignment disrupts the particle-particle interaction, which was assumed to be the main energy pathway in the nanofluids, and results in the deterioration of convective heat transfer.

Polyalphaolefins (PAO) are a group of synthetic engine oils that have been used extensively as lubricants and coolants in various military and aerospace applications [101]. As a heat transfer fluid, their thermal performance and energy efficiency are seriously limited by the low intrinsic thermal conductivity of PAO (0.132 W/mK vs. 0.6 W/mK for water). Therefore, it is of great practical interest to develop PAO-based nanofluids with enhanced thermophysical properties, which can also serve as a good sample for the fundamental study of convective thermal transport in non-aqueous nanofluids. Yang et al. [102] measured the thermal and rheological properties of PAO-CNT nanofluids at different dispersant concentrations, dispersing energy levels and nanoparticle concentrations. They found nanoparticle aggregation was the most important factor contributing to the effective properties: Larger agglomerates resulted in both higher thermal conductivity and higher viscosity. The thermal conductivity of nanofluids increased with the CNT aspect ratio until the CNTs were long enough to form a percolated network structure. Zhou et al. [33] investigated the dependence of viscosity on the shear-rate and the temperature in PAO-Al<sub>2</sub>O<sub>3</sub> nanofluids. At low particle volume

fraction (1v% and 3v% for nanospheres and 1v% for nanorods), the viscosity showed a weak dependence on shear rate and the nanofluids can be approximated as a Newtonian fluid. The relative viscosity (defined as  $\mu_r = \mu/\mu_f$ ) was found to be independent of temperature, indicating the rheological properties of nanofluids were primarily dominated by the base fluid. Shaikh et al. [103] measured the thermal conductivity of three types of PAO nanofluids containing CNTs, exfoliated graphite (EXG) and heat treated nanofibers (HTTs), respectively. They observed that the thermal conductivity enhancement was the most significant for PAO-CNT nanofluids, followed by EXG and HTT. Nelson and Banerjee [101] conducted convective heat transfer experiments of PAO nanofluids in a plain offset fin heat exchanger. The nanofluids were synthesized with exfoliated graphite fibers. They showed the augmented Nusselt number was due to the precipitation of nanoparticles on the wall of the heat exchanger which acted as nanoscale fins to enhance the convective heat transfer.

The literature survey reveals that thermal transport of non-aqueous nanofluids containing non-spherical particles has not been well understood. Particularly, there is a clear call for a systematic investigation on the effects of the particle-fluid and particle-particle interactions on the effective thermophysical property and convective heat transfer characteristics of the nanofluids.

## **4.2 EXPERIMENTS**

The experimental apparatus, test procedures and data analysis are similar to that used for the study of single-phase convection of  $\text{Al}_2\text{O}_3$ -water nanofluids, and have been discussed in Chapter 2. In this section, only the experimental results are presented.

#### 4. 2.1 EXPERIMENTAL RESULTS FOR PAO

Control experiments were first performed with the base fluid (PAO) to obtain baseline information for single-phase transport of nanofluids. For laminar flow, the Hagen-Poiseuille equation [80] can be used to predict the friction factor for hydrodynamically fully developed condition

$$f \cdot \text{Re} = 64, \quad (4.1)$$

and the Shah equation [83] is used to account for the developing length effect

$$f_{app} \text{Re} \approx 4 \left( \frac{3.44}{\sqrt{\zeta}} + \frac{16 + 0.3125\zeta - 3.44/\sqrt{\zeta}}{1 + 2.12 \times 10^{-4} / \zeta^2} \right). \quad (4.2)$$

where  $\zeta = (x/D)/\text{Re}$ . Figure 4. 1 depicts the measured friction factor of PAO as a variation of the Reynolds number. The experiments in this work were conducted over the same flow rate range (50 ~ 200 mLPM) as for water in the previous work [104], however, a much lower maximum Re ( $\text{Re} \leq 460$ ) was achieved due to the high viscosity of PAO.

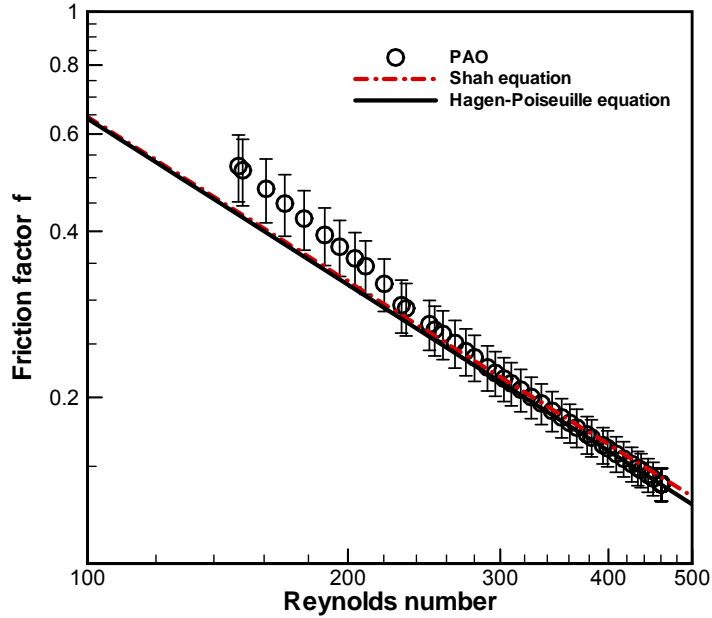


**Figure 4. 1.** Friction factor of PAO versus Reynolds number.

Consequently, the hydrodynamic entrance length ( $L^+ \approx 0.056 Re \cdot D$ ) is less than 9.2% of the total channel length even at the highest Reynolds number. Thus, the entrance region effect is insignificant in all the experiments conducted. Figure 4.1 shows the experimental data agree quite well with the predictions from Eqs. (4.1) and (4.2), except for the low  $Re$  region where the measurement uncertainty is relatively high.

The local Nusselt number results of PAO are shown in Figure 4.2 as a function of  $x^*$  ( $= x/(D Re Pr)$ ). Due to the large Prandtl number of PAO ( $61.6 < Pr < 87.1$ ), the thermally developing flow behavior can be clearly identified:  $Nu_x$  approaches infinity at  $x^* = 0$  and rapidly decays as  $x^*$  decreases, and  $Nu_x$  does not reach the asymptotical (fully developed) value, i.e.,  $Nu = 4.36$ , over the range of  $x^*$  studied in this work. The experimental data can be reasonably correlated by the Shah-London equation [105].

$$Nu_x = \begin{cases} 1.302 / (x^*)^{1/3} - 1 & \text{for } x^* \leq 0.00005 \\ 1.302 / (x^*)^{1/3} - 0.5 & \text{for } 0.0005 \leq x^* \leq 0.0015 \\ 4.364 + 8.68(1000x^*)^{-0.506} e^{-41x^*} & \text{for } x^* \geq 0.0015 \end{cases} \quad (4.2)$$

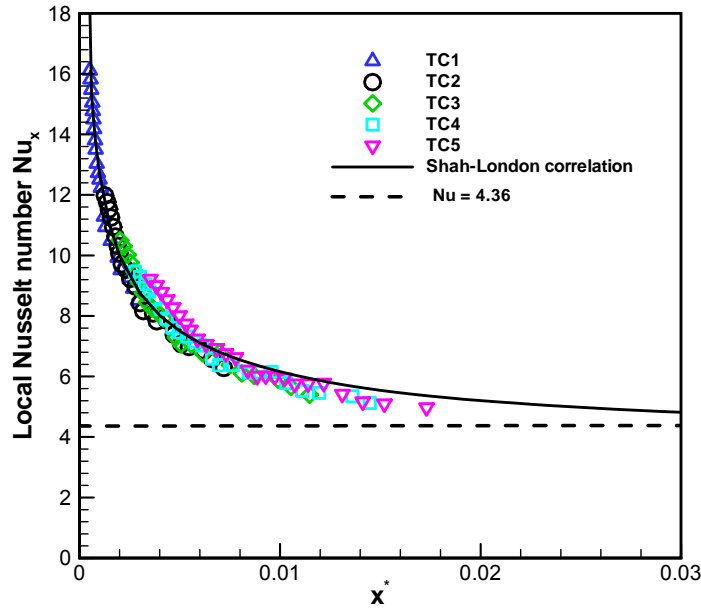


**Figure 4.2.** Local Nusselt number for PAO versus  $x^*$  (heat flux  $q'' = 6.5 \text{ kW/m}^2$ ).

#### 4. 2.2 EXPERIMENTAL RESULTS FOR AL<sub>2</sub>O<sub>3</sub>-PAO NANOFLUIDS

The pressure drop experiments were conducted for NF1 and NF2 with volume concentrations of 0.65 and 1.3 %, respectively. Pressure drop across the length of the minichannel is first presented in Figure 4. 3 as a function of the flow rate. It shows nanofluids (both NF1 and NF2) incur higher pressure drop than the base fluid at the same flow rate, and the difference enlarges with increasing particle volume fraction. Consistent with the viscosity measurements, the pressure drop of NF2 is always greater than that of NF1 at the same volume fraction.

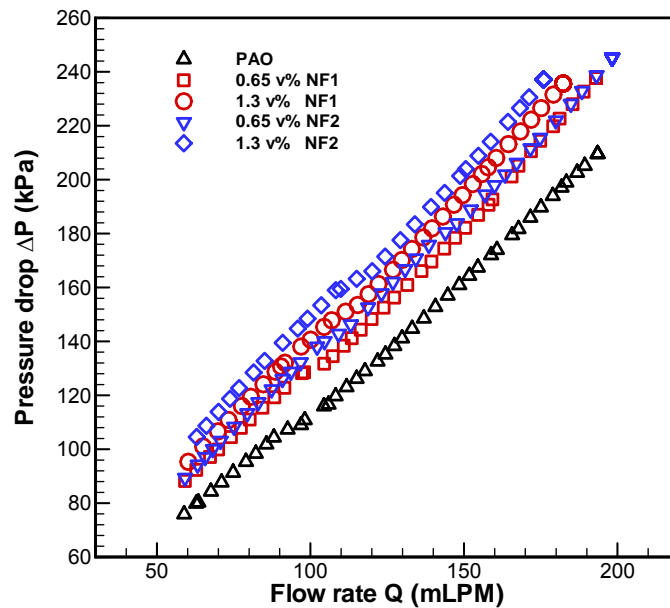


**Figure 4. 3.** Pressure drop across the minichannel versus flow rate.

Figure 4. 4 shows the measured friction factor of the nanofluids as a variation of the Reynolds number. At medium to high Reynolds numbers, the  $f$ -measurements of NF1 match the Shah prediction fairly well. In comparison, the data for NF2 show appreciable deviation in the same range of Re, i.e., dropping below the theoretical curve.

This may be attributed to the stronger alignment of the nanorods under shear stresses at higher  $Re$ , causing the effective viscosity to decrease in a process similar to the shear thinning in non-Newtonian fluids.

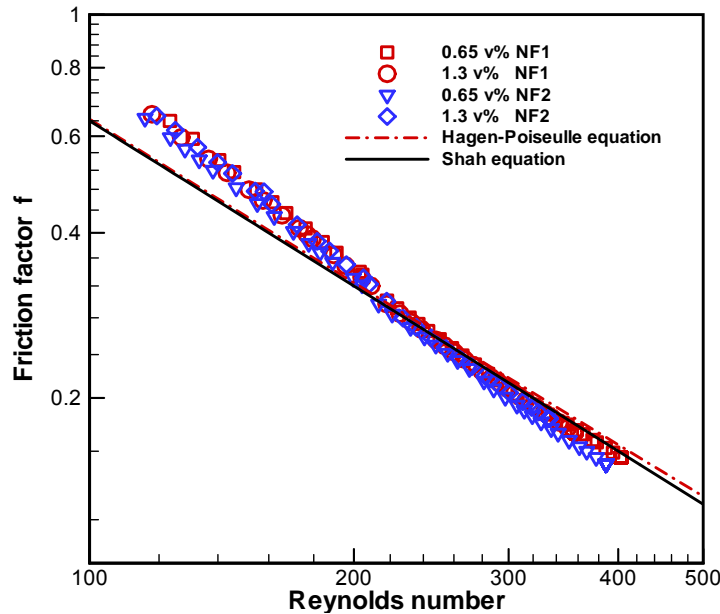
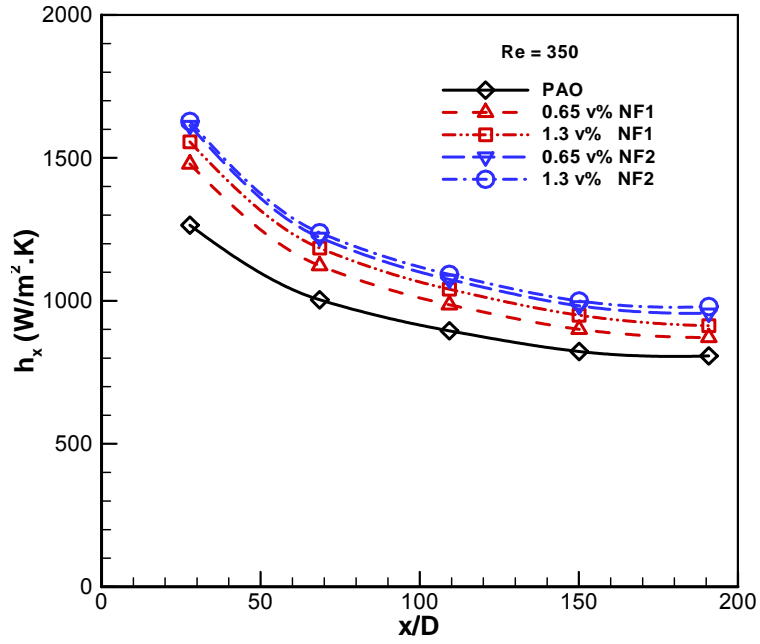


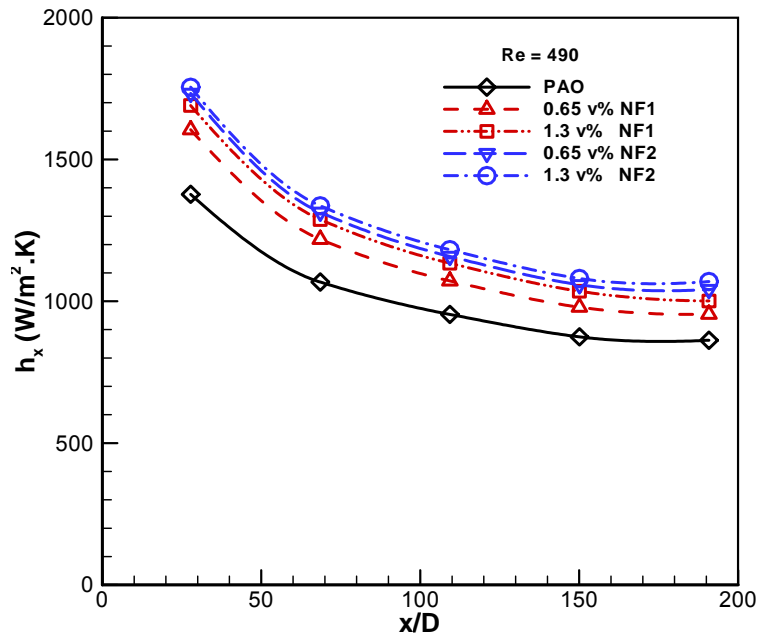
**Figure 4. 4.** Friction factor of nanofluids as a function of Reynolds number  
(Error bars are not shown for clarity)

Convective heat transfer experiments were conducted for NF1 and NF2 with the volume concentrations of 0.65 and 1.3 %, respectively. The local heat transfer coefficients measured at five axial locations (TC1 through TC5) are presented in Figure 4. 5 for  $Re = 350$  and  $490$ . It can be found that the convective heat transfer of nanofluids is enhanced as compared to the base fluid, and the increment increases proportionally to the Reynolds number and the particle volume fraction. The heat transfer enhancement is more significant in the regions near the channel entrance than at the downstream locations. For instance, in Figure 4. 5(a), the enhancement in heat transfer coefficient for

the 1.3% NF2 nanofluid is 28.7% near the entrance and decreases to less than 21% near the channel exit. This trend strengthens with increasing nanoparticle concentration and Reynolds number.



(a)



(b)

**Figure 4. 5.** Local convective heat transfer of PAO (heat flux  $q'' = 6.5 \text{ kW/m}^2$ ).

More interestingly, it is observed that the heat transfer coefficient for 0.65 v% NF2 is higher than those for NF1 at both concentrations of 0.65 v% and 1.3 v%. This is unexpected because the thermal conductivity data in Figure 2. 8 and Figure 2. 9 suggest

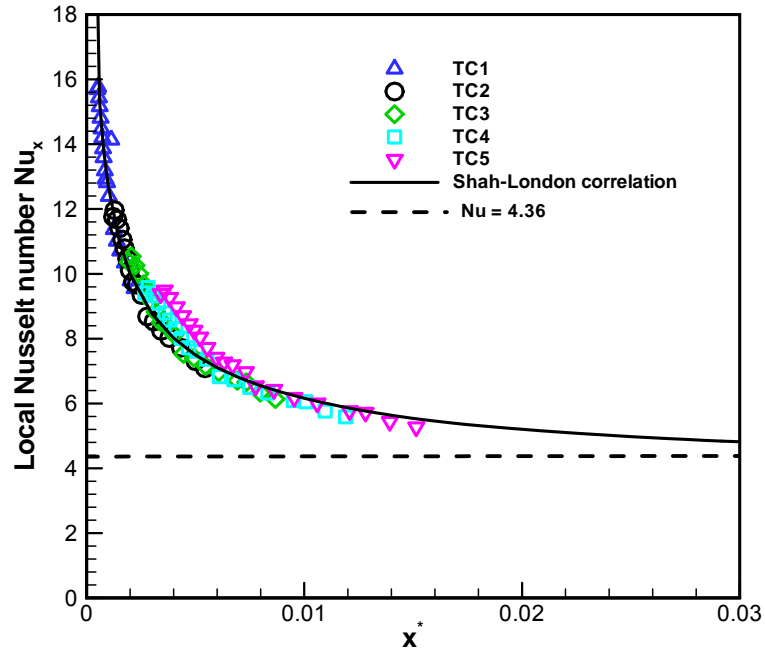
that  $k$  for 0.65 v% NF2 ( $k/k_f = 1.076$ ) is only slightly higher than that for 0.65 v% NF1 ( $k/k_f = 1.053$ ), but lower than that for 1.3 v% NF1 ( $k/k_f = 1.098$ ). When the effect of shear-induced particle alignment is considered, an even larger discrepancy emerges. Since the series structure can be more easily formed in nanofluids containing rod-like particles (as shown in Figure 2. 11), which represents the least effective pathway for thermal energy transport, the convective heat transfer of NF2 would be lower than that of NF1 at the same particle volume concentration. However, this conjecture is in direct contradiction to the results shown in Figure 4. 5.

The paradox may be explained qualitatively by examining the periodic orientational motions of rod-like particles in a shear flow [106-109]. A rod-like particle tends to align its long axis with the flow direction. Unless perfectly aligned, the shear velocities will be slightly different at the two ends of the rod, causing the rod to rotate periodically about its center to trace out the so-called Jeffery orbits [110]. In colloidal suspensions of sufficiently high concentration, the particles interact with their neighbors and are forced to perform the orientational motion collectively, which can be described by the “director”, i.e., the average orientation of the rods. At low shear rates, the director performs a “tumbling” or “kayaking” motion in which the director rotates slowly when it is nearly aligned with the flow direction, and rotates rapidly when its long axis makes a non-zero angle with the shear plane. At intermediate shear rates, the director will oscillate up and down in the shear plane in a symmetrical way about the flow direction, transitioning into the “wagging” motion. At further increased shear rate, the wagging motion is suppressed until the director is arrested making a stationary orientation at a small angle with respect to the flow direction. Clearly, the periodic orientational motions

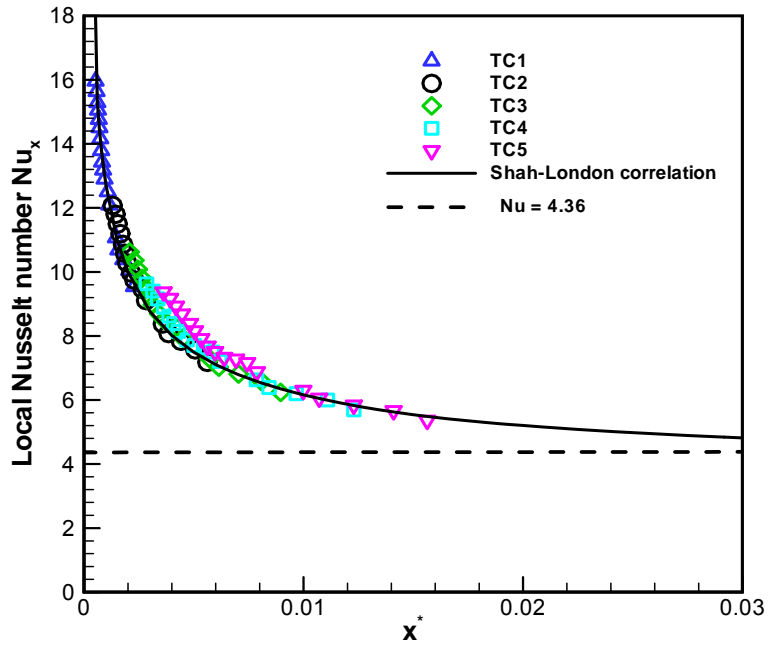
of the rod-like particles, either tumbling, kayaking or wagging, will create disturbances to the local flow field, acting in the role of turbulent eddies, to promote the convective heat transfer. Thus, the fluid-particle interactions are a two-way coupling process: while the shear field re-distributes the particles, the orientational motion of the particles also modulates the development of both the hydrodynamic and thermal boundary layers. Furthermore, as the nanorods rotate in the thermal boundary layer, their two ends experience higher temperature in the near-wall region and lower temperature in the near-bulk region periodically. Since heat can be easily conducted from the hot end to the cold end of the highly conductive nanorods, they may act as heat pumps to effectively transfer heat into the bulk of the fluid. Indeed, the results in Figure 4. 5 suggest that the heat transfer enhancement due to the periodic orientational motion of the nanorods in NF2 not only offsets the adverse effect of reduced effective thermal conductivity due to the shear-induced particle alignment, but it also surpasses the heat transfer augmentation in NF1 due to higher particle loading.

Finally, the local Nusselt number measurements are plotted in Figure 4.6 and Figure 4. 7 as a function of  $x^*$  for NF1 and NF2, respectively. Figure 4. 6 shows that at both volume fractions of 0.65 and 1.3 v%, the experimental data of NF1 match closely the predictions from Shah-London's correlation. In Figure 4. 7,  $Nu_x$  for NF2 initially follows the Shah-London prediction. As  $x^*$  increases,  $Nu_x$  drops quickly with a slope much steeper than the theoretical curve. Unlike PAO and NF1, the  $Nu_x$  results for NF2 at different axial locations are fairly dispersive and no common trend line can be found. These behaviors may be attributed to the effect of shear-induced motions of rod-like particles on the effective thermal conductivity and the heat transfer enhancement. In

calculating  $Nu_x (= h_x \cdot D/k)$ , the convective heat transfer coefficient,  $h_x$ , is estimated using Eq. (3.5), but the effective thermal conductivity,  $k$ , is from measurements obtained under static conditions (as in Figure 2. 8). As previously described, the shear-induced alignment and orientational motion of the nanorods cause the *actual* effective thermal conductivity of NF2 to be dependent on the local shear field in a rather complex manner. Therefore, the use of static measurement of  $k$  leads to the artifacts shown in Figure 4. 7. Consequently, certain cautions should be exercised when the convective heat transfer performance is evaluated on the basis of conventional dimensionless numbers, such as  $Nu$ , for nanofluids containing non-spherical particles.

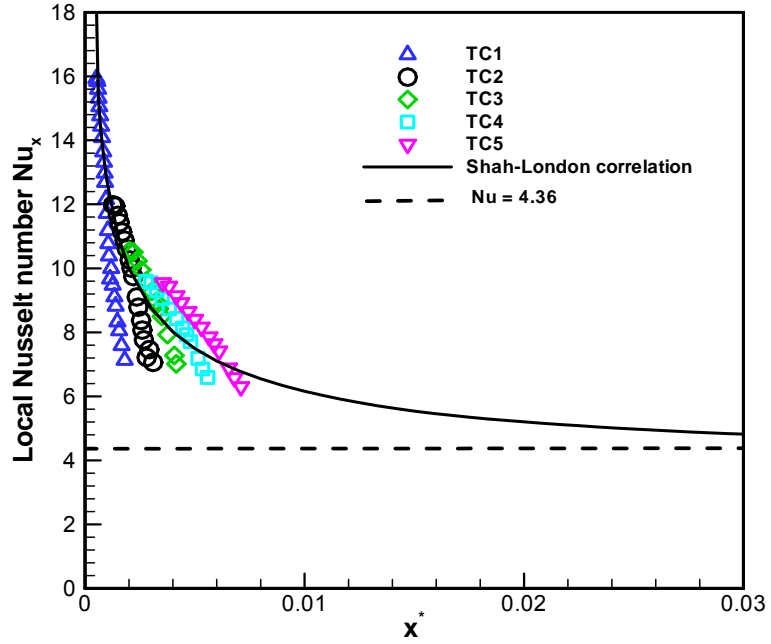


(a)

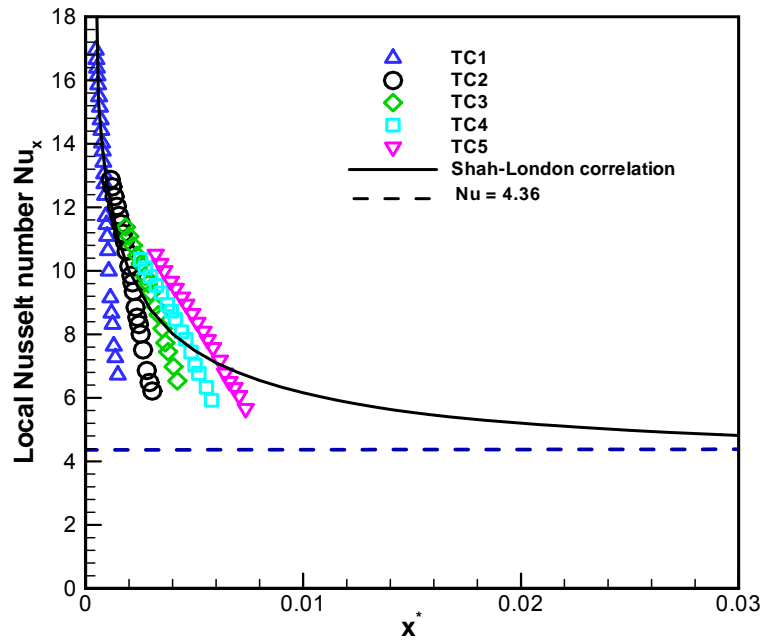


(b)

**Figure 4. 6.** Local Nusselt number for NF1 as a function of  $x^*$  (heat flux  $q'' = 6.5 \text{ kW/m}^2$ ) for: (a) 0.65 v%, and (b) 1.3 v%.



(a)



(b)

**Figure 4. 7.** Local Nusselt number for NF2 as a function of  $x^*$  (heat flux  $q'' = 6.5 \text{ kW/m}^2$ ) for: (a) 0.65 v%, and (b) 1.3 v%.

### 4.3 SUMMARY

An experimental study was conducted to investigate the thermophysical properties and convective heat transfer characteristics of  $\text{Al}_2\text{O}_3$ -PAO nanofluids containing both spherical and rod-like nanoparticles. The effective viscosity and thermal conductivity of the nanofluids were measured, and the results were compared with predictions from several existing theories in the literature. It was found that, in addition to the particle volume fraction, other parameters including the aspect ratio, dispersion state and aggregation of nanoparticles as well as the shear field have a significant impact on the effective properties, especially for nanofluids containing non-spherical particles. The pressure drop and convection heat transfer coefficient were also measured for the nanofluids in the laminar flow regime. Although established theoretical correlations provide satisfactory prediction of the friction factor and Nusselt number for nanofluids containing spherical nanoparticles, they fail for nanofluids containing rod-like nanoparticles. The results indicate that in a convective flow, the shear-induced alignment and orientational motion of the particles must be considered in order to correctly interpret the experimental data of nanofluids containing non-spherical nanoparticles. Findings from this study imply that, if external means (such as electromagnetic force or shear field) are applied to manipulate the states of dispersion and orientation of the nanoparticles in the base medium, thermal transport of the nanofluids can be strategically controlled to yield optimal performance.

## **CHAPTER 5. THERMAL EFFECTIVENESS OF LAMINAR FORCED CONVECTION OF NANOFLUIDS**

The results in the previous chapters show that the convective thermal performance of nanofluids in cooling applications depends crucially on the effective thermophysical properties. Based on the experimental data, the thermal effectivenesses of the nanofluids are evaluated critically in this chapter using various figures of merit (FOM) under three typical flow constraints, i.e., constant flow rate, constant Reynolds number and constant pumping power.

### **5.1 INTRODUCTION**

Past studies have confirmed that single-phase forced convective heat transfer can be enhanced by nanofluids [2, 4, 6, 111-113]. However, the adoption of nanofluids for real-world cooling applications cannot be established solely from a heat transfer perspective [114, 115]. Other concurrent aspects, such as the hydrodynamic performance, must also be considered in order to determine the overall thermal performance of nanofluids.

The convective thermal performance of nanofluids depends crucially on the effective thermophysical properties. For nanofluids, the thermal conductivity is enhanced favorably for better heat transfer, but the increase in viscosity necessitates a higher pumping power to sustain sufficient flow in the cooling device/system [38, 116-118]. Prasher et al. [119] showed that the increase in nanofluid viscosity should be less than four times the increase in thermal conductivity to yield the same convective heat transfer coefficient as the base fluid with a comparable pressure drop; otherwise, the nanofluid

will underperform. Another drawback with nanofluids is related to the lower specific heat with respect to that of the base fluid. For convective liquid cooling, the thermal conductivity determines the coolant's heat transfer capability from the heating source, and the specific heat determines the ability of the fluid to store and move heat away from the cooling device [120]. Thus, the use of nanofluids will simultaneously reduce the temperature difference between the heating wall and the fluid (due to higher thermal conductivity) and increase the local mean temperature of the fluid (due to lower specific heat) in forced convection through a channel under constant heat flux boundary conditions. Additionally, Bergman [121] demonstrated that the thermal performance of nanofluids is a function of the channel length and the mass flow rate, and that a particular nanofluid, although efficient for one application, can be a poor choice for a different one. The exergetic analysis done by Singh et al. [122] showed that for nanofluids in forced convection heat transfer, the thermodynamic effectiveness is strongly affected by the channel size, and it is beneficial to use nanofluids in conventional channels with laminar flow and in microchannels with turbulent flow.

In view of so many influencing factors, a systematic evaluation of the thermal performance of nanofluids is complex, which is further complicated by the lack of well-established evaluation criteria. In the past studies, the thermal performance of nanofluids has been defined loosely and evaluated using a myriad of different criteria (as will be elaborated later), making it difficult to compare the results from different researchers. One exception is the work by Yu et al. [7] that addresses the validity of thermal performance evaluation criteria used for nanofluids. The authors compared the convective heat transfer coefficient of nanofluids to that of the base fluid in turbulent

flow under three flow constraints: constant flow velocity, constant Reynolds number and constant pumping power. They found that the constant pumping power comparison offers the most consistent assessment, the constant flow velocity comparison is quite accurate when the pumping power is negligible as compared to the total power consumption, but the constant Reynolds number comparison should not be used because it completely ignores the pumping power penalty caused by pumping the nanofluid to reach the same Reynolds number as the base fluid. Other studies pertinent to the evaluation of thermal performance of nanofluids are scarce and are mostly limited to theoretical and/or numerical analysis. As a consequence, despite of extensive studies on the thermal property and convective heat transfer of nanofluids, their suitability as a candidate coolant for liquid cooling applications remains ambiguous and even controversial.

The literature survey reveals that thermal performance of nanofluids has not been well understood. This chapter aims at providing a comprehensive assessment of the thermal performance of nanofluids to engineering practitioners in selecting suitable coolants for liquid cooling applications.

## **5.2 SELECTION CRITERIA OF COOLANTS**

The convective heat transfer and hydrodynamic performances of a coolant depend critically on its thermophysical properties [123]. For instance, the thermal conductivity defines the coolant's capability to transfer heat from a heat source into the coolant; the specific heat represents the coolant's ability to store thermal energy and to carry heat away per unit mass, and the viscosity is related to the flow resistance and determines the system pressure drop and the required pumping power to enable cooling. Usually, a good

coolant would possess high values of thermal conductivity and specific heat as well as a low viscosity.

Various forms of figure of merit (FOM) have been introduced in the literature to evaluate the thermal performance of a candidate coolant. The first one was the Mouromtseff number ( $Mo$ ) [124]

$$Mo = \frac{\rho^a k^b c_p^d}{\mu^e}, \quad (5.1)$$

where the exponents  $a$ ,  $b$ ,  $d$  and  $e$  can be found from appropriate heat transfer correlations [115]. For a fully developed laminar flow,  $Mo$  is simply the thermal conductivity of the fluid. Since  $Mo$  is a dimensional parameter, it's difficult to use in assessing the thermal performance of synthetic coolants, such as nanofluids, relative to the base fluids. A more convenient FOM is the ratio of convective heat transfer coefficient of the coolant over that of the base fluid [7, 125]

$$(FOM)_h = h / h_b, \quad (5.2)$$

where the heat transfer coefficient  $h$  is related to the Nusselt number  $Nu$  by Eq. (3.9). For a fully-developed laminar flow under constant wall heat flux conditions [81],  $Nu = 48/11$ , it follows

$$(FOM)_h = k / k_b, \quad (5.3)$$

For a turbulent flow, the Dittus-Boelter equation can be used to estimate  $h$ ,  $h = 0.023 Re^{0.8} Pr^{0.4} (k / D)$ , which leads to

$$(FOM)_h = (\rho / \rho_b)^{0.8} (c_p / c_{p,b})^{0.4} (\mu / \mu_b)^{-0.4} (k / k_b)^{0.6} (u / u_b)^{0.8}. \quad (5.4)$$

It is noted that Eq. (5.4) may be recast in different forms specific to the flow constraint imposed on the cooling system. For example, if  $Re$  remains constant, i.e.,  $\rho u / \mu = \rho_b u_b / \mu_b$ , the FOM is

$$(FOM)_h = (c_p / c_{p,b})^{0.4} (\mu / \mu_b)^{0.4} (k / k_b)^{0.6} . \quad (5.5)$$

Similar expressions of  $(FOM)_h$  can be obtained for constant flow velocity ( $u = u_b$ ) and constant pumping power ( $\rho^{0.75} u^{2.75} \mu^{0.25} = \rho_b^{0.75} u_b^{2.75} \mu_b^{0.25}$ ) conditions, respectively [7].

An alternative FOM, which is also based on the heat transfer performance, is defined as the ratio of the maximum overall temperature difference (i.e., the difference between the wall temperature at the channel exit and the fluid temperature at the channel inlet) of the nanofluid to that of the base fluid [121, 126, 127]

$$(FOM)_T = 1 - \frac{(T_{w,o} - T_{in})}{(T_{w,o} - T_{in})_b} . \quad (5.6)$$

For laminar flow through a circular channel with constant heat flux conditions, it is shown that [121]

$$(FOM)_T = 1 - \frac{\left[ \left( \frac{1}{h(\pi DL)} \right) + \left( \frac{1}{\dot{m}c_p} \right) \right]}{\left[ \left( \frac{1}{h(\pi DL)} \right) + \left( \frac{1}{\dot{m}c_p} \right) \right]_b} . \quad (5.7)$$

In practical cooling applications, while the primary goal is to enhance heat transfer, it becomes more and more important to minimize the pumping power consumption required to enable the cooling performance. This is necessitated by the ever-increasing energy prices as well as the limits of battery technologies in portable electronics that demand the cooling solutions to be as power-efficient as possible [114]. Therefore, it is proposed that the FOM be defined as [123]:

$$(FOM)_p = \left[ (c_p h / P) \right] / \left[ (c_p h / P)_b \right], \quad (5.8)$$

where the pumping power  $P$  is  $P = \Delta p \cdot Q$  for an incompressible fluid, and the pressure drop can be obtained from Eq. (3.2):  $\Delta p = f(L/D)(\rho u^2 / 2)$ . For a fully-developed laminar flow under constant wall heat flux conditions,  $f = 64 / Re$  and  $Nu = 48/11$ , Eq. (5.8) can be re-arranged to yield

$$(FOM)_p = (\mu / \mu_b)^{-1} (k / k_b) (c_p / c_{p,b}) (u / u_b)^{-2}. \quad (5.9)$$

For a turbulent flow,  $f = 0.316 / Re^{0.25}$  and  $h = 0.023 Re^{0.8} Pr^{0.4} (k / D)$ ,  $(FOM)_p$  becomes

$$(FOM)_p = (\rho / \rho_b)^{0.05} (\mu / \mu_b)^{-0.65} (k / k_b)^{0.6} (c_p / c_{p,b})^{1.4} (u / u_b)^{-1.95}. \quad (5.10)$$

Similarly, Eqs. (5.9) and (5.10) can be manipulated for prescribed flow conditions (such as constant  $Re$ , constant  $Q$ , or constant  $P$ ) to arrive at specific  $(FOM)_p$  expressions. Other forms of FOM have also been used to account for the offsetting effects of the increased pumping power consumption against the heat transfer enhancement brought forth by the coolant [119, 128]. For instance, Garg et al. [128] compared the thermal effectiveness of the nanofluids by using

$$(FOM)_Q = (q / P) / (q / P)_b, \quad (5.11)$$

where  $q$  is the heat transfer rate.

To justify the adoption of a nanofluid in the place of the base fluid for cooling applications, the following criteria should be met:  $(FOM)_h > 1$ ,  $(FOM)_T > 0$ ,  $(FOM)_p > 1$ ,  $(FOM)_Q > 1$ .

### 5.3 THERMAL PERFORMANCE OF NANOFLUIDS

Convective thermal performance of nanofluids can be evaluated using various FOM criteria previously developed. However, it must be pointed out that even with the same FOM criterion, different conclusions may be reached on the suitability of using a nanofluid for a cooling application, depending on the way the experimental data are presented and interpreted. In the literature, three flow constraints are commonly used as bases in comparing the heat transfer performance of nanofluid with the base fluid: constant  $Re$ , constant  $Q$ , and constant  $P$  [125, 129, 130]. These three flow constraints are closely interrelated, but can lead to different thermal performance. In the constant  $Re$  comparison, for instance, the flow rate ratio of the nanofluid over the base fluid is

$$(Q/Q_b)_{Re} = (\rho/\rho_b)^{-1} (\mu/\mu_b), \quad (5.12)$$

while in the constant  $P$  comparison, the flow rate ratio for fully-developed laminar flow is

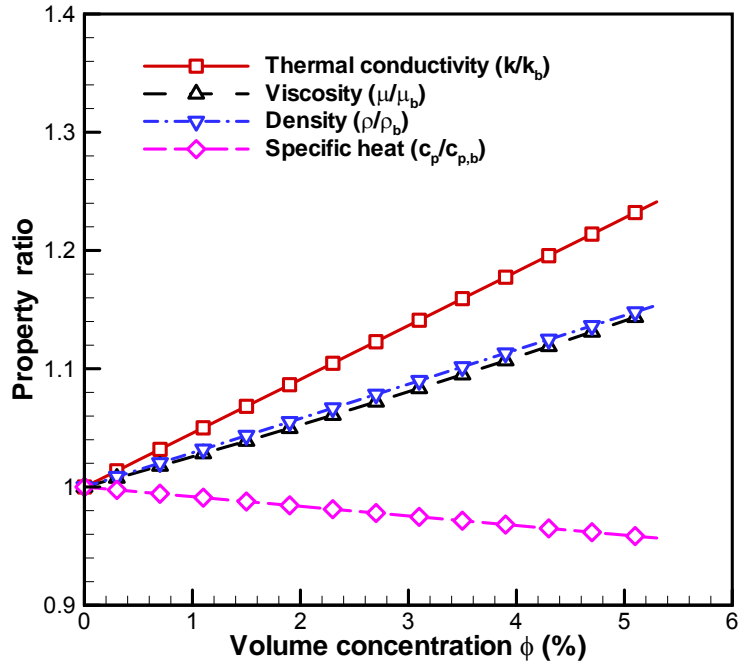
$$(Q/Q_b)_P = (\mu/\mu_b)^{-1/2}, \quad (5.13)$$

From Figure 5.1 (a), the viscosity ratio  $\mu/\mu_b$  for  $Al_2O_3$ -water nanofluids follows essentially the same trend line of the density ratio  $\rho/\rho_b$  i.e.,  $(\mu/\mu_b) \sim (\rho/\rho_b)$ . Hence, according to Eq.(5.12),  $(Q/Q_b)_{Re}$  remains approximately unity, in other words, the constant  $Re$  basis is equivalent to the constant  $Q$  basis for  $Al_2O_3$ -water nanofluids. For  $Al_2O_3$ -PAO nanofluids, however, Figure 5.1 (b) shows that  $\mu/\mu_b$  always exceeds  $\rho/\rho_b$  and as a result,  $(Q/Q_b)_{Re} > 1$ . Further, it can be deduced from Eq. (5.13) that  $(Q/Q_b)_P < 1$  for both nanofluids due to the increased effective viscosity. Thus, the actual velocity ratio of the nanofluid to the base fluid can be very dissimilar under different flow

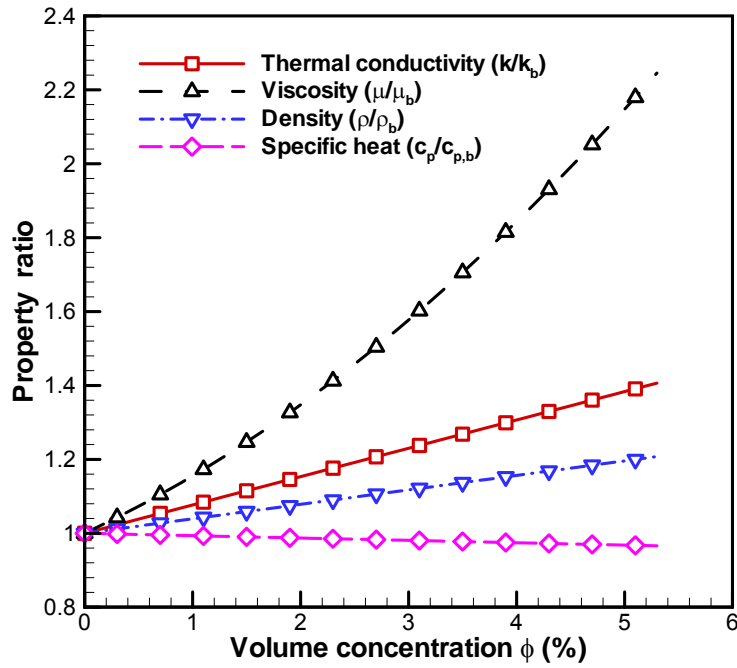
constraints. Since the convective heat transfer of the nanofluids is clearly governed by thermally developing flow (as shown in Figure 4.6), it is not surprising that different (or even contradictory) conclusions may be drawn on thermal performance of the same nanofluid if they were not made under the same flow condition [7, 125, 131]. In the present work, the thermal performance of each nanofluid is evaluated using all three bases, (i.e., constant  $Q$ , constant  $Re$  and constant  $P$ ), to ensure a fair and comprehensive comparison against the base fluid.

Figure 5.2 illustrates the  $(FOM)_h$  evaluation for  $Al_2O_3$ -water nanofluids. It is noted that the data are presented in terms of the comparison of convective heat transfer coefficients, rather than the explicit values of  $(FOM)_h$ . This is because, by definition, an FOM is a normalized parameter with regard to that of the base fluid. As a quotient, the dividend and the divisor of the FOM must correspond to identical flow conditions, e.g., when  $(FOM)_h$  is evaluated on the constant  $Q$  basis,  $h$  and  $h_b$  must be measured at the same flow rate, whereas  $h$  and  $h_b$  must be for the same  $Re$  (or  $P$ ) if constant  $Re$  (or  $P$ ) is used as the basis. Thus, to obtain explicit values of FOM will render the experimentation process very cumbersome. In contrast, direct comparison of the constituent thermal performance parameters provides a more convenient measure of FOM. For instance, since the trend line of  $h$  exceeds that of  $h_b$ , it simply implies  $(FOM)_h > 1$ . Figure 5.2 shows that nanofluids outperform the base fluid under all three flow constraints. For example, it is deduced from Figure 5.2 (a) that  $(FOM)_h$  for the 5 v% nanofluid varies in 1.13 - 1.18 over the range of flow rate measured. As discussed earlier,  $(Q/Q_b)_{Re} \sim 1$  for  $Al_2O_3$ -water nanofluids, i.e., the flow rates of nanofluids are approximately equal to that of the base fluid at the same  $Re$ . Due to this  $Q$ - $Re$  correspondence, the  $Q$ -based and  $Re$ -

based plots are almost indistinguishable in Figures 5.2 (a) and (b). Therefore, only the  $Q$ -based results will be reported for  $\text{Al}_2\text{O}_3$ -water nanofluids in the subsequent discussion. When  $P$  is used as the basis, Figure 5.2 (c) shows the data points are clustered together, especially at lower range of  $P$ , which indicates  $(FOM)_h$  of nanofluids diminishes when pumping power consumption is taken into consideration.

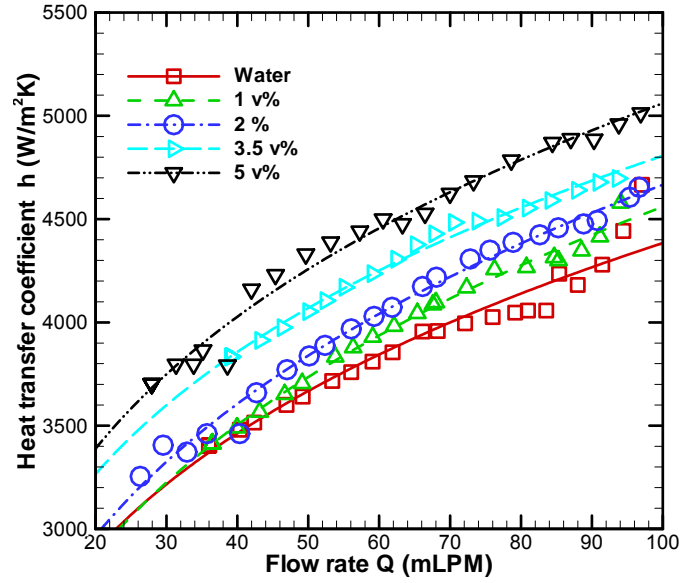


(a)

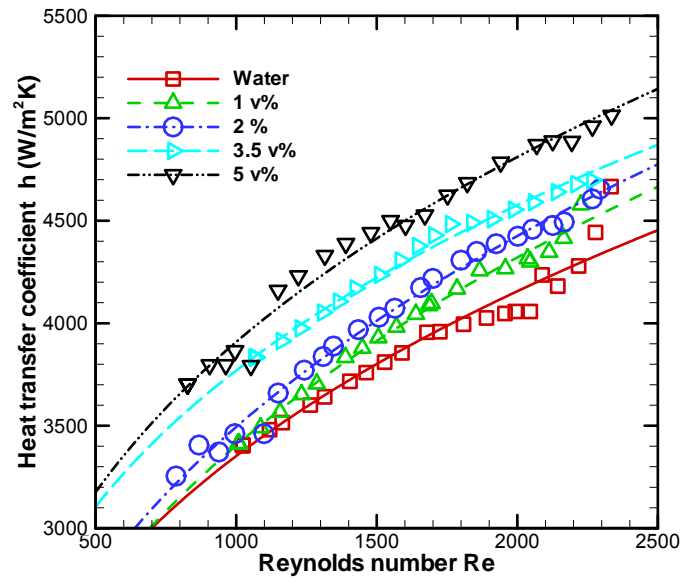


(b)

**Figure 5. 1.** Effective thermophysical properties of nanofluids (shown as the ratio to those of the base fluids): (a) Al<sub>2</sub>O<sub>3</sub>-water nanofluids, and (b) Al<sub>2</sub>O<sub>3</sub>-PAO nanofluids.

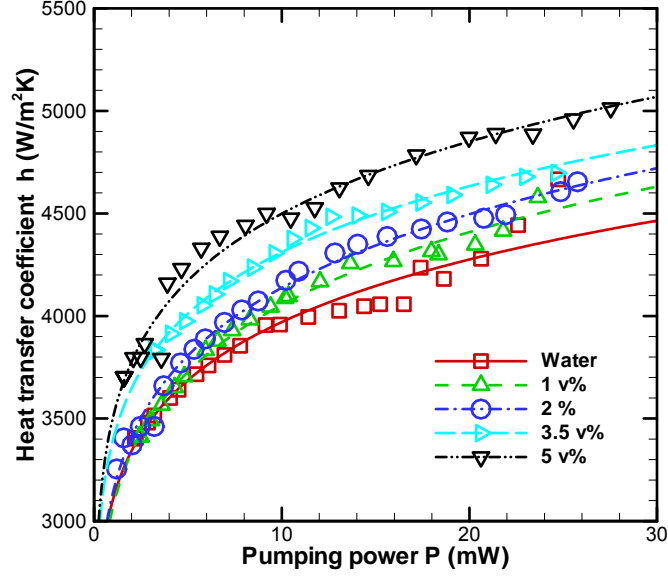


(a)



(b)

**Figure 5. 2.** Evaluation of  $(FOM)_h$  of Al<sub>2</sub>O<sub>3</sub>-water nanofluids presented in terms of convective heat transfer coefficient using different bases of comparison: (a)  $Q$ -based; (b)  $Re$ -based and (c)  $P$ -based (heat flux  $q'' = 6.5 \text{ kW/m}^2$ ).

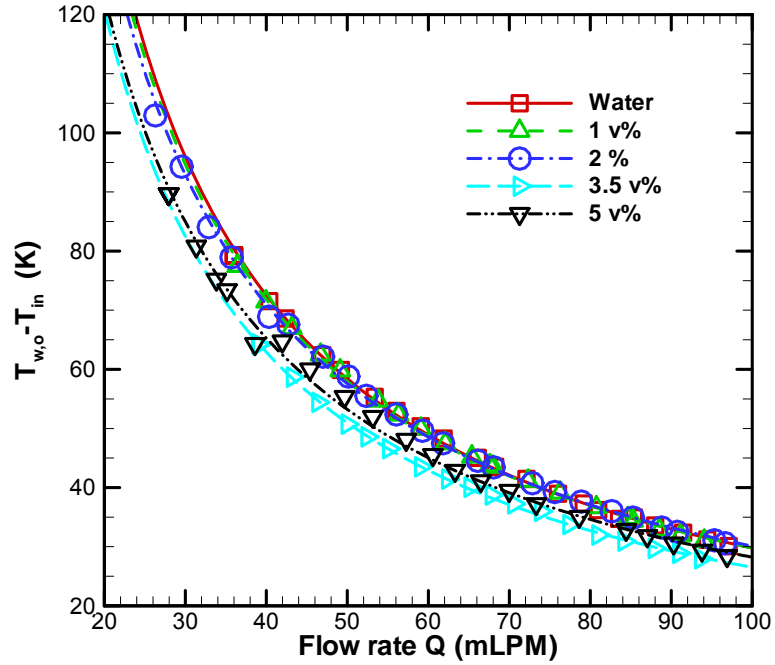


(c)

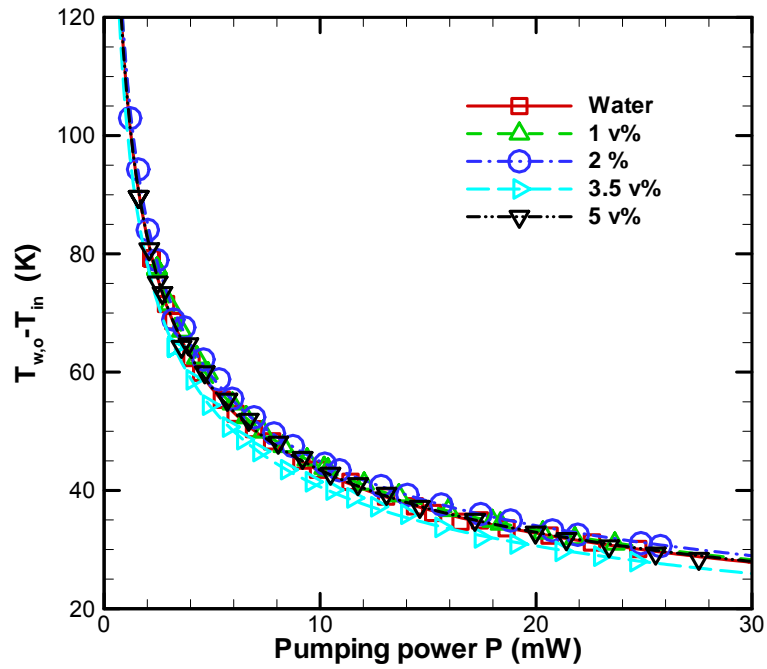
**Figure 5.2.** Evaluation of  $(FOM)_h$  of  $Al_2O_3$ -water nanofluids presented in terms of convective heat transfer coefficient using different bases of comparison: (a)  $Q$ -based; (b)  $Re$ -based and (c)  $P$ -based (heat flux  $q'' = 6.5 \text{ kW/m}^2$ ) [continued].

Figure 5. 3 compares the measured  $T_{w,o} - T_{in}$  as an assessment of  $(FOM)_T$  for  $Al_2O_3$ -water nanofluids. Clearly, the lower the values of  $T_{w,o} - T_{in}$ , the more effective is the fluid in removing heat from the system [132]. It is seen in Figure 5. 3 (a) that the nanofluids do improve the heat transfer performance over the base fluid, however, the enhancement is not as significant as measured by  $(FOM)_h$  in Figure 5. 2 (a). The reason can be explained as follows. Since the thermal resistance of a convective cooling device is defined as  $R = (T_{w,o} - T_{in}) / q$ ,  $(FOM)_T$  is closely related to the ratio of the thermal resistance of nanofluid to that of the base fluid. The overall thermal resistance consists of a convective component, which is represented by  $1 / [h(\pi DL)]$  in Eq. (5.7) and signifies the fluid's ability to transfer thermal energy from the source (depending on  $k$  and  $h$ ), and a

caloric component, which is represented by  $1/(\dot{m}c_p)$  and denotes the fluid's ability to transport the energy out of the system (depending on  $\rho c_p$ ). With nanofluids, the convective resistance is reduced as a result of the enhanced convective heat transfer coefficient, however, the caloric resistance is increased due to the lower specific heat of the nanofluids. Consequently, the compromise leads to a lesser degree of enhancement than the case where the adverse effect of lower specific heat is neglected (as in Figure 5. 2(a)). Additionally, for the same reason, Figure 5. 3(a) suggests there exists an optimal nanoparticle concentration, e.g., 3.5 v% herein, which would yield the minimum overall thermal resistance. Figure 5. 3(b) shows that the use of nanofluids becomes less appealing when a constant pumping power is prescribed, where  $(Q/Q_b)_p < 1$ .



(a)



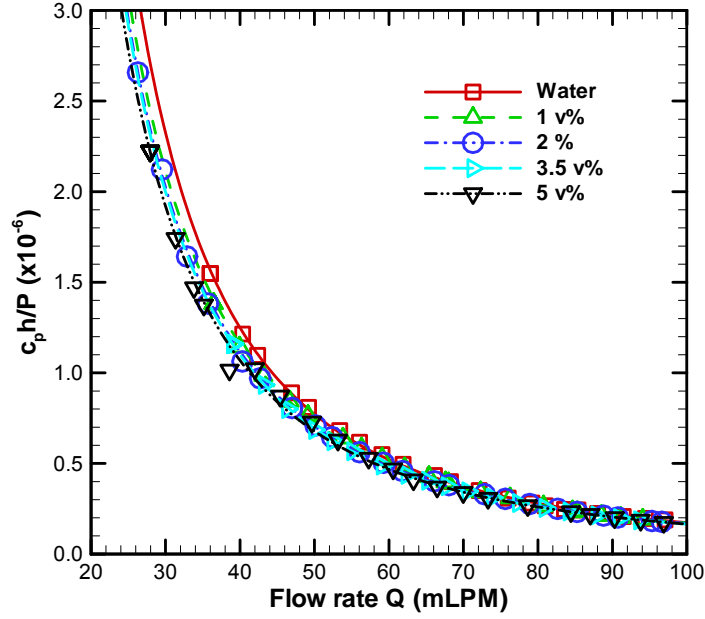
(b)

**Figure 5. 3.** Evaluation of  $(FOM)_r$  of  $Al_2O_3$ -water nanofluids presented in terms of  $(T_{w,o} - T_{in})$  using different bases of comparison: (a)  $Q$ -based and (b)  $P$ -based (heat flux  $q'' = 6.5 \text{ kW/m}^2$ ).

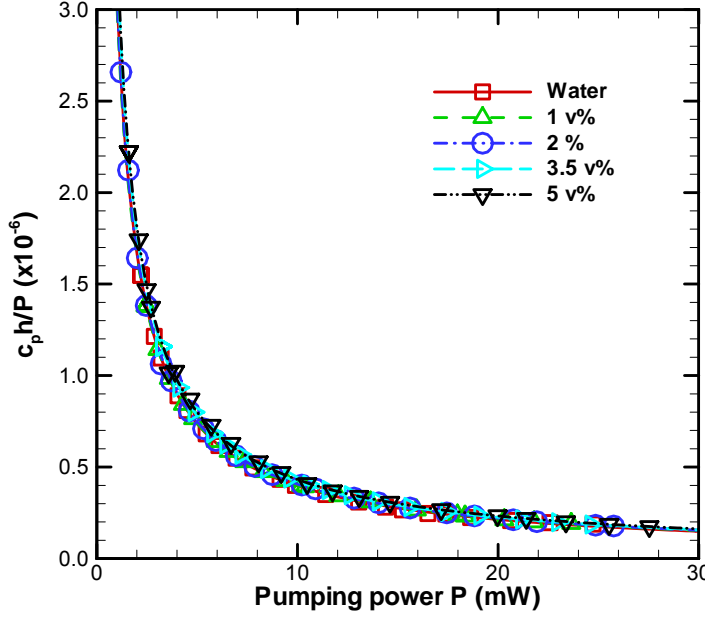
Figure 5.4 shows the evaluation of  $(FOM)_p$  for  $\text{Al}_2\text{O}_3$ -water nanofluids, expressed as the comparison of  $c_p h / P$ . The performance parameter  $c_p h / P$  offers a comprehensive measure of the effectiveness of a fluid for cooling applications, because it characterizes both the overall heat transfer performance ( $h$  represents heat removal from the heat source, and  $c_p$  represents thermal energy storage in the fluid) and the hydrodynamic performance ( $P$  is the power consumption to overcome the flow resistance). In Figure 5.4 (a) and (b), the data for the base fluid and nanofluids of various concentrations all fall on a single trend line, indicating there is essentially no improvement in  $(FOM)_p$  by the use of nanofluids. This is plausible from the thermal effectiveness perspective because the advantage of producing higher convective heat transfer with nanofluids is offset by the disadvantage of the lower specific heat and higher viscosity of the nanofluids. A scrutiny of Figure 5.4 (a) reveals that  $c_p h / P$  of the base fluid slightly surpasses that of the nanofluids at low flow rates, where a higher pumping power is required to yield the same flow rate for the nanofluids but the enhancement in heat transfer coefficient is disproportionate (see Figure 5. 2(c)). As the flow rate increases, the difference in  $c_p h / P$  between nanofluids and the base fluid quickly vanishes, since the increase in  $P$  is compensated by higher  $h$ .

Figure 5.5 shows the comparison of  $(FOM)_q$  for  $\text{Al}_2\text{O}_3$ -water nanofluids. The performance parameter  $q / P$  is in fact the coefficient of performance (COP) of the fluid, i.e., the ratio of heat dissipation to the pumping power needed to enable the cooling. The results are very similar to what is found in Figure 5.4: the nanofluids are modestly

outperformed by the base fluid under constant flow rate condition, whereas their performance is equal to the base fluid when the pumping power is fixed as constant.

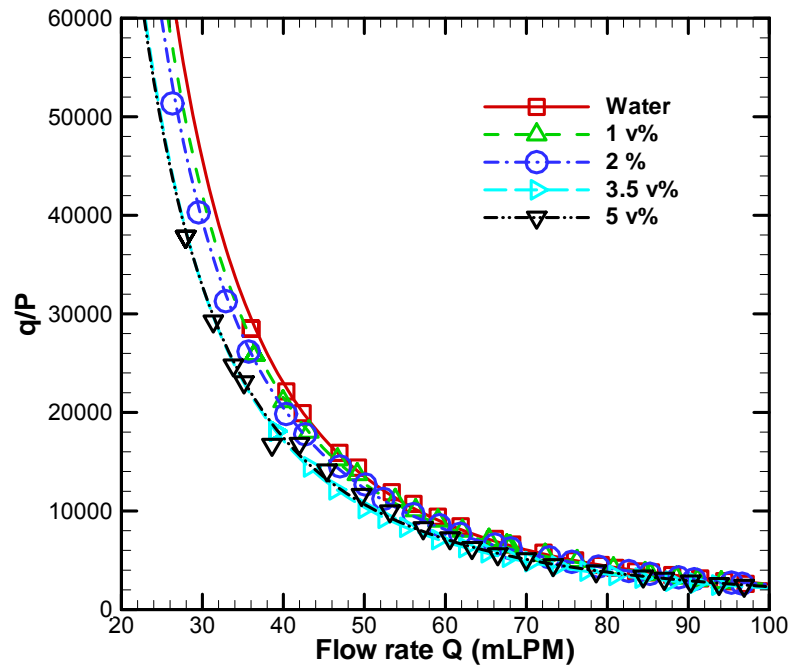


(a)

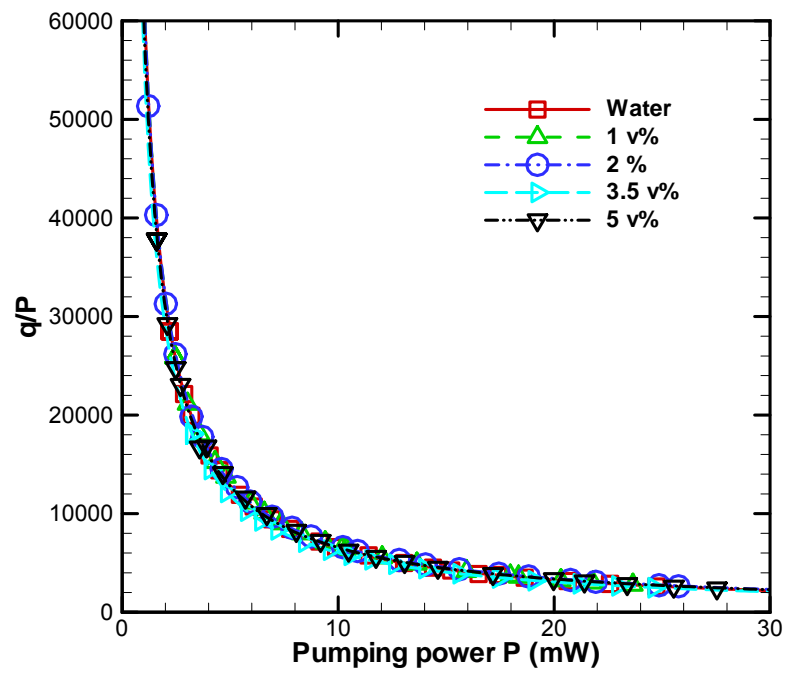


(b)

**Figure 5. 4.** Evaluation of  $(FOM)_p$  of  $Al_2O_3$ -water nanofluids presented in terms of  $c_p h / P$  using different bases of comparison: (a)  $Q$ -based and (b)  $P$ -based (heat flux  $q'' = 6.5 \text{ kW/m}^2$ ).



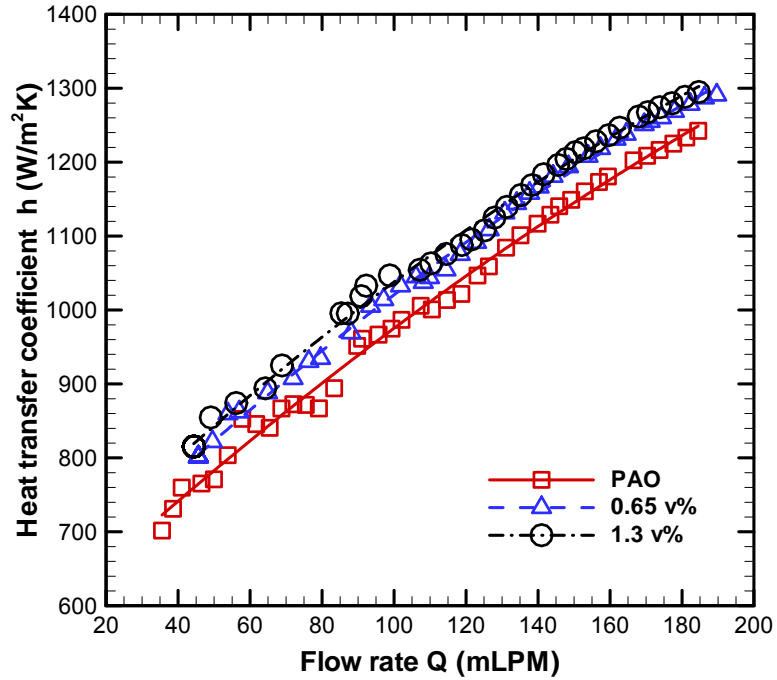
(a)



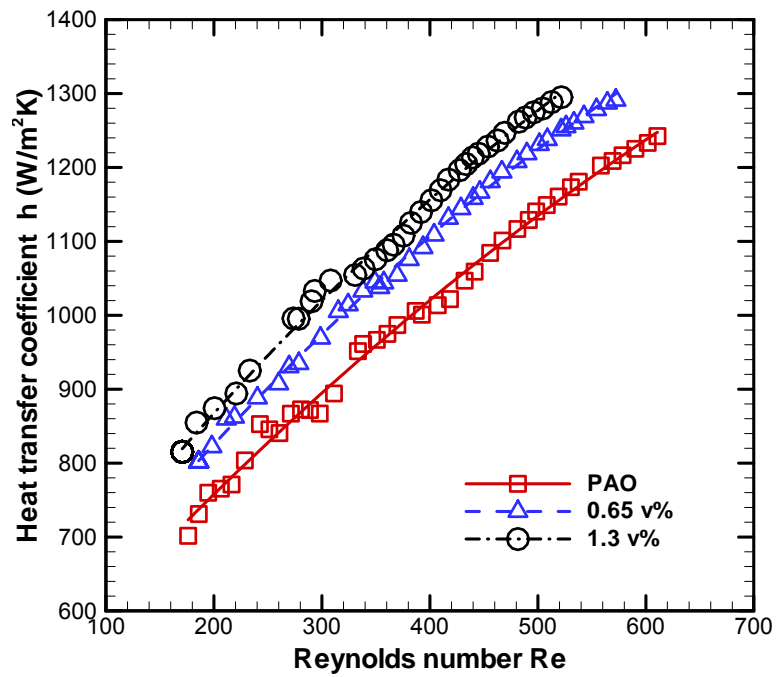
(b)

**Figure 5. 5.** Evaluation of  $(FOM)_Q$  of  $Al_2O_3$ -water nanofluids presented in terms of  $q/P$  using different bases of comparison: (a)  $Q$ -based and (b)  $P$ -based (heat flux  $q'' = 6.5 \text{ kW/m}^2$ ).

The thermal performance of Al<sub>2</sub>O<sub>3</sub>-PAO nanofluids is evaluated using the same group of FOM functions, and the results are illustrated in Figure 5. 6-Figure 5. 9. It has been shown from the previous discussion that  $(Q/Q_b)_{Re} > 1$  and  $(Q/Q_b)_P < 1$  in the forced convection of Al<sub>2</sub>O<sub>3</sub>-PAO nanofluids. Accordingly, the heat transfer enhancement in Figure 5. 6 is most appreciable when the convective flow is subject to the constant  $Re$  condition (Figure 5. 6(b)) where the actual fluid velocity is higher in the nanofluids than in the base fluid. Almost no heat transfer enhancement can be observed under the constant  $P$  condition (Figure 5. 6(c)) because the benefit of thermal conductivity enhancement in nanofluids on heat transfer is counteracted by their reduced flow velocity ( $(Q/Q_b)_P < 1$ ). The evaluation of  $(FOM)_T$  for Al<sub>2</sub>O<sub>3</sub>-PAO nanofluids is depicted in Figure 5. 7 with similar trends to Al<sub>2</sub>O<sub>3</sub>-water nanofluids. The thermal performance of nanofluids relative to the base fluid can be explained by the interplay of the effective thermal conductivity, the effective specific heat and the flow velocity of nanofluids under different flow constraints. The  $(FOM)_P$  and  $(FOM)_Q$  results in Figure 5. 8 and Figure 5. 9 resemble those obtained in Figure 5.4 and Figure 5.5 for Al<sub>2</sub>O<sub>3</sub>-water nanofluids. It is seen again that when the heat transfer performance and hydrodynamic performance are considered altogether, the nanofluids do not exhibit any overall enhancement over the base fluid and, therefore, the thermal effectiveness of nanofluids in liquid cooling applications is called into question.

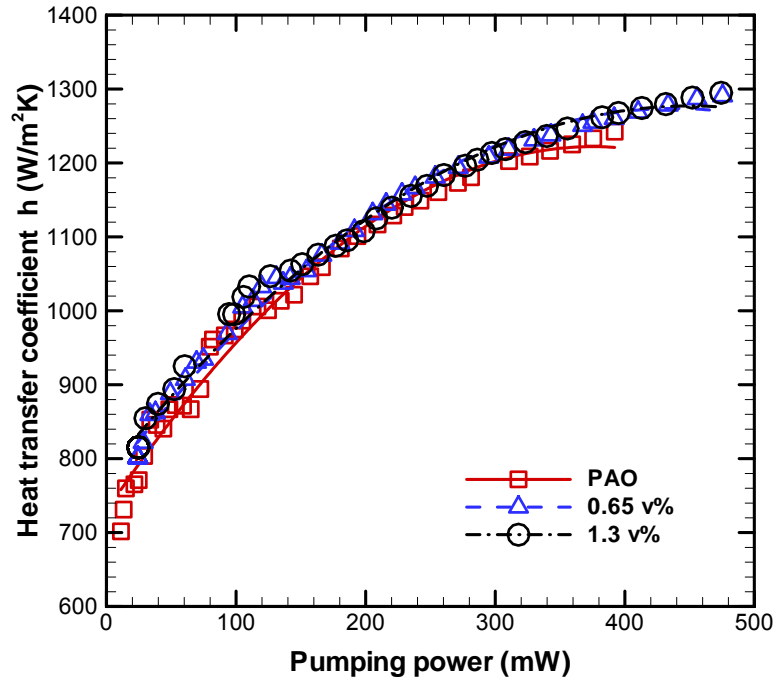


(a)



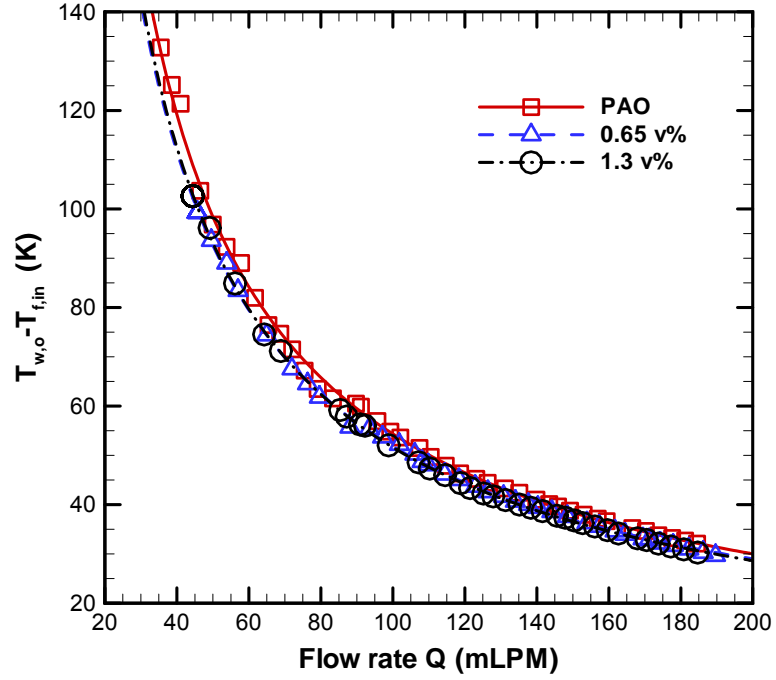
(b)

**Figure 5. 6.** Evaluation of  $(FOM)_h$  of  $Al_2O_3$ -PAO nanofluids presented in terms of convective heat transfer coefficient using different bases of comparison: (a)  $Q$ -based; (b)  $Re$ -based and (c)  $P$ -based (heat flux  $q'' = 6.5 \text{ kW/m}^2$ ).

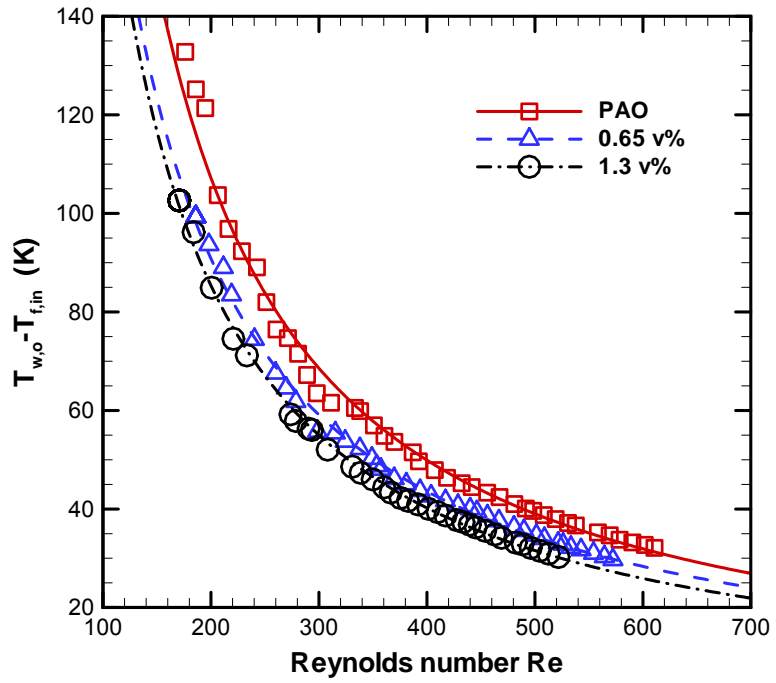


(c)

**Figure 5.6.** Evaluation of  $(FOM)_h$  of  $Al_2O_3$ -PAO nanofluids presented in terms of convective heat transfer coefficient using different bases of comparison: (a)  $Q$ -based; (b)  $Re$ -based and (c)  $P$ -based (heat flux  $q'' = 6.5 \text{ kW/m}^2$ ). [continued].

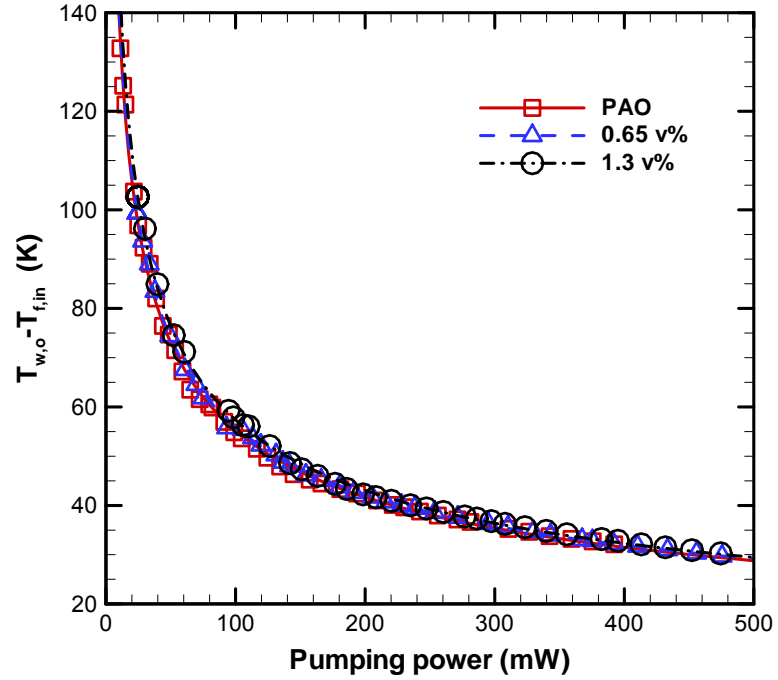


(a)



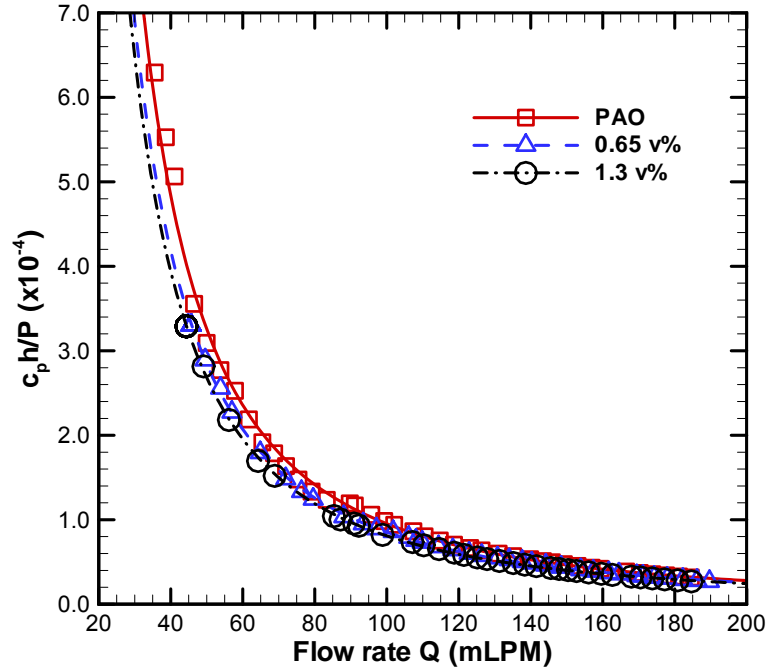
(b)

**Figure 5. 7.** Evaluation of  $(FOM)_T$  of  $Al_2O_3$ -PAO nanofluids presented in terms of  $(T_{w,o} - T_{f,in})$  using different bases of comparison: (a)  $Q$ -based; (b)  $Re$ -based and (c)  $P$ -based (heat flux  $q'' = 6.5 \text{ kW/m}^2$ ).

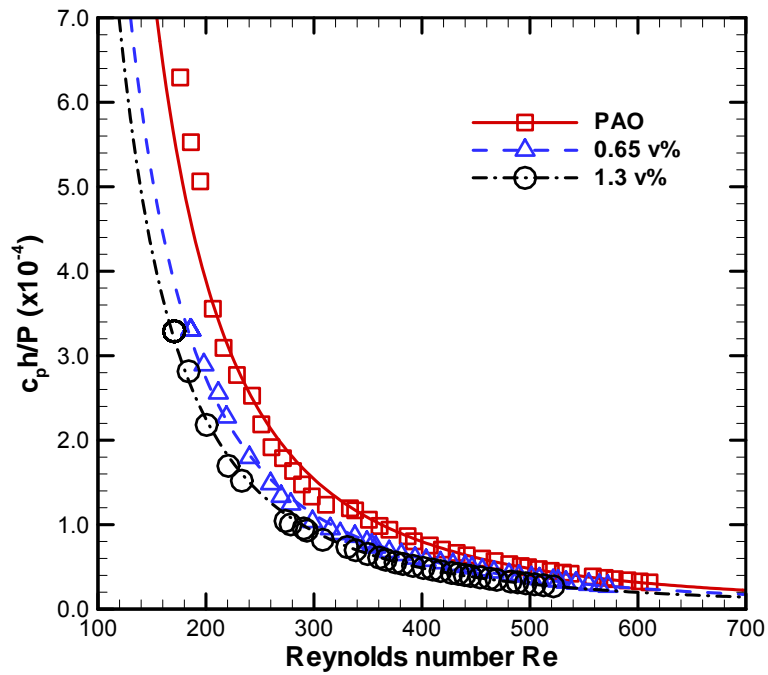


(c)

**Figure 5.7.** Evaluation of  $(FOM)_r$  of  $Al_2O_3$ -PAO nanofluids presented in terms of  $(T_{w,o} - T_{in})$  using different bases of comparison: (a)  $Q$ -based; (b)  $Re$ -based and (c)  $P$ -based (heat flux  $q'' = 6.5 \text{ kW/m}^2$ ) [continued].

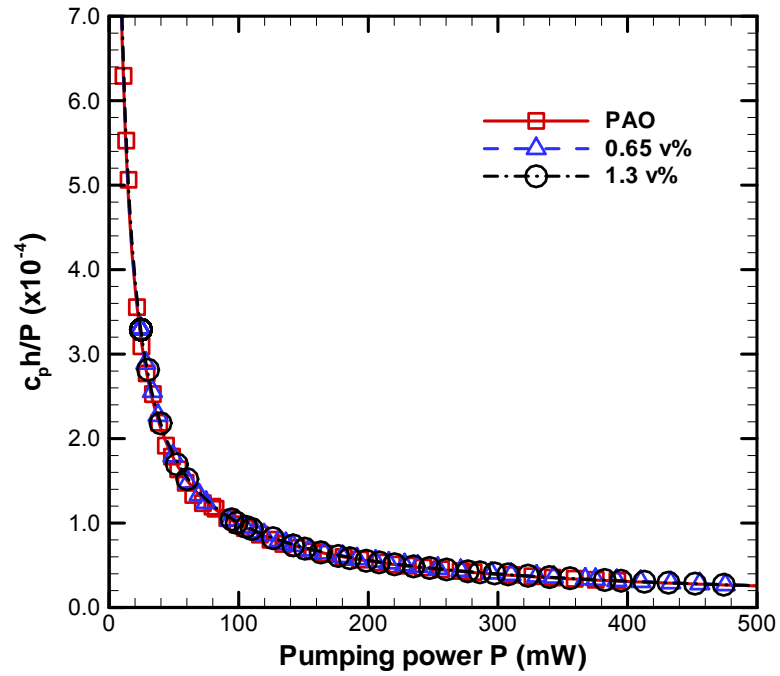


(a)



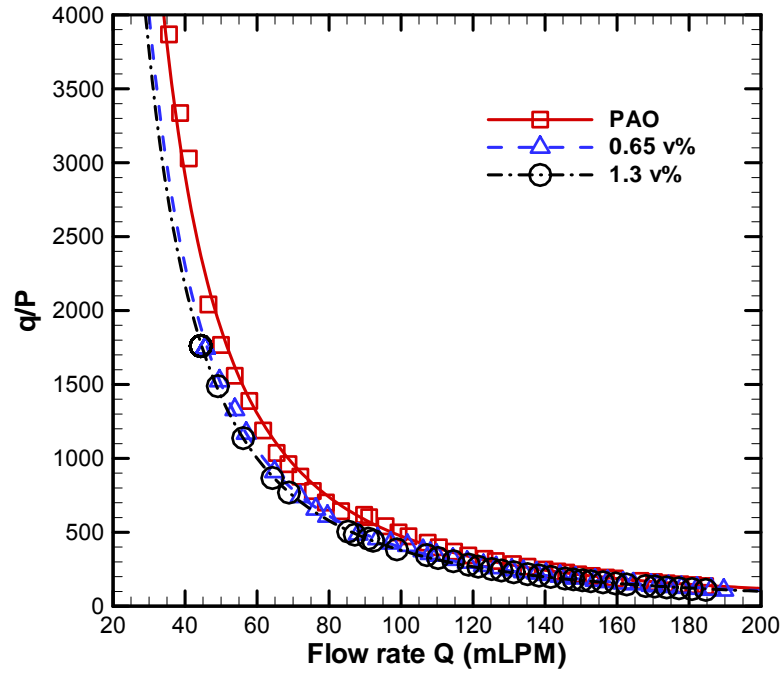
(b)

**Figure 5.8.** Assessment of  $(FOM)_p$  of  $\text{Al}_2\text{O}_3$ -PAO nanofluids presented in terms of  $c_p h/P$  using different bases of comparison: (a)  $Q$ -based; (b)  $Re$ -based and (c)  $P$ -based (heat flux  $q'' = 6.5 \text{ kW/m}^2$ )

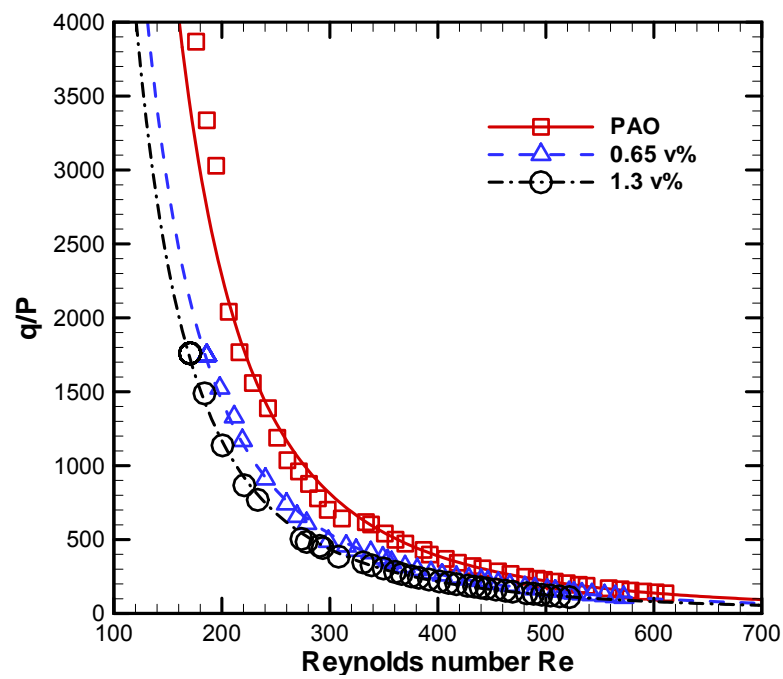


(c)

**Figure 5.8.** Assessment of  $(FOM)_p$  of  $Al_2O_3$ -PAO nanofluids presented in terms of  $c_p h/P$  using different bases of comparison: (a)  $Q$ -based; (b)  $Re$ -based and (c)  $P$ -based (heat flux  $q'' = 6.5 \text{ kW/m}^2$ ) [continued].

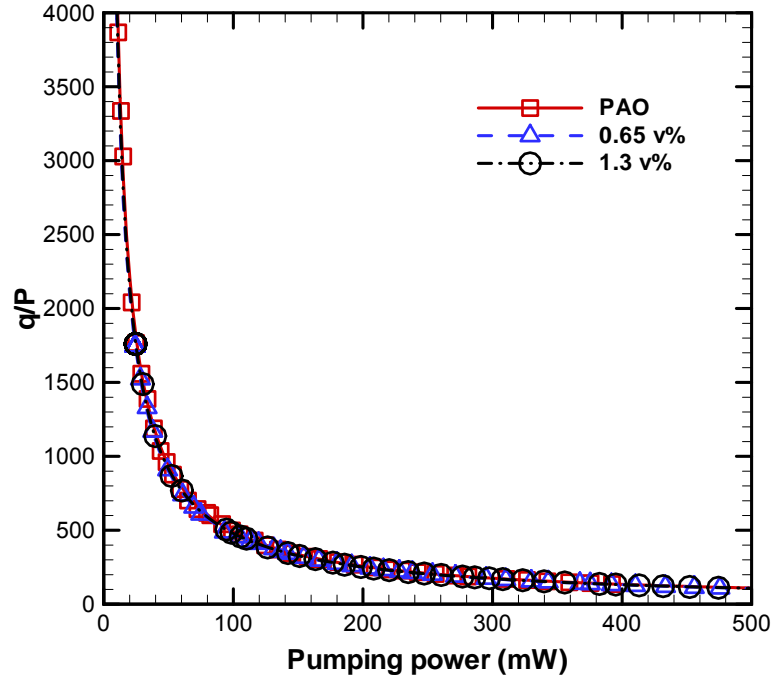


(a)



(b)

**Figure 5. 9.** Assessment of  $(FOM)_Q$  of  $Al_2O_3$ -PAO nanofluids presented in terms of  $q/P$  using different bases of comparison: (a)  $Q$ -based; (b)  $Re$ -based and (c)  $P$ -based (heat flux  $q'' = 6.5 \text{ kW/m}^2$ ).



(c)

**Figure 5.9.** Assessment of  $(FOM)_Q$  of  $Al_2O_3$ -PAO nanofluids presented in terms of  $q/P$  using different bases of comparison: (a)  $Q$ -based; (b)  $Re$ -based and (c)  $P$ -based (heat flux  $q'' = 6.5 \text{ kW/m}^2$ ) [continued].

## 5.4 SUMMARY

An experimental investigation was conducted to study the thermal effectiveness of  $Al_2O_3$ -water and  $Al_2O_3$ -PAO nanofluids in laminar forced convection. Based on the convective heat transfer and pressure drop measurements, four different forms of FOM, including  $(FOM)_h$ ,  $(FOM)_T$ ,  $(FOM)_p$  and  $(FOM)_Q$ , were critically evaluated for the nanofluids under three typical flow constraints, i.e., constant flow rate, constant Reynolds number and constant pumping power. The key findings can be summarized as follows.

1) Three effective thermophysical properties play an important role in the thermal performance of nanofluids. While the enhancement in thermal conductivity helps to

improve convective heat transfer, the higher viscosity necessitates more pumping power to enable the cooling, and the reduced specific heat adds to the caloric thermal resistance that hampers the heat to be transported out of the system. All three properties must be accounted for in evaluating the thermal effectiveness of nanofluids for real-world cooling applications.

2) Convective thermal performance of nanofluids depends on the constraints that are imposed on the flow, i.e., constant  $Re$ , constant  $Q$ , or constant  $P$ . Due to the variation in effective thermophysical properties, the actual flow velocity in the nanofluids may be different from that in the base fluid under the same flow constraint, thereby leading to different thermal performance.

3) The FOM evaluation results show that nanofluids appear meritorious if judged only from the heat transfer perspective, however, their overall thermal effectiveness for cooling applications is doubtful when the hydrodynamic performance and pumping power consumption are considered. In particular, virtually no difference in thermal performance can be found between nanofluids and the base fluid when the cooling application is constrained by constant pumping power condition.

## **CHAPTER 6. FLOW BOILING HEAT TRANSFER IN A MINICHANNEL**

### **6.1 INTRODUCTION**

Convective flow boiling and two-phase flow occur when the fluid is allowed to undergo phase change and boil. Utilizing the latent heat of the coolant, the two-phase heat exchangers are able to dissipate very high heat fluxes with a smaller amount of coolant than in the single-phase case. Another advantage of the two-phase convective boiling process is the resultant temperature uniformity in the heat exchangers, since the coolant will remain at its saturation temperature once the boiling commences. Therefore, it is natural to pose the following question: will flow boiling heat transfer be enhanced by the use of nanofluids?

Compared to the many studies that have investigated the thermophysical properties and single-phase convection of nanofluids, there have been very few studies related to boiling and two-phase heat transfer. Table 6.1 summarizes the experimental data available in the literature for nucleate boiling, critical heat flux (CHF), flow boiling and two-phase flow of nanofluids [133-153]. Conflicting experimental results have been obtained on nucleate pool boiling heat transfer, with some studies showing enhanced boiling heat transfer upon the addition of nanoparticles, and others showing inferior boiling performance of nanofluids relative to that of the base fluid. In contrast, most studies agree on the enhancement of CHF with nanofluids. A possible mechanism offered for the deterioration or enhancement of nucleate boiling heat transfer in nanofluids is nanoparticle deposition on the boiling surface which can change the active nucleation sites and surface wetting characteristics. Much more work is needed to

advance the understanding of nucleate pool boiling heat transfer and two-phase flow of nanofluids.

In light of this state of the art, several specific goals are identified for the research presented in this chapter:

- 1) Explore flow boiling heat transfer characteristics of nanofluids in a minichannel;
- 2) Study the effects of nanofluids on the onset of nucleate boiling (ONB) and develop a theoretical model to gain insight into the underlying mechanisms;
- 3) Investigate two-phase flow instabilities and study the effects of nanofluids on the transition boundaries of onset of flow instabilities (OFI).

**Table 6. 1. Boiling and Two-Phase Heat Transfer with Nanofluids.**

Reference	Particle Size and Concentration	Boiling Type	Experimental Conditions	Key Findings	Mechanisms and Models
Das et al. [133]	Al <sub>2</sub> O <sub>3</sub> -water 38 nm 1-4 v%	Pool boiling (on horizontal tubes)	Cylindrical heater D = 20 mm (Material not reported)  Surface roughness R <sub>a,smooth</sub> = 0.4 μm R <sub>a,rough</sub> = 1.1 μm	<ul style="list-style-type: none"> <li>• Nucleate boiling heat transfer deteriorates relative to the base fluid, and boiling curve shifts to the right.</li> <li>• Boiling heat transfer more adversely affected for roughened surface.</li> </ul>	<ul style="list-style-type: none"> <li>• Nanoparticles deposited on the heater surface reduce surface roughness and degrade boiling characteristics.</li> <li>• Boiling heat transfer correlations proposed for smooth and rough surfaces of the form <math>Nu = c_1 Re_b^{c_2} Pr^{0.4}</math></li> </ul>
Das et al. [134, 135]	Al <sub>2</sub> O <sub>3</sub> -water 58.4 nm 1-4 v%	Pool boiling (on horizontal tubes)	Cylindrical heater D = 4, 6.5, 20 mm (Material not reported)  Surface roughness R <sub>a</sub> = 0.37 to 0.45 μm	<ul style="list-style-type: none"> <li>• Nucleate boiling heat transfer deteriorates relative to the base fluid and boiling curve shifts to the right.</li> <li>• Boiling curve shift is not proportional to nanoparticle concentration and is strongly dependent on heater diameter.</li> <li>• Literature survey shows boiling heat transfer deterioration occurs at high particle concentrations (4-16 wt%), while enhancement occurs at lower concentrations (0.3-1.25 wt%).</li> </ul>	<ul style="list-style-type: none"> <li>• Nanoparticles deposited on heater surface form a porous layer, which increases surface wettability and improves CHF.</li> <li>• Boiling heat transfer depends on relative size of nanoparticles to surface roughness for cases where the number of active nucleation sites is increased upon nanoparticle deposition.</li> </ul>
Naranya et al. [136]	Al <sub>2</sub> O <sub>3</sub> -water 47 and 150 nm 0.5, 1, 2 wt%	Pool boiling (on vertical tubes)	Cylindrical heater D = 4, 6.5 and 20 mm (Material: stainless steel)  Surface roughness R <sub>a</sub> = 0.048 to 0.524 μm	<ul style="list-style-type: none"> <li>• Boiling heat transfer always enhanced on roughest heater and enhancement decreases with increasing nanoparticle concentration.</li> <li>• On smoother heater, boiling heat transfer may be enhanced or suppressed and decreases with increasing nanoparticle concentration.</li> <li>• On smoothest heater, boiling heat transfer is almost always suppressed and decreases with increasing nanoparticle concentration.</li> </ul>	<ul style="list-style-type: none"> <li>• Interface of nanoparticle and heating surface causes either increase or decrease in boiling heat transfer.</li> <li>• When nanoparticle size comparable to surface roughness, nucleation sites are suppressed and boiling heat transfer deteriorates.</li> <li>• When nanoparticle size smaller than surface roughness, nucleation sites increase and boiling heat transfer is enhanced.</li> </ul>

Reference	Particle Size and Concentration	Boiling Type	Experimental Conditions	Key Findings	Mechanisms and Models
Chopkar et al. [137]	ZrO <sub>2</sub> -water 20-25 nm 0.005-0.15 v%	Pool boiling	Plate heater D = 60.5 mm (Material: copper)  Surface roughness Ra = 0.5-0.7 μm	<ul style="list-style-type: none"> <li>• Nucleate boiling heat transfer reaches maximum at lowest concentration, and decreases with increasing concentration.</li> <li>• Nucleate boiling heat transfer decreases in nanofluid-surfactant mixture.</li> </ul>	<ul style="list-style-type: none"> <li>• Nanoparticle deposition decreases heater surface roughness and suppresses nucleation sites.</li> </ul>
Vassalo et al. [138]	SiO <sub>2</sub> -water 15, 50 nm 3 μm 0.5 v%	Pool boiling	Wire heater D = 0.4 mm Material: NiCr	<ul style="list-style-type: none"> <li>• Nanofluids have no noticeable effect on nucleate boiling heat transfer till CHF.</li> <li>• CHF increased 60% with nanofluids.</li> <li>• Addition of microparticles has similar effects on boiling heat transfer and CHF to addition of nanoparticles.</li> </ul>	<ul style="list-style-type: none"> <li>• Surface roughness improves heat transfer and CHF; however, this alone cannot explain CHF enhancement in nanofluids.</li> </ul>
Wen and Ding [139]	Al <sub>2</sub> O <sub>3</sub> -water 90-450 nm 0.32-1.25 wt%	Pool boiling	Plate heater D = 150 mm (Material: stainless steel)	<ul style="list-style-type: none"> <li>• Nucleate boiling heat transfer dramatically enhanced (40% with 1.25 wt%).</li> <li>• Heat transfer enhancement proportional to nanoparticle concentration and heat flux.</li> </ul>	<ul style="list-style-type: none"> <li>• Nanoparticle sedimentation and deposition detrimental to heat transfer.</li> <li>• Surface properties including roughness, wettability and contamination are important.</li> </ul>
Bang and Chang [140]	Al <sub>2</sub> O <sub>3</sub> -water 10-100 nm 47 nm 0.5-4 v%	Pool boiling	Plate heater 4 × 100 mm <sup>2</sup>  Material: copper	<ul style="list-style-type: none"> <li>• Boiling heat transfer lower than for pure water and decreases with increasing nanoparticle concentration.</li> <li>• Nucleate boiling is delayed.</li> <li>• CHF increases 32% for horizontal boiling and 13% for vertical boiling.</li> </ul>	<ul style="list-style-type: none"> <li>• Deterioration of boiling heat transfer contradictory to enhanced properties of nanofluids.</li> <li>• Nanoparticle deposition increases surface roughness causing fouling and suppressing active nucleation sites.</li> <li>• CHF enhancement due to reduced coalescence of bubbles.</li> </ul>
Milanova and Kumar [141]	SiO <sub>2</sub> -water 10 and 20 nm 0.5 v%	Pool boiling	Wire heater D = 0.32 mm (for NiCr) and D = 0.558 (for lead)	<ul style="list-style-type: none"> <li>• CHF increases with decreasing acidity, depending on nanoparticle size and pH level.</li> <li>• When no salts are present, negatively charged nanoparticles in NaOH solution remain stable and yield much higher CHF.</li> </ul>	—

Reference	Particle Size and Concentration	Boiling Type	Experimental Conditions	Key Findings	Mechanisms and Models
Milanova and Kumar [142]	SiO <sub>2</sub> -water 10 and 20 nm 0.5 v%	Pool boiling	Wire heater D = 0.32 mm (Material: NiCr)	<ul style="list-style-type: none"> <li>CHF increases to 267% for 10 nm nanoparticles and 147% for 20 nm nanoparticles relative to pure water.</li> <li>CHF depends strongly on the pH value.</li> </ul>	<ul style="list-style-type: none"> <li>pH value of nanofluids determines the charge on the nanoparticles and their mutual interaction with heating wire.</li> <li>Nanoparticle deposition leads to higher heat transfer and CHF.</li> </ul>
Liu et al. [143]	CuO-water 30 nm 0.1-2.0 wt%	Pool boiling	Smooth and grooved surfaces  (Material: copper) P = 7.4, 20, 100 kPa	<ul style="list-style-type: none"> <li>Nucleate boiling heat transfer and CHF increase with increasing nanoparticle concentrations (&lt;1 wt%).</li> <li>An optimum nanoparticle concentration of 1 wt% yields maximum heat transfer enhancement, beyond which CHF enhancement flattens and boiling heat transfer deteriorates.</li> <li>Decreasing pressure results in improved boiling heat transfer and CHF.</li> </ul>	—
Lee and Mudawar [144]	Al <sub>2</sub> O <sub>3</sub> -water 36 nm 1 v%	Flow boiling	Microchannel heat sink 215 × 821 μm <sup>2</sup> (Material: copper)	<ul style="list-style-type: none"> <li>No flow boiling achieved as nanoparticles deposit rapidly near the channel exit once boiling commences.</li> <li>Nanoparticles cluster quickly and fill the entire channel blocking coolant from entering flow channels.</li> </ul>	—
Park and Jung [145]	CNT-water CNT-R22  D = 20 nm L = 1 μm 1.0 v%	Flow boiling	Circular tube D = 102 mm L = 230 mm	<ul style="list-style-type: none"> <li>Addition of CNTs enhances boiling heat transfer by up to 28.7% at low heat flux; as heat flux increases, the enhancement deteriorates to 6.3%.</li> <li>No fouling was observed for CNT solutions on the heating wall.</li> </ul>	<ul style="list-style-type: none"> <li>Stephan and Abdelsalam correlation [14] and Cooper correlation [15] provide satisfactory prediction of nucleate boiling heat transfer.</li> </ul>
Xue et al. [146]	CNT-water  D = 15 nm 1.0 v%	Flow boiling		<ul style="list-style-type: none"> <li>Addition of CNTs deteriorates heat transfer of two-phase thermosyphon.</li> <li>Surface tension of water increases by 13.5% with addition of CNTs.</li> <li>Contact angle decreases due to addition of CNTs and surface wettability is improved.</li> </ul>	<ul style="list-style-type: none"> <li>Heat transfer is retarded due to decreased cavity site density, detachment frequency and lingering of coalesced vapor bubbles over heating surface.</li> </ul>

Reference	Particle Size and Concentration	Boiling Type	Experimental Conditions	Key Findings	Mechanisms and Models
Kim et al. [147]	TiO <sub>2</sub> -water 10-500 nm (mean: 85 nm) 10-5-10-1 v%	Pool boiling	Wire heater D = 0.2 mm (Material: NiCr)	<ul style="list-style-type: none"> <li>• At 0.1 v%, CHF increases to 200% relative to pure water.</li> <li>• Nanoparticle deposition on heating surface depends on particle concentration. More micron-sized structures form at high concentrations.</li> <li>• CHF enhancement of pure water on nanoparticle-coated heater exceeds CHF enhancement caused by nanofluids at high concentrations.</li> </ul>	<ul style="list-style-type: none"> <li>• CHF enhancement primarily due to modified surface characteristics (microstructure and topology) by nanoparticle deposition.</li> <li>• Ramilison correlation [ ] more accurate than Zuber's correlation [ ] in predicting CHF.</li> </ul>
Kim et al. [148]	Al <sub>2</sub> O <sub>3</sub> : 110-210 nm ZrO <sub>2</sub> : 110-250 nm SiO <sub>2</sub> : 20-40 nm 0.001-0.1 v%	Pool boiling	Flat heater 5 × 0.05 mm <sup>2</sup> (Material: stainless steel)	<ul style="list-style-type: none"> <li>• Surface wettability enhanced by nanoparticle layer deposited on heating surface.</li> <li>• Bubble nucleation decreased due to decrease of contact angle.</li> <li>• CHF delayed by increased surface wettability.</li> </ul>	<ul style="list-style-type: none"> <li>• Increased surface wettability caused by adhesion tension and surface roughness.</li> <li>• Active nucleation cavities decrease due to decrease of contact angle.</li> <li>• Contact angle reduction increases liquid layer thickness and delays dryout.</li> </ul>
Kim et al. [149]	Al <sub>2</sub> O <sub>3</sub> : 110-210 nm ZrO <sub>2</sub> : 110-250 nm SiO <sub>2</sub> : 20-40 nm 0.001- 0.1 v%	Pool boiling	Wire heater D = 0.381 mm Flat heater 5 × 0.05 mm <sup>2</sup> (Material: stainless steel)	<ul style="list-style-type: none"> <li>• Nucleate boiling heat transfer deteriorates.</li> <li>• CHF significantly enhanced at low concentrations of nanofluids.</li> <li>• Surface wettability improved by nanoparticle deposition on heating surface.</li> </ul>	<ul style="list-style-type: none"> <li>• CHF enhancement attributed to increased surface wettability due to nanoparticle deposition.</li> <li>• A review of four hypotheses, including hydrodynamic instability, macrolayer dryout, hot/dry spot and bubble interaction theories, suggests higher wettability increases CHF.</li> </ul>
Kim et al. [150]	Al <sub>2</sub> O <sub>3</sub> -water 40-50 nm 0.1 v%	Flow boiling	Circular tube D = 8.7 mm (Material: stainless steel) Flow rate < 0.15 kg/s	<ul style="list-style-type: none"> <li>• Nanofluids enhance CHF (by up to 30%) and yield higher exit quality.</li> <li>• Burnout modes different for nanofluids and pure water: extensive burnout with complete failure occurs in water vs. localized burnout with a pinhole-type failure for nanofluids.</li> </ul>	–

Reference	Particle Size and Concentration	Boiling Type	Experimental Conditions	Key Findings	Mechanisms and Models
Sefiane [151]	Al-ethanol Size not reported 1-5 wt%	Evaporation	Flat heater coated with polytetrafluoroethylene (PTFE)	<ul style="list-style-type: none"> <li>Depinning time for nanofluids longer than for the base fluid.</li> <li>CHF enhanced by the delay of dry spot spreading due to promoted contact line pinning with nanofluids.</li> </ul>	<ul style="list-style-type: none"> <li>Nanoparticles influence wetting and contact line behavior during evaporation.</li> <li>Structural disjoining pressure due to presence of nanoparticles affects force balance near three-phase region.</li> </ul>
You et al. [152]	Al <sub>2</sub> O <sub>3</sub> -water 0.001-0.025 g/l	Saturated pool boiling	Heater 10 × 10 mm <sup>2</sup> (Material: unknown)	<ul style="list-style-type: none"> <li>Boiling heat transfer coefficient not affected by nanofluids in nucleate boiling regime.</li> <li>CHF increased by 200% when nanoparticle concentration &gt; 0.005 g/l.</li> <li>Nucleate bubbles depart at much lower frequencies with larger size.</li> </ul>	<ul style="list-style-type: none"> <li>Zuber correlation [] insufficient in predicting CHF for nanofluids, suggesting parameters other than fluid properties may account for increased CHF.</li> </ul>
Xue et al. [153]	CNT-gum Arabic (GA) d = 15 nm L = 10 μm	Quenching (saturated)	Sphere D = 25 mm (Material: copper)	<ul style="list-style-type: none"> <li>During quenching, the sphere experiences film boiling, precipitous transplosion and pulsation and nucleation boiling.</li> <li>No difference in the nucleate and film boiling heat transfer was found for CNT nanofluid, but CHF is enhanced.</li> <li>Improved wettability enhances transitional boiling heat transfer and Leidenfrost point.</li> </ul>	<ul style="list-style-type: none"> <li>Increased CHF due to CNT deposition, which improves bubble removal from the surface.</li> </ul>

## 6.2 GENERAL FEATURES OF FLOW BOILING HEAT TRANSFER

The general features of flow boiling in channel flows can be observed from the boiling curve that illustrates the wall temperature variation as a function of heat flux. A schematic figure of the boiling curve is shown in [154]. The fluid enters the channel at point A as subcooled single-phase liquid. The heat transfer mode is single-phase convective heat transfer until location C, at which point the wall temperature exceeds the threshold value for the onset of nucleate boiling (ONB). From this point onward, both single-phase convection and nucleate boiling contribute to the total transfer of heat. The convective component is then swamped by boiling heat transfer from point D when the fully developed boiling region (FDB) starts. The intermediate region (C to D) is defined as the partial boiling regime. As fluid continues to absorb heat, saturated boiling is established at location E, when the bulk temperature reaches the local saturation temperature. Beyond this point, the vapor content increases steadily until dryout occurs.

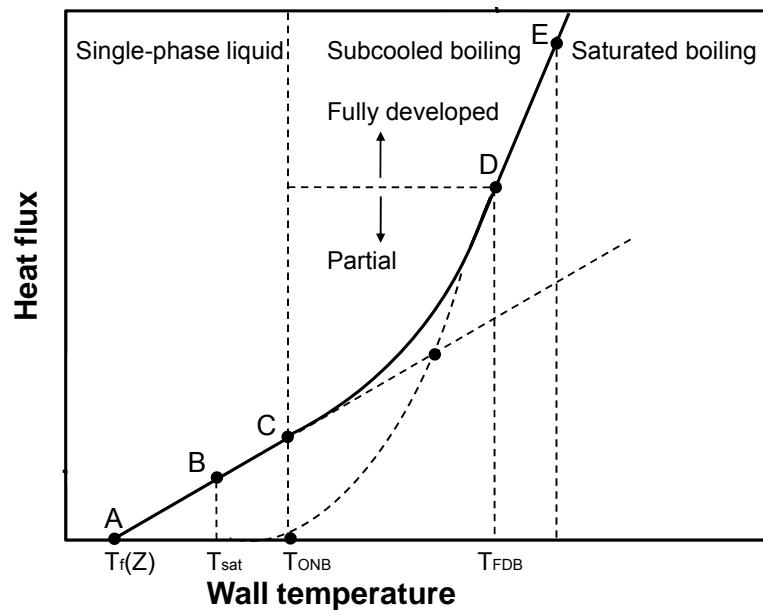


Figure 6. 1. Boiling curve.

## 6.3 FLOW BOILING HEAT TRANSFER EXPERIMENTS

### 6.3.1 EXPERIMENTAL APPARATUS

The experimental loop for the flow boiling heat transfer study of nanofluids is almost identical to that used in the single-phase heat transfer study, except for a few new components specially designed for boiling experiments (shown in Figure 6.2). A proportional integral derivative (PID)-regulated preheater (Infinity CRES-ILB-24-0040-K) was installed to control the inlet subcooling of the working fluid prior it entering the test section. A throttling valve was added near the exit of the test section to reduce possible feedbacks from the compressible volumes in the downstream piping system (such as the heat exchanger and the reservoir). Additionally, a drainage tank was installed after the throttle valve to help remove any dissolved gas escaping from the working fluid during the preheating stage before the flow boiling experiment starts.

The PID-regulated preheater is schematically shown in Figure 6. 3. Experiments were conducted to test its temporal response and temperature control accuracy. Figure 6.4 (a) shows that during the startup stage, the inlet fluid temperature (flow rate= 131.3mL/min) at the entrance of the test tube can be raised by the preheater from the room temperature (25°C) to the set value (88°C) within 60 minutes. Once the initial steady state is established, the PID control system can respond quickly to sudden adjustments, for instance, Figure 6.4 (b) depicts that when the set temperature is changed from 48°C to 77°C, the inlet fluid temperature will reach the desirable value within 10 minutes and the temperature fluctuations are less than 1°C under the new steady state.

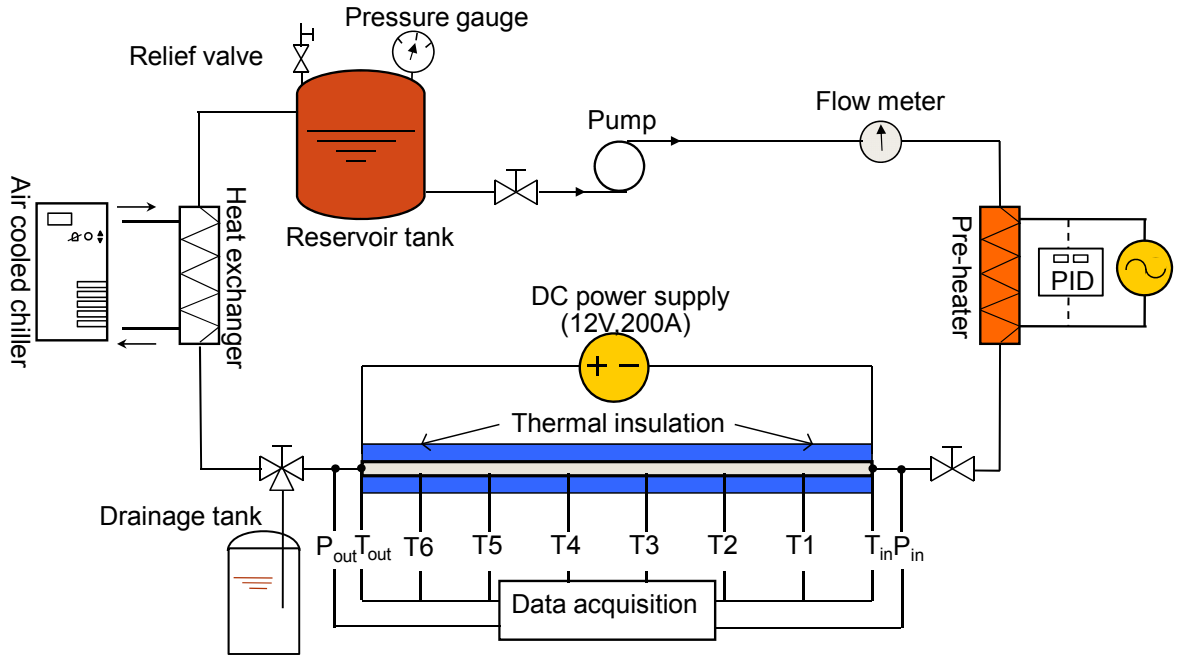


**Figure 6.2.** Schematic of experimental apparatus for flow boiling.

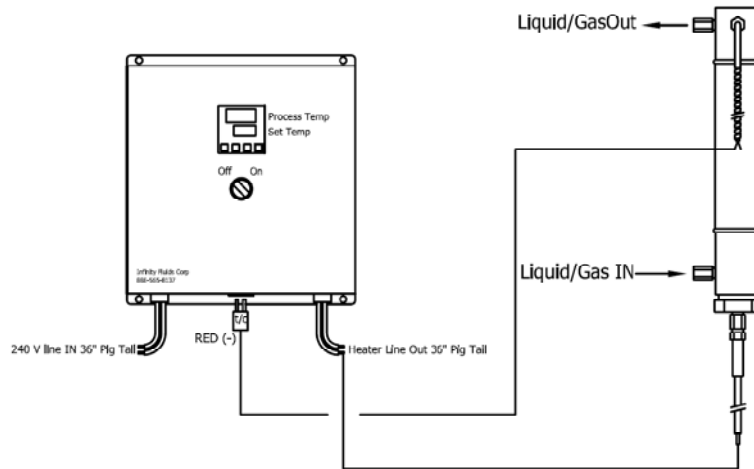
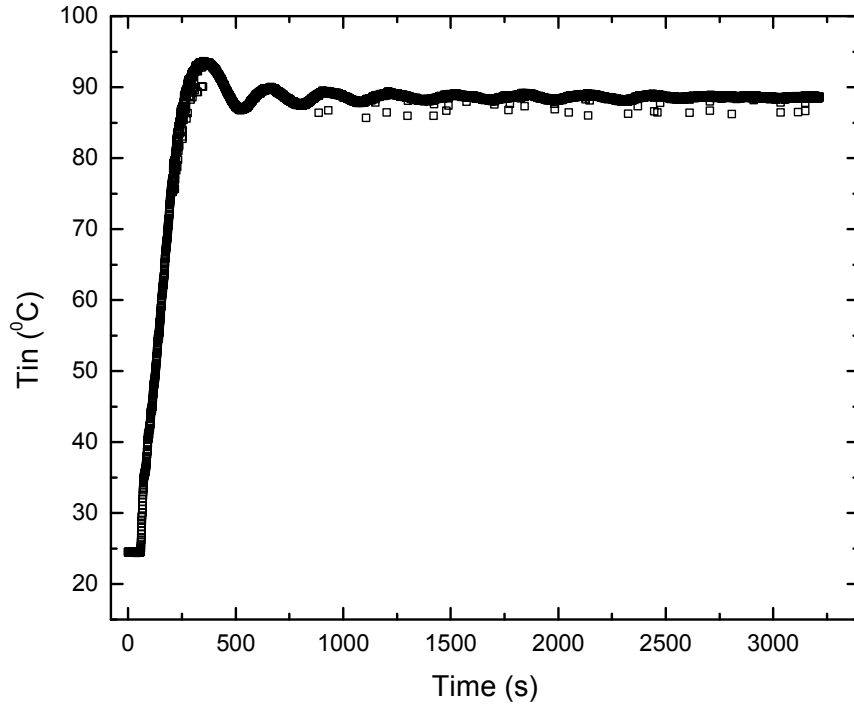
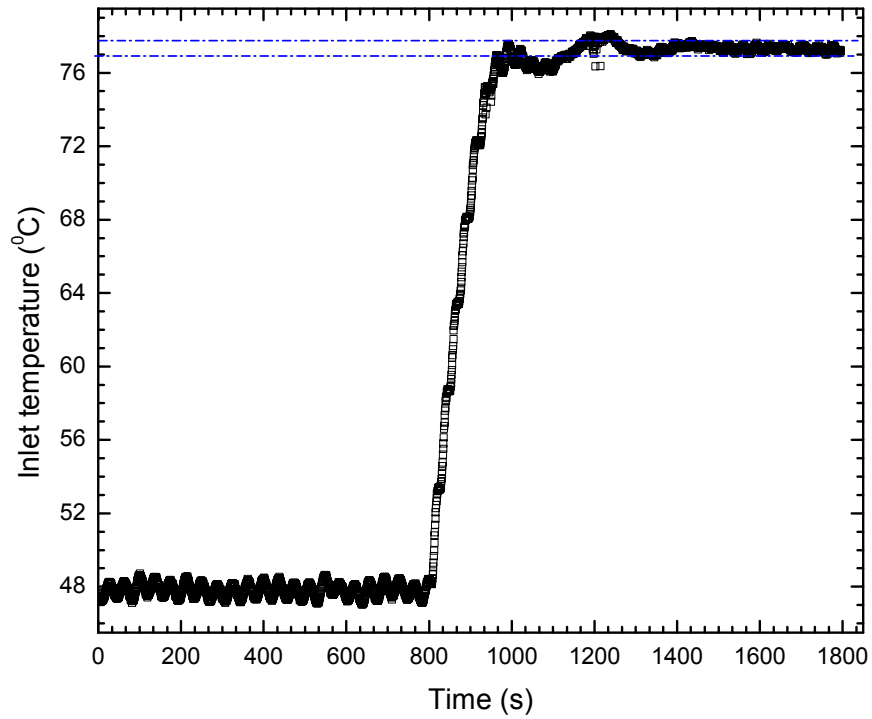


**Figure 6.3.** PID-regulated preheater for inlet subcooling control.



(a)



(b)

**Figure 6. 4.** Temporal variation of the inlet fluid temperature after running through the PID-regulated preheater (131.3mL/min).

### **6.3.2 PREPARATION OF NANOFLUIDS**

De-ionized (DI) water and  $\text{Al}_2\text{O}_3$ -water nanofluids were used as the working fluids in the flow boiling experiments. Nanofluids with two particle volume concentrations (0.01 v% and 0.1 v%) were prepared following the same procedures described in Chapter 2, except that DI water was degassed by vigorously boiling for about two hours before mixing with  $\text{Al}_2\text{O}_3$  nanoparticles. The amount of dissolved air in water was monitored with an oxygen sensor. Figure 6. 5 shows the time evolution of the measured oxygen concentration. If the degassed water is left unattended in the container, the oxygen concentration increases gradually from 3.6 mg/L to 5.0 mg/L during the first four hours, and reaches 7.7 mg/L at the end of the 24-hour period. The actual amount of dissolved air in the nanofluids was expected to be lower as the result of the sonication process when the nanofluids were synthesized. According to [155], if the concentration of dissolved oxygen is lower than 5.4 mg/L, the effect of dissolved air on boiling heat transfer can be safely neglected. This is expected to be the case for the present study.

### **6.3.3 CONTACT ANGLE MEASUREMENT**

Contact angle of a working fluid on the heater surface plays an important role in various aspects of nucleate boiling, such as onset of nucleate boiling (ONB) and critical heat flux (CHF). Kim et al. [156] measured the contact angle of water on inner surface of stainless steel tube both before and after flow boiling heat transfer experiments were conducted with alumina-water nanofluids of different concentrations. It was found that the contact angle decreases dramatically by 20-30° after the flow boiling experiments. Similar observations were made by other research groups [149, 157-159], and the reason was attributed to the deposition of nanoparticles on the heater surface.

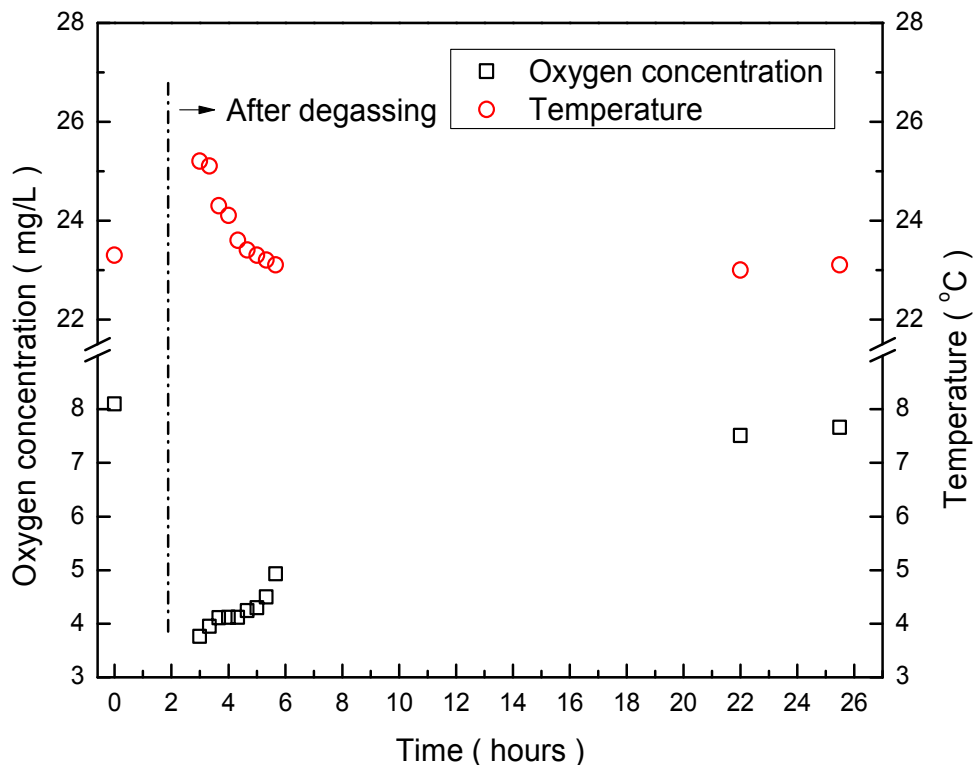


**Figure 6. 5.** Oxygen concentration and temperature of water variation with time.

In this study, the contact angle was measured for nanofluids on a flat stainless steel plate (Type 304), which is the same material of the minichannel test tube, using the sessile-drop method with a KSV tensiometer. Prior to each measurement, the test plate was cleaned with acetone and rinsed thoroughly with DI water. The typical measurement process is as follows: a 2- $\mu$ l droplet of the sample fluid was gently deposited by a syringe vertically down onto the test surface. The image of the droplet at the end of spreading was captured by a CCD camera (shown in Figure 6.6). The outer profile of the droplet was curve-fitted using a built-in image processing software, and the contact angle was calculated from the Young-Laplace theory. The results suggest that the contact angle of nanofluids is smaller than that of water on the same test surface, and it decreases with the

nanoparticle volume concentration. For instance, the contact angles are  $85.9^\circ$ ,  $82.7^\circ$  and  $76.0^\circ$  for water, 0.01 v%  $\text{Al}_2\text{O}_3$ -water nanofluid and 0.1 v%  $\text{Al}_2\text{O}_3$ -water nanofluid, respectively.

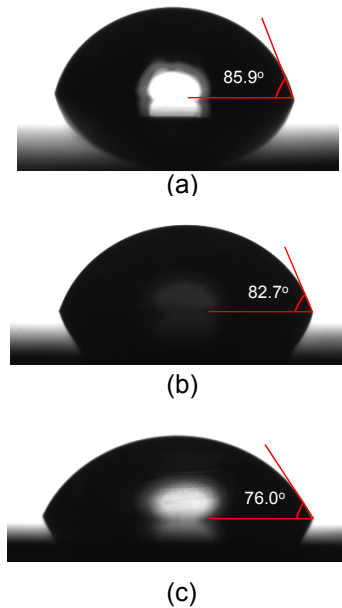


**Figure 6. 6.** Contact angle measurements on a stainless steel surface for (a) water, (b) 0.01 v%  $\text{Al}_2\text{O}_3$ -water nanofluid, and (c) 0.1 v%  $\text{Al}_2\text{O}_3$ -water nanofluid.

#### 6.3.4 TEST PROCEDURES

The test procedures for the flow boiling heat transfer experiments are as follows. The gear pump was first started to circulate the working fluid with the desired flow rate. Then the preheater was activated, and it usually took about 60 minutes for the fluid to reach the target temperature at the inlet of the minichannel. Afterwards, the DC power supply was turned on at the lowest power input level. A steady state was deemed to be reached when the readings from all thermocouples became and remained stable (within  $\pm 0.3^\circ\text{C}$ ) for at least 5 minutes. The measured parameters, including flow rate, pressure,

temperature, and applied voltage and current, were read into the data acquisition system, and each measurement value was calculated as an average of 300 readings. Following that, the power input was increased with small increment, and the procedure repeated for subsequent experiments. The inlet temperature of the test fluid ranged from 80.4 to 90.6 °C. The maximum heat flux achieved in the experiments was 40.6 W/cm<sup>2</sup>.

Similar procedures were taken for the two-phase flow instability experiments. Instead of controlling the power input, the flow rate was gradually reduced from the maximum value for subsequent tests. The corresponding mass flux obtained in the experiments ranged from 680 to 3100 kg/m<sup>2</sup>s. After reaching the minimum flow rate, one set of two-phase flow instability study was done, and the power input was then adjusted to a new level to repeat the above process. Five heat flux conditions were studied: 0, 19.9, 23.2, 26.2, and 29.9 W/cm<sup>2</sup>.

In the experiments, three different test samples were investigated: DI water, 0.01 v% Al<sub>2</sub>O<sub>3</sub>-water nanofluid and 0.1v% Al<sub>2</sub>O<sub>3</sub>-water nanofluid. To avoid the effect of nanoparticle deposition on the flow boiling heat transfer and two-phase flow, the minichannel test tube was replaced with a new one after the tests with each nanofluid sample.

### **6.3.5 DATA REDUCTION**

Heat loss from the test section to the ambient was first estimated under the single-phase heat transfer conditions, i.e., from the difference between the total power input and the sensible heat absorbed by the fluid

$$q_{loss} = q_{input} - \dot{m}c_p (T_{f,out} - T_{f,in}). \quad (6.1)$$

and the results were extrapolated to obtain heat loss under the flow boiling conditions, which was correlated as a function of the average wall temperature  $q_{loss} = q_{loss}(T_{w,m})$ . One example is given in Figure 6. 7 for  $G = 1374.7 \text{ kg/m}^2\text{s}$ ,  $T_{f,in} = 80.8^\circ\text{C}$ . Similar heat loss correlations were developed for each test condition.

The applied heat flux  $q_w''$  was calculated based on the inner area of the minichannel ( $A = \pi \cdot D \cdot L$ )

$$q_w'' = (q_{input} - q_{loss}) / A. \quad (6.2)$$

The boiling heat transfer coefficient was determined from

$$\bar{h}_p = \frac{q_w''}{T_w - T_f}, \quad (6.3)$$

in which  $T_w$  is the average temperature of the channel wall and  $T_f$  is the mean fluid temperature.

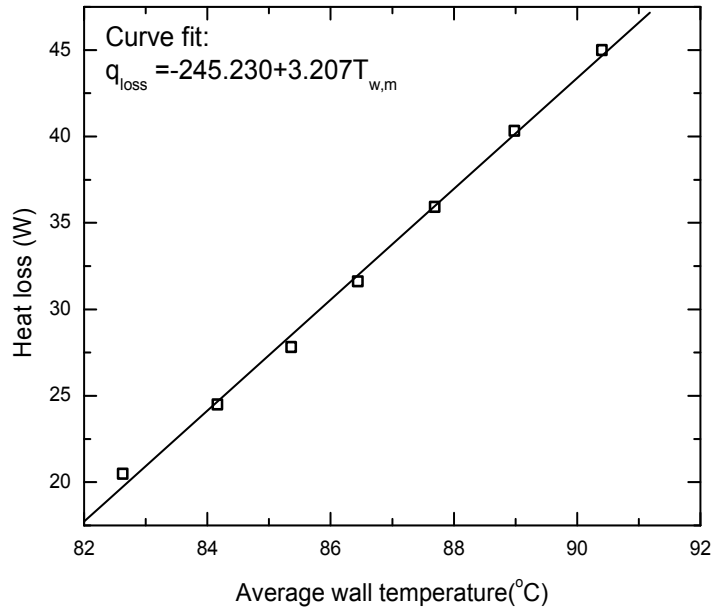


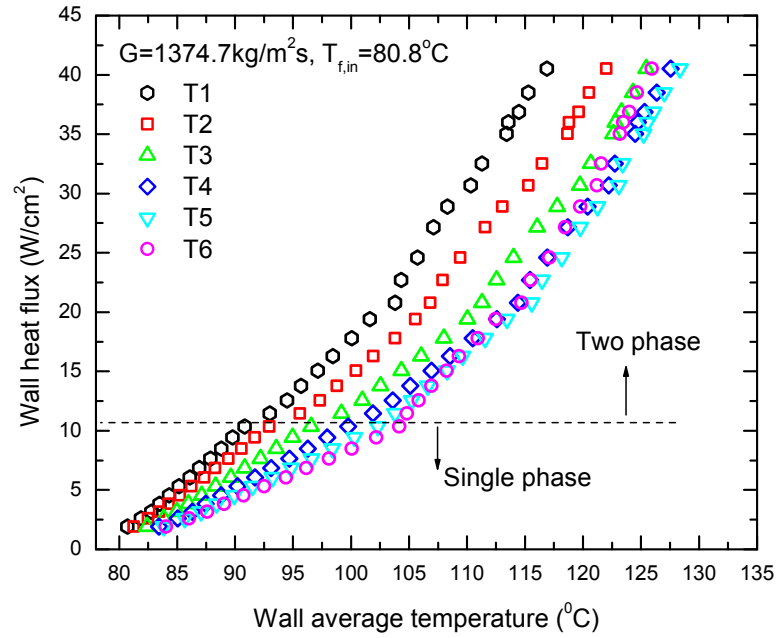
**Figure 6. 7.** Heat loss in experiment estimated from single phase data ( $G = 1374.7 \text{ kg/m}^2\text{s}$ ,  $T_{f,in} = 80.8^\circ\text{C}$ ).

Temperature-dependent thermophysical properties were used for of water and nanofluids in the data analysis. Since very dilute nanofluids were used in this study, the effect of nanoparticles on the saturation properties were neglected. Thus, the saturation temperatures of the fluid at the inlet and outlet of the minichannel were determined from the measured absolute pressures. A linear profile was then assumed for the local saturation temperature at any streamwise location between the inlet and outlet of the minichannel.

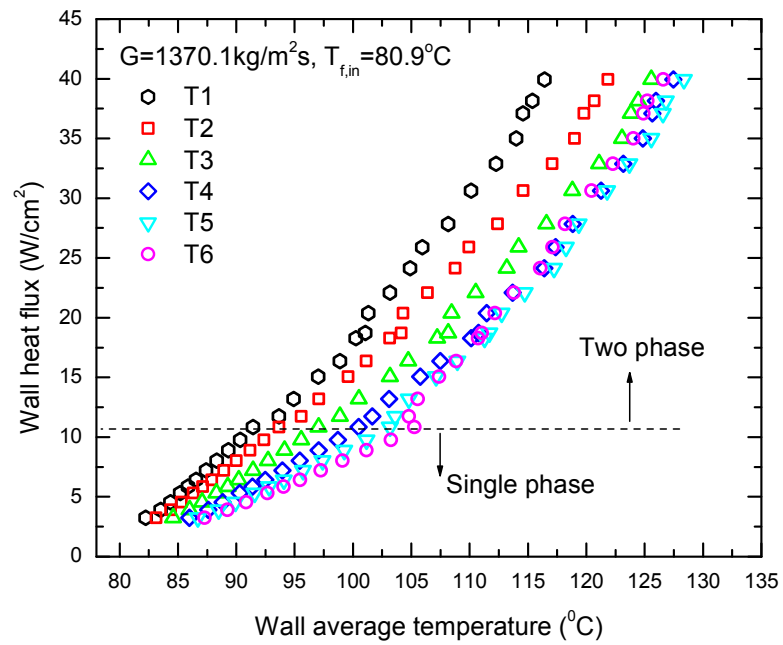
## **6.4 EXPERIMENTAL RESULTS**

### **6.4.1 BOILING CURVES**

Boiling curves were constructed for water and nanofluids using the wall temperatures measured at the six streamwise locations. Figure 6.8 shows that at low heat fluxes, single-phase flow prevails in the test fluids, and the steeper slope of the curves (i.e., higher convective heat transfer coefficient) obtained from the upper-steam thermocouples (T1, T2 and T3) clearly indicate the entrance region effect; when the heat flux is increased, the slope first changes for the measurement from T6, indicating the onset of nucleate boiling (ONB) occurs near the exit of the test tube and then gradually propagates toward upstream locations. Another important discovery is that the ONB takes place in nanofluids at higher heat flux as well as greater wall superheat. For instance, the ONB at the T6 location occurs at  $q'' = 10.4 \text{ W/cm}^2$  and  $T_w = 104.1^\circ\text{C}$  for water, but at  $q'' = 10.8 \text{ W/cm}^2$  and  $T_w = 105.3^\circ\text{C}$  for 0.01 v% nanofluid and at  $q'' = 18.4 \text{ W/cm}^2$  and  $T_w = 125.3^\circ\text{C}$  for 0.1 v% nanofluid.

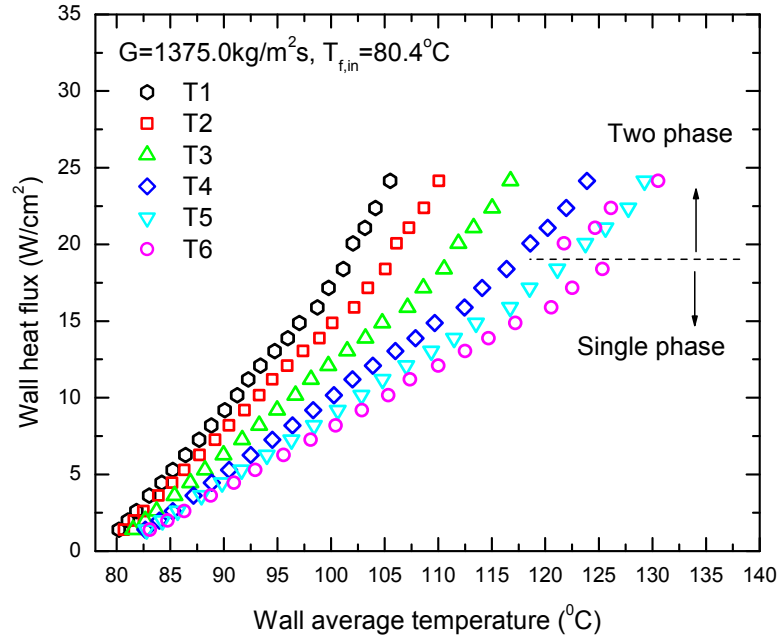


(a)



(b)

**Figure 6. 8.** Boiling curves for: (a) water, (b) 0.01 v% nanofluid, and (c) 0.1 v% nanofluid.



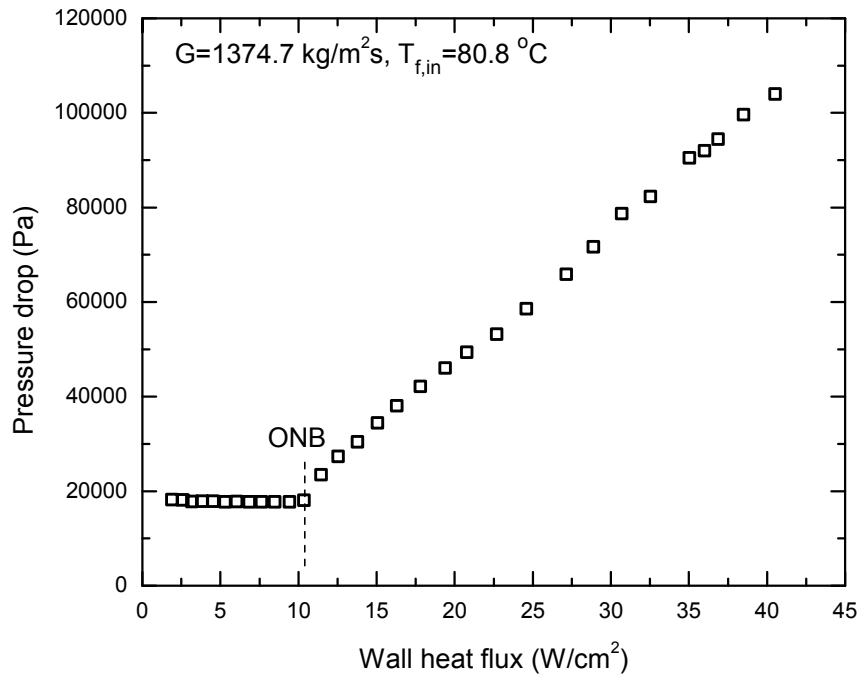
(c)

**Figure 6.8.** Boiling curves for: (a) water, (b) 0.01 v% nanofluid, and (c) 0.1 v% nanofluid [continued].

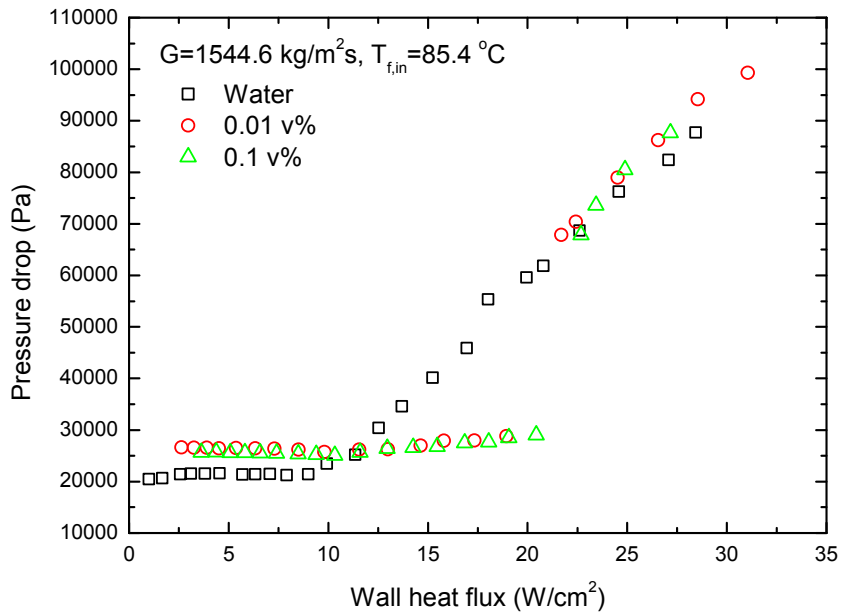
#### 6.4.2 PRESSURE DROP

The pressure drop across the minichannel was measured as a function of the applied heat flux. The result for water at  $G = 1374.7 \text{ kg/m}^2\text{s}$  and  $T_{f,in} = 80.8^\circ\text{C}$  is shown in Figure 6.9 (a). It is seen that in the single-phase region, the pressure drop decreases slightly as the wall heat flux increases, due to the lower viscosity of fluid at higher temperature. The decreasing trend persists until the onset nucleate of boiling (ONB) occurs at  $q'' = 10.35 \text{ W/cm}^2$ , which can be clearly identified from the abrupt change in the slope of the data. After ONB, the two-phase pressure drop increases almost linearly because the acceleration effect of the vapor content becomes pronounced. The observation of ONB is consistent with that from the boiling curve in Figure 6.8 (a) where

ONB occurs at the same heat flux. Similar pressure drop results are obtained for the nanofluids, as shown in Figure 6.9 (b), where the delayed ONB can be clearly identified.



(a)



(b)

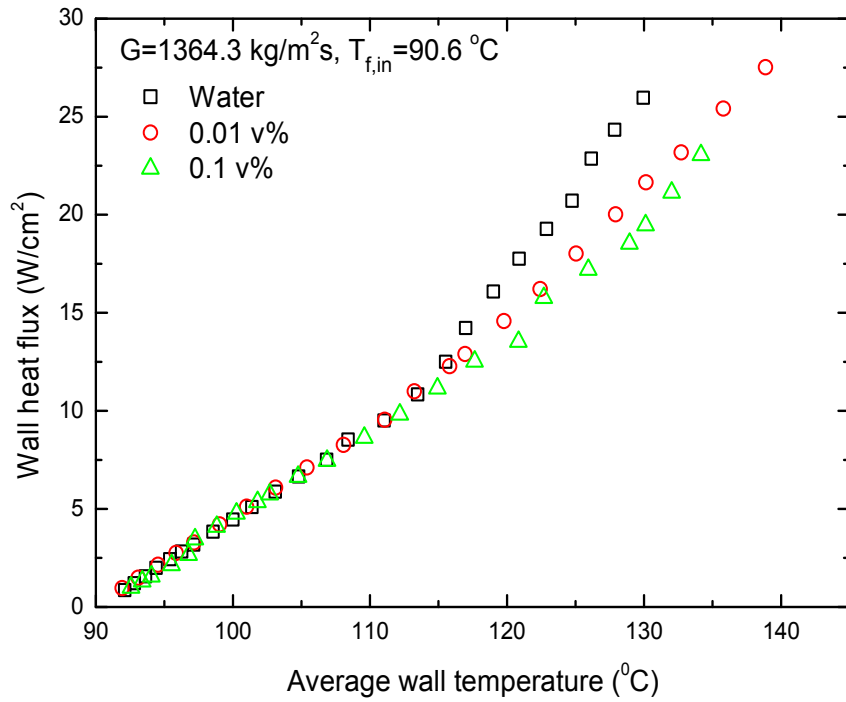
**Figure 6.9.** Two-phase pressure drop of (a) water and (b) nanofluids.

### 6.4.3 ONSET NUCLEATE OF BOILING

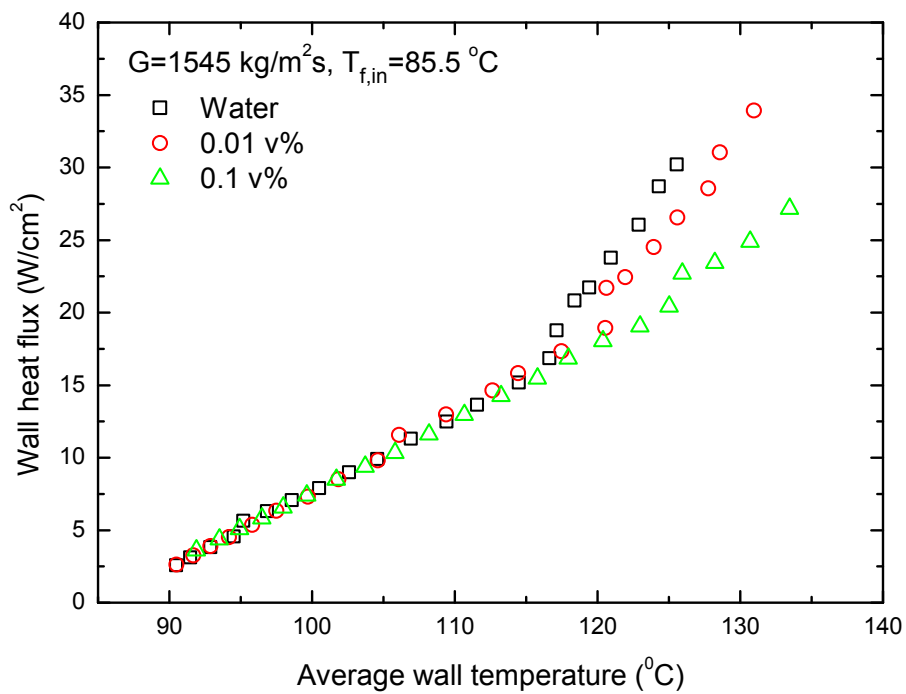
A careful examination of the boiling curves in Figure 6.8 has suggested that the ONB occurs at higher heat flux as the nanoparticle concentration increases, i.e., ONB is delayed in nanofluids. The delayed ONB can be distinguished more clearly from Figure 6.10 in which the boiling curves are constructed using the average wall temperature. Figure 6. 10 shows that the experimental data for all test fluids collapse together in single-phase region (due to the low particle concentration), but, once the ONB occurs, they start to deviate from the single-phase trend in the following order: first, water, then 0.01 v% nanofluid and, last, 0.1 v% nanofluid. Similar findings of delayed ONB were reported in pool boiling heat transfer experiments of nanofluids [160, 161], however, no other studies in the literature have been devoted to investigating the ONB characteristics in forced convective flow boiling of nanofluids. Furthermore, the delayed ONB has a great impact on the flow boiling instabilities in nanofluids (as will be discussed later). Therefore, the possible mechanisms for the delayed ONB are discussed next, and a theoretical model is also developed to gain some insight into the key parameters that govern the ONB in nanofluids.

It is postulated that two primary mechanisms are responsible for delaying the ONB in flow boiling of nanofluids:

- 1) The nanoparticle layer deposited on the inner surface of the test tube may alter the profile of active nucleation sites. It has been reported that once boiling takes place, nanoparticles will first aggregate at the liquid-vapor interface, and then quickly adhere to the wall surface [144].



(a)



(b)

**Figure 6. 10.** Comparison of Boiling curve.

As schematically shown in Figure 6. 11, smaller-sized cavities are completely filled by the nanoparticle aggregates while the larger ones may be partially filled. Consequently, the size range and number density of *available* nucleation sites will diminish, making it more difficult for ONB to occur.

2) From the previous single-phase heat transfer study, it is known that the thermal boundary layer development is retarded in nanofluid flow due to shear-induced nanoparticle migration. As discussed in [162], the size range of theoretically *eligible* nucleate cavities depends critically on the thermal boundary layer thickness. Therefore, the active nucleation sites will diminish in flow boiling of nanofluids.

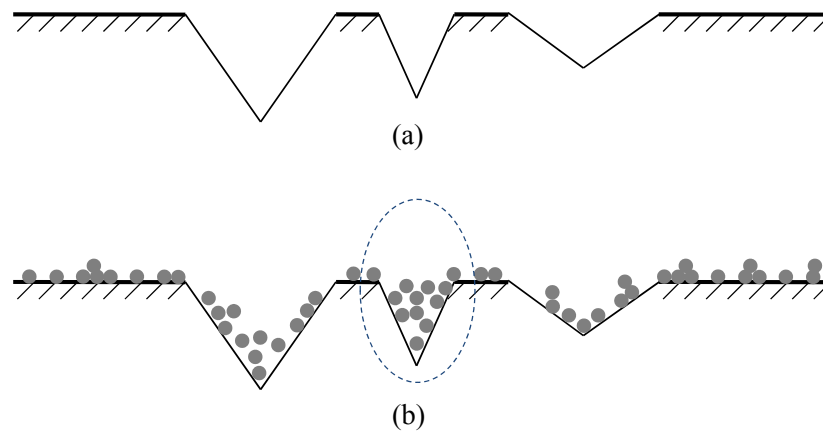


**Figure 6. 11.** Distribution of nucleation sites on a boiling surface before (a) and after (b) deposition of nanoparticles.

#### 6.4.4 ANALYTICAL MODEL FOR ONB

An analytical model was developed to illustrate the effect of nanofluids on the ONB from a different perspective, i.e., the impact of contact angle. This model follows the approach in [163, 164]. The key assumptions are:

- 1) The bubble nucleus takes the shape of a truncated sphere, as depicted in Figure 6.12;
- 2) The bubble nucleus does not change the temperature profile in the surrounding single-phase fluid;
- 3) The vapor and liquid phases are in equilibrium under saturated conditions;
- 4) A bubble nucleus will grow if the temperature of the fluid at a distance from the wall equal to the bubbles height is greater than the superheat requirement.

Equilibrium theory provides the superheat equation for the bubble nucleus:

$$T_b - T_s = T_b \frac{2\sigma}{\rho_v h_{fg} r_b} \quad , \quad (6.4)$$

where  $T_s(p_f)$  is written as  $T_s$  for brevity, and  $r_b$  is the bubble radius.

From , the following geometric relations are evident:

$$y_b = r_b (1 + \cos \theta) \quad , \quad (6.5)$$

$$r_c = r_b \sin \theta \quad . \quad (6.6)$$

The superheat equation, Eq.(6.4), can then be written as

$$T_b - T_s = T_b \frac{2\sigma(1 + \cos \theta)}{\rho_y h_{fg} y_b} = T_b \frac{2\sigma C}{\rho_y h_{fg} y_b} \quad , \quad (6.7)$$

where  $C$  is the shape factor,  $C = 1 + \cos \theta$  . This equation provides the superheat criterion for the onset of nucleate boiling. Rearrangement of Eq.(6.7) yields the vapor temperature

$$T_b = T_s / \left( 1 - \frac{2\sigma C}{\rho_y h_{fg} y_b} \right) \quad . \quad (6.8)$$

The local temperature of the fluid surrounding the bubble nucleus can be obtained from single-phase heat transfer together with assumption 2 in the previous section. In the vicinity of the channel surface, bulk convection is damped out so that a linear profile can be assumed for the fluid temperature in this region:

$$T_f(y) = T_w - q_w'' y / k_f. \quad (6.9)$$

Explicitly relating the wall temperature  $T_w$  to the effective wall heat flux  $q_w''$  in Eq. (6.9) allows for convective heat transfer features to be represented in the model.

Under the uniform heat flux boundary condition, the bulk mean temperature at the channel exit is derived from energy balance as

$$T_{f,out} = T_{f,in} + \frac{4q_w'' L}{\rho_f c_p u_0 D}. \quad (6.10)$$

The channel wall temperature is

$$T_w = T_f + \frac{q_w''}{(Nu_f k_f) / D}. \quad (6.11)$$

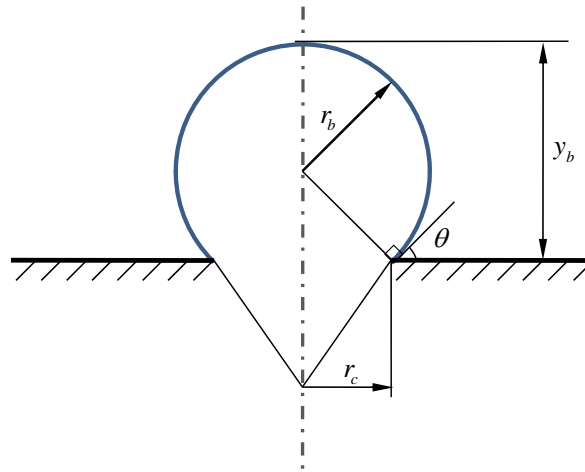
For water and dilute nanofluids in the laminar and turbulent flow regimes, the Nusselt number can be found from

$$\text{Laminar flow: } Nu_f = 1.86 (\text{Re Pr } D/L)^{1/3} (\mu_f / \mu_w)^{0.152}, \quad (6.12)$$

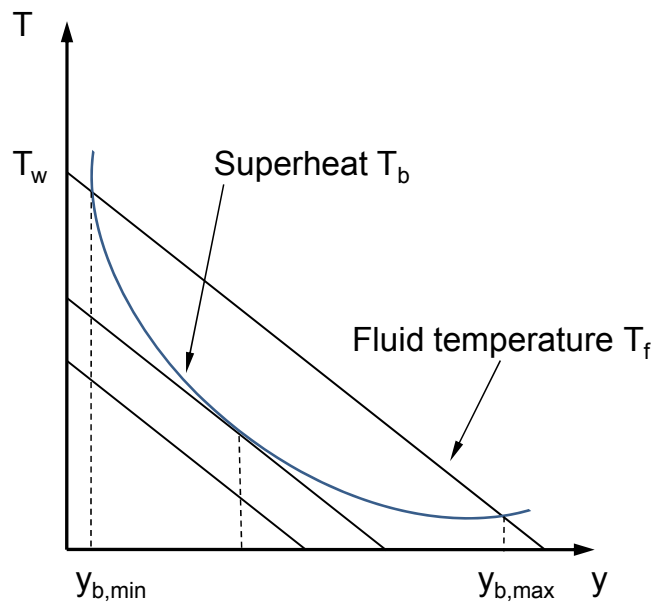
$$\text{Turbulent flow: } Nu_f = 0.116 (\text{Re}^{2/3} - 125) \text{Pr}^{1/3} [1 + (D/L)]^{2/3} (\mu_f / \mu_w)^{0.152}. \quad (6.13)$$

Nucleate boiling may occur only when  $T_f \geq T_b$  at the top of the bubble nucleus, as shown in Figure 6. 12. From Eq. (6.7) and (6.8), the necessary condition for ONB can be written as,

$$T_w - \frac{q_w''}{k_f} y_b = T_s / \left( 1 - \frac{2\sigma C}{\rho_v h_{fg} y_b} \right), \quad (6.14)$$



(a)



(b)

**Figure 6. 12.** Onset of nucleate boiling (a) an embryo bubble residing on the cavity, and (b) ONB superheat criterion.

the equation can further be rearranged in term of  $y_b$ :

$$\frac{q_w''}{k_f} y_b^2 - \left( T_w + \frac{2\sigma C}{\rho_v h_{fg}} \frac{q_w''}{k_f} - T_s \right) y_b + \frac{2\sigma C}{\rho_v h_{fg}} T_w = 0, \quad (6.15)$$

General solution of this equation is

$$y_b = \frac{\left( T_w + \frac{2\sigma C}{\rho_v h_{fg}} \frac{q_w''}{k_f} - T_s \right) \pm \sqrt{\left( T_w + \frac{2\sigma C}{\rho_v h_{fg}} \frac{q_w''}{k_f} - T_s \right)^2 - 4 \frac{2\sigma C}{\rho_v h_{fg}} \frac{q_w''}{k_f} T_w}}{2 \frac{q_w''}{k_f}}. \quad (6.16)$$

For both roots to be real, the determinant in (6.16) must be positive, i.e.,

$$\left( T_w + \frac{2\sigma C}{\rho_v h_{fg}} \frac{q_w''}{k_f} - T_s \right)^2 - 4 \frac{2\sigma C}{\rho_v h_{fg}} \frac{q_w''}{k_f} T_w \geq 0. \quad (6.17)$$

The superheat criterion can be obtained by rearranging this inequality

$$\sqrt{T_w} - \sqrt{T_s} \geq \sqrt{\frac{2\sigma C}{\rho_v h_{fg}} \frac{q_w''}{k_f}}. \quad (6.18)$$

Several interesting observations may be made from Eq. (6.18) as follows.

- 1) For given conditions, i.e., wall heat flux  $q_w''$ , fluid inlet velocity  $u_0$  and temperature  $T_{f,in}$ , the measured wall temperature  $T_w$ , or a value of  $T_w$  obtained from Eq. (6.11), may be substituted in the inequality Eq. (6.18) to determine if ONB will occur.
- 2) Conversely, if the fluid inlet conditions are prescribed and the heat flux allowed to vary, the threshold heat flux required to trigger the ONB can be predicted from the following equation:

$$\sqrt{T_{f,in} + \frac{q_w'' \pi D L}{\rho_f c_p u_0} + \frac{q_w''}{(Nu_f k_f) / D}} - \sqrt{T_s} = \sqrt{\frac{2\sigma C}{\rho_v h_{fg}} \frac{q_w''}{k_f}}. \quad (6.19)$$

Figure 6. 13 illustrates that the superheat criterion is satisfied only in the region  $y_{b,\min} \leq y_b \leq y_{b,\max}$ , where  $y_{b,\min}$  and  $y_{b,\max}$  represent the two roots of Eq. (6.15), respectively. Considering the geometric relation shown in Figure 6. 12, this requirement suggests that a cavity with radius  $r_c$  could be active [162] only if

$$r_{c,\min} \leq r_c \leq r_{c,\max}, \quad (6.20)$$

where

$$r_c^* = \frac{\left( T_w + \frac{2\sigma C}{\rho_v h_{fg}} \frac{q_w''}{k_f} - T_s \right)}{2 \frac{q_w''}{k_f}} \frac{\sin \theta}{1 + \cos \theta}, \quad (6.21)$$

$$r_{c,\min} = r_c^* - \frac{\sqrt{\left( T_w + \frac{2\sigma C}{\rho_v h_{fg}} \frac{q_w''}{k_f} - T_s \right)^2 - 4 \frac{2\sigma C}{\rho_v h_{fg}} \frac{q_w''}{k_f} T_w}}{2 \frac{q_w''}{k_f}} \frac{\sin \theta}{1 + \cos \theta}, \quad (6.22)$$

$$r_{c,\max} = r_c^* + \frac{\sqrt{\left( T_w + \frac{2\sigma C}{\rho_v h_{fg}} \frac{q_w''}{k_f} - T_s \right)^2 - 4 \frac{2\sigma C}{\rho_v h_{fg}} \frac{q_w''}{k_f} T_w}}{2 \frac{q_w''}{k_f}} \frac{\sin \theta}{1 + \cos \theta}. \quad (6.23)$$

Figure 6. 13 compares the predicted size range of active nucleation sites as a function of wall temperature for different contact angles. It is seen that the minimum wall superheat required for initiating ONB increases with decreasing contact angle, i.e., for higher nanoparticle concentrations. On the other hand, at a fixed wall superheat, the size range of active nucleation sites becomes narrower for denser nanofluids. The above analysis proves that, as the contact angle decreases with nanofluids, the ONB will be delayed due to the diminishing range of active nucleation sites.

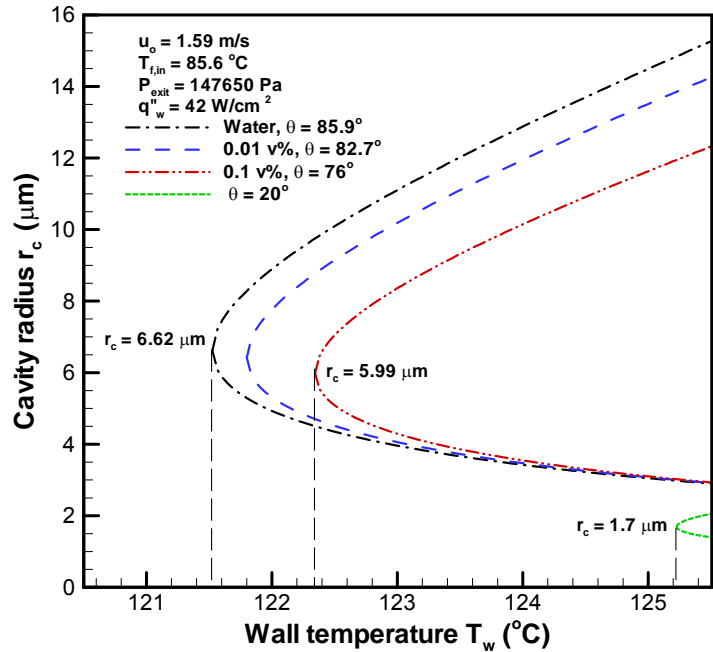


**Figure 6.13.** Size range of active nucleation sites as a function of wall temperature for different contact angles.

## 6.5 TWO-PHASE FLOW INSTABILITY

Two-phase flow systems are often accompanied by small scale fluctuations, including two-phase interfacial waves as well as oscillations of flow rate and system pressure, which, if not suppressed, may trigger large scale two-phase instabilities. The two-phase flow instabilities are undesirable and can change a steady phase heat transfer process to the point at which the operation of the heat transfer equipments goes beyond the designed safety regime. For instance, severe flow rate and pressure oscillations can cause mechanical vibrations and problems in system control, and in extreme cases, degrade the heat transfer characteristics so that the heat transfer surface may burn out due to drastic increase in wall temperatures. Additionally, the periodic cycling of the wall temperature will induce in thermal stresses in the wall materials that may build up and eventually lead to mechanical breakdown and other more serious accidents [165].

Therefore, flow instability control is of great importance to two-phase thermal systems such as two-phase heat exchangers, water-cooled nuclear reactors and steam generators, which requires a fundamental understanding of the physical mechanisms that set off the two-phase instabilities.

### **6.5.1 CLASSIFICATIONS OF TWO-PHASE FLOW INSTABILITIES**

A two-phase flow is stable if, when disturbed, the flow system can return asymptotically to the original operating state; otherwise, the flow is subject to instabilities. Two-phase flow instability usually arises from the interactions between the internal and external flow characteristics, and can be classified into two categories: static instability and dynamic instability [166].

Static instability occurs when the new operating conditions of the disturbed system tend asymptotically toward the ones that are different from the original ones. The sources of static instability are intrinsic to the steady-state operation of the flow system, and obey the steady-state laws [167, 168]. Ledinegg instability is the most common static instability in two-phase flow. It takes place when the slope of the two-phase flow demand curve (the internal pressure drop vs. mass flux curve) is negative and steeper than the pump supply curve (the external pressure drop vs. mass flux curve) and multiple intersections are possible in the internal and external characteristic curves [169]. The detailed mechanism is illustrated in Figure 6. 14 where the internal two-phase characteristic curve A has a negative slope region in addition to two positive slope region and it intersects the external pump characteristic curve B at multiple locations, *a*, *b* and *c*.

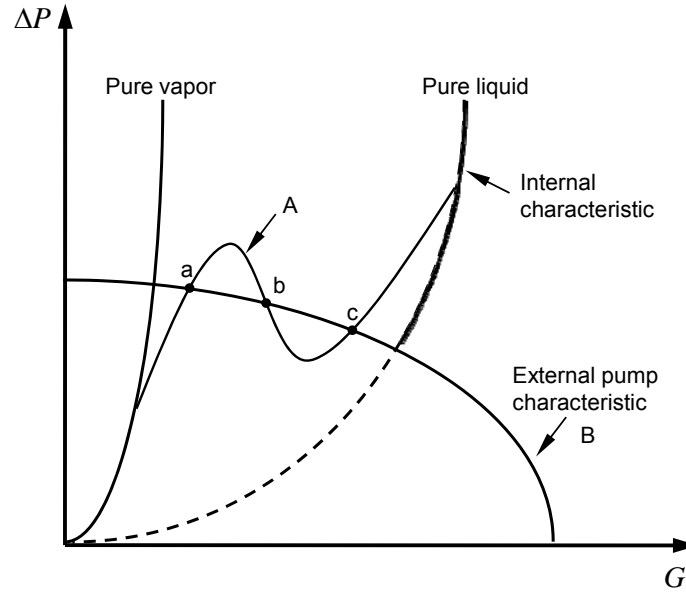


**Figure 6. 14.** Ledinegg instability.

If a small perturbation causes the mass flux to decrease slightly from point *b*, a higher pressure drop must be overcome to sustain the two-phase flow (i.e., the operating point moves up along the internal curve *A*). However, since near point *b* the external characteristic is less steep than the internal characteristic, the pump is unable to provide sufficient pressure head as demanded. Accordingly, the disparity between the available and required pressure drops will further reduce the mass flux, driving the flow to continue to move upward on curve *A* till the slope becomes positive. The system will ultimately reach a new equilibrium at point *a* where the supply and requirement of pressure drop are equal. Using a similar argument, it can be found that a perturbation that increases the mass flow rate at point *b* will cause the operating point to shift spontaneously to point *c*. In either case, the operation at point *b* is unstable. Other types of static instabilities and their key features have been studied extensively in the literature [165, 168, 170], and are summarized in Table 6. 2 [165].

The two-phase flow is subject to dynamic instability when the interaction and delayed feedback between the inertia of flow and compressibility of the two-phase mixture play a major role in stimulating instability. Dynamic instabilities are generally characterized in terms of oscillatory behaviors of flow parameters such as the mass flux, inlet pressure and wall temperatures [171]. Four types of dynamic instabilities have been identified by Boure et al. [168] and Kakac [172], which include density-wave type oscillation, pressure-drop type oscillation, thermal oscillation and acoustic oscillation. The physical mechanisms and salient characteristics of these dynamic instabilities can be found from Table 6. 2. In the following, three major types of dynamic instabilities will be briefly reviewed.

**Table 6. 2. Two-phase flow instabilities [165].**

Category	Type	Mechanism	Characteristics
Static instabilities	Ledinegg instability	Internal characteristics steeper than external characteristics in a negative slope region.	Flow undergoes sudden, large amplitude excursion to a new stable operating condition.
	Boiling crisis	Ineffective removal of heat from heated surface.	Wall temperature excursion and flow oscillation.
	Flow pattern transition instability	Bubbly flow has less void but higher pressure drop than annular flow.	Cyclic flow pattern transitions and flow rate variation.
	Bumping, Geysering, or Chugging	Periodic adjustment of metastable condition, usually due to lack of nucleation sites.	Periodic process of super-heat and violent evaporation with possible expulsion and refilling.
Dynamic instabilities	Density-wave oscillations	Delay and feedback effects in relationship between flow rate, density, and pressure-drop.	Frequencies related to transit time as a continuity wave.
	Pressure-drop oscillations	Dynamic interaction between channel and compressible volume.	Very low frequency periodic Process.
	Thermal oscillations	Interaction of variable heat transfer coefficient with flow dynamics.	High magnitude temperature oscillations in the solid due to transitions between different boiling regimes.
	Acoustic oscillations	Resonance of pressure waves.	High frequencies (10-100 Hz) related to time required for pressure wave propagation in System.

The two-phase flow is subject to dynamic instability when the interaction and delayed feedback between the inertia of flow and compressibility of the two-phase mixture play a major role in stimulating instability. Dynamic instabilities are generally characterized in terms of oscillatory behaviors of flow parameters such as the mass flux, inlet pressure and wall temperatures [171]. Four types of dynamic instabilities have been identified by Boure et al. [168] and Kakac [172], which include density-wave type oscillation, pressure-drop type oscillation, thermal oscillation and acoustic oscillation. The physical mechanisms and salient characteristics of these dynamic instabilities can be found from Table 6. 2. In the following, three major types of dynamic instabilities will be briefly reviewed.

#### **6.5.1.1 DENSITY-WAVE OSCILLATIONS**

Density-wave oscillations are caused by multiple regenerative feedbacks between the mass flux, vapor generation rate and two-phase pressure drop [168, 173], during which fluid waves of mixtures of alternately higher and lower density (i.e., liquid and vapor) travel along the flow channel. Since the density-wave oscillations are related to kinematic wave-propagation, they are also noted as "flow-void feedback instability." As shown in Figure 6. 15, the oscillation amplitudes and periods of mass flux, pressure, and wall temperature are usually small, and the oscillations of mass flow rate and pressure are in phase [171].

#### **6.5.1.2 PRESSURE-DROP TYPE OSCILLATIONS**

Pressure drop type oscillations occur when significant amount of compressible volume exists in the flow boiling two-phase system [165]. Such compressible volume can be produced if the flow channel has a long aspect ratio (e.g.,  $L/d > 150$ ) under low

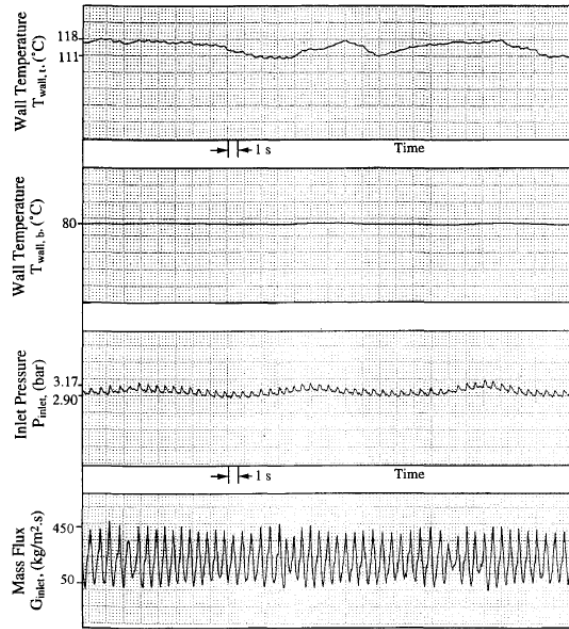


**Figure 6. 15.** Density wave type oscillations [171].

mass flux and/or high heat flux conditions [174], or if a surging tank or an accumulator is installed upstream of the boiling channel [171, 175-177]. The compressible volume serves as the buffer zone when there is an imbalance in the internal and external mass flux vs. pressure drop characteristics, which induces long-period, large-amplitude oscillations of pressure, mass flux and wall temperatures. Generally, the fluctuations of mass flow rate and pressure are out of phase, as shown in Figure 6. 16 [171] [178].

### 6.5.1.3 THERMAL OSCILLATIONS

Thermal oscillations are dynamic instabilities related to the instability of the liquid film next to the tube wall. The flow usually oscillates between annular flow, transition boiling and droplet flow, and is characterized by large-amplitude fluctuations in the wall temperature. The periods of and amplitudes of pressure and mass flux

fluctuations for this instability are very small. Density-wave oscillations are required to trigger the thermal oscillations.

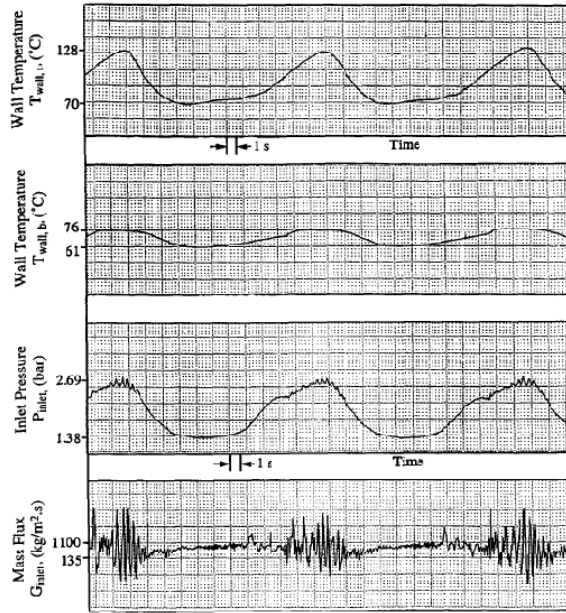


**Figure 6. 16.** Pressure-drop type oscillations [171].

In practical applications, the three major dynamic instabilities are generally distinct from each other without overlap. The boundaries between different type of oscillations are shown as the dash lines in [171]. Pressure drop type oscillations usually start first when there is an appreciable amount of compressible volume upstream in the flow loop or if the aspect ratio of the boiling channel is large. As the mass flux is reduced, the pressure in the channel increases to compress the vapor phase. Density-wave oscillations then occur when the compressible volume diminishes. At last, thermal oscillations start as the operating point moves further to the leftmost side of Figure 6. 17.

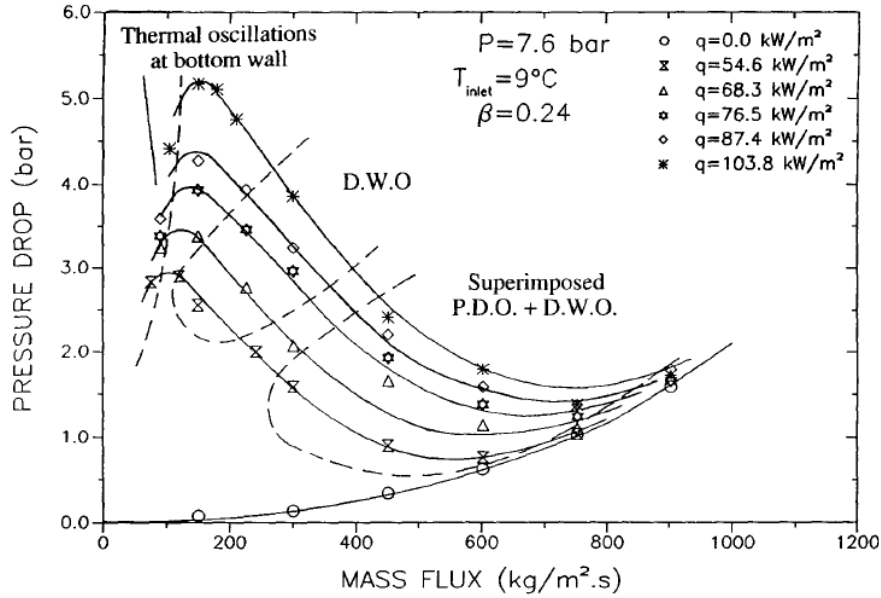


**Figure 6. 17.** Oscillation boundaries (D.W.O. refers to density-wave oscillations, P.D.O. refers to pressure-drop oscillations) [171].

### 6.5.2 TWO-PHASE FLOW INSTABILITY

Experiments were conducted to investigate the two-phase flow instabilities of water and nanofluids in flowing boiling through a minichannel, following the test procedures described earlier. The applied heat flux was fixed at  $29.9 \text{ W/cm}^2$  in all experiments.

Figure 6. 18 shows the time dependence of various two-phase flow parameters of water at the initial high mass flux condition ( $G = 2038.7 \text{ kg/m}^2\text{s}$ ), where the two-phase system operates in the single-phase region (i.e., the top right part of the flow characteristics curve with a positive slope in Figure 6. 25). The fluctuations in the flow parameters are merely random noises with no detectable amplitude and period. When the mass flux decreases to  $G = 1054.4 \text{ kg/m}^2\text{s}$ , two-phase flow oscillations started in which all flow parameters demonstrate clear peak-valley periodic cycles, as depicted in Figure

6.19. It shows that the oscillations of the inlet pressure and the mass flux are out of phase (the phase angle is  $\sim 180^\circ$ ), and the oscillation period is rather long,  $\sim 6$ -7 seconds, as compared to the time needed for the fluid to pass through the test tube ( $t = 0.28$ s). These are the typical features of pressure-drop type oscillations. It is not surprising since intrinsic conditions to trigger pressure-drop oscillations exist in the two-phase flow system. First, the test channel has a large aspect ratio of  $L/D = 281$ , which exceeds the threshold value for a "long tube" ( $L/D \sim 150$ ), so that the vapor phase generated during boiling provides sufficient amount of compressible volume. Second, the preheater located upstream to the test channel serves as a surge tank that modulates the internal and external pressure drop vs. mass flux characteristics.

The measurements of two-phase flow instability for nanofluids are shown in Figure 6. 20 to Figure 6. 23. As compared to the results for water, the oscillation amplitudes are smaller, and the periods are less distinguishable even in the low mass flux case where pressure-drop oscillations were supposed to dominate. In other word, two-phase flow oscillations seem to be suppressed in nanofluids, and the extent of suppression increases as the nanoparticle concentration increases from 0.01 v% to 0.1 v%.

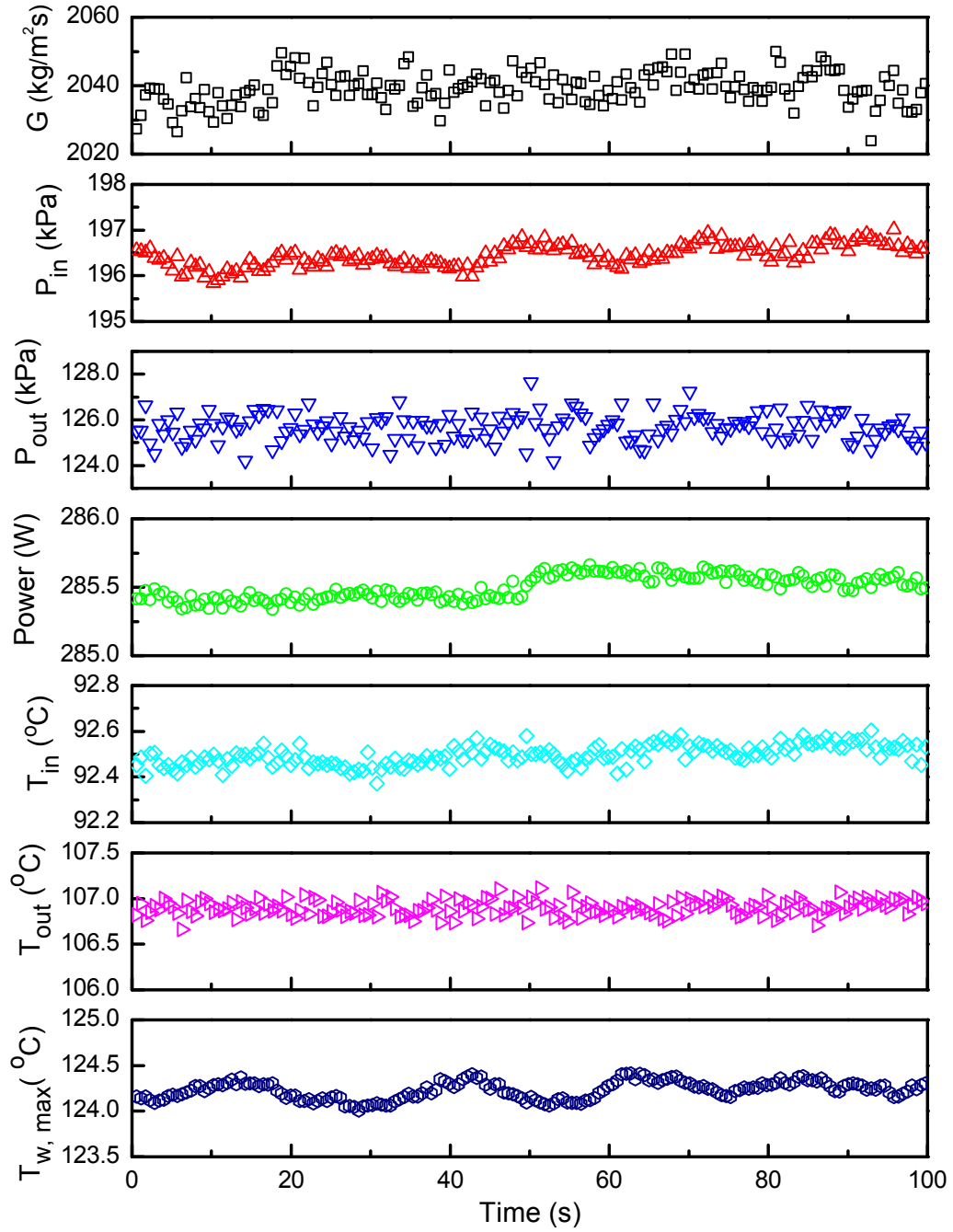


**Figure 6. 18.** Different parameters of water variation with time at  $G = 2038.7 \text{ kg/m}^2\text{s}$ ,  
 $T_{in} = 92.3 \text{ }^\circ\text{C}$ ,  $q''=29.9 \text{ W/cm}^2$  (stable region).

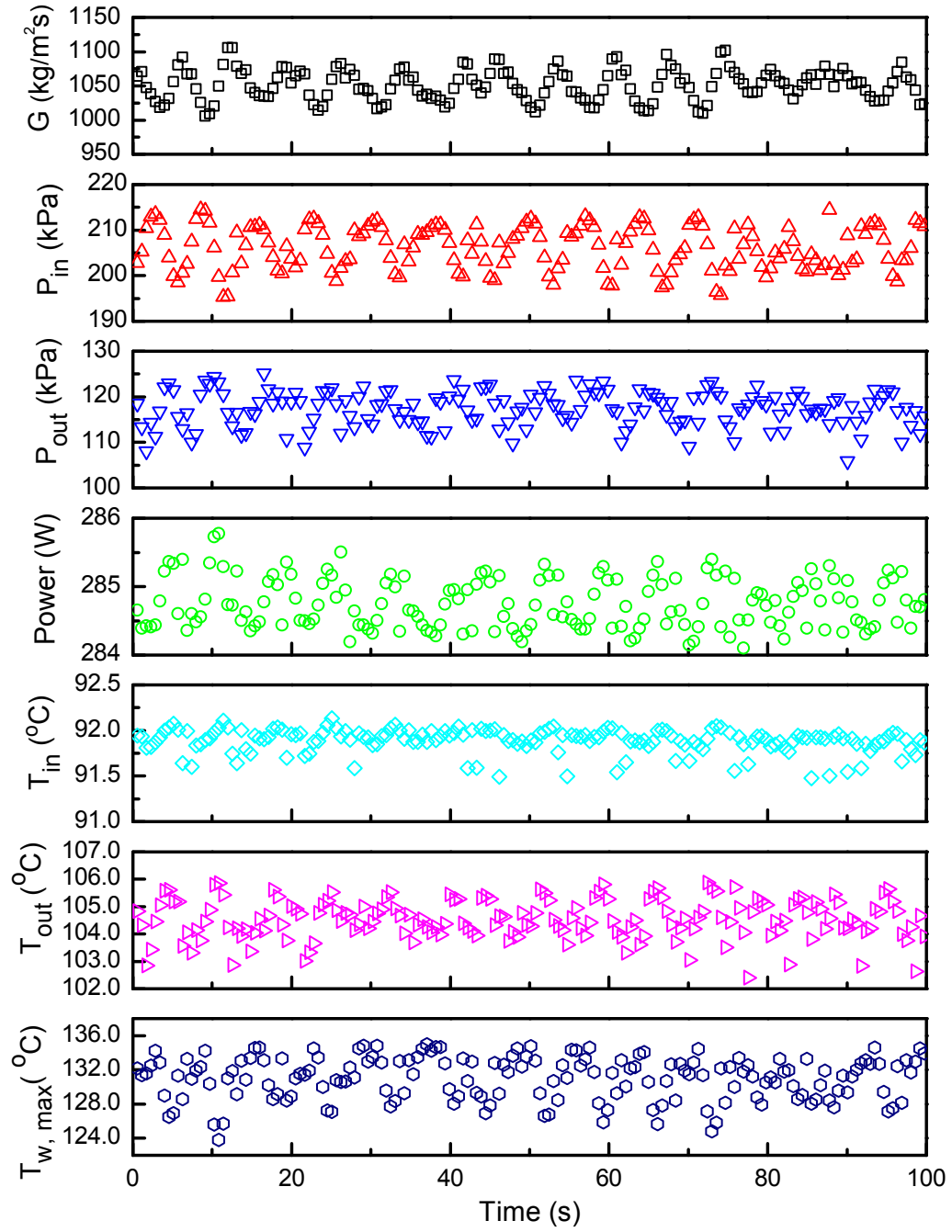


**Figure 6. 19.** Pressure-drop type oscillations of water at  $G = 1054.4 \text{ kg/m}^2\text{s}$ ,  $T_{in}=91.9 \text{ }^{\circ}\text{C}$ ,  $q''=29.9 \text{ W/cm}^2$ .

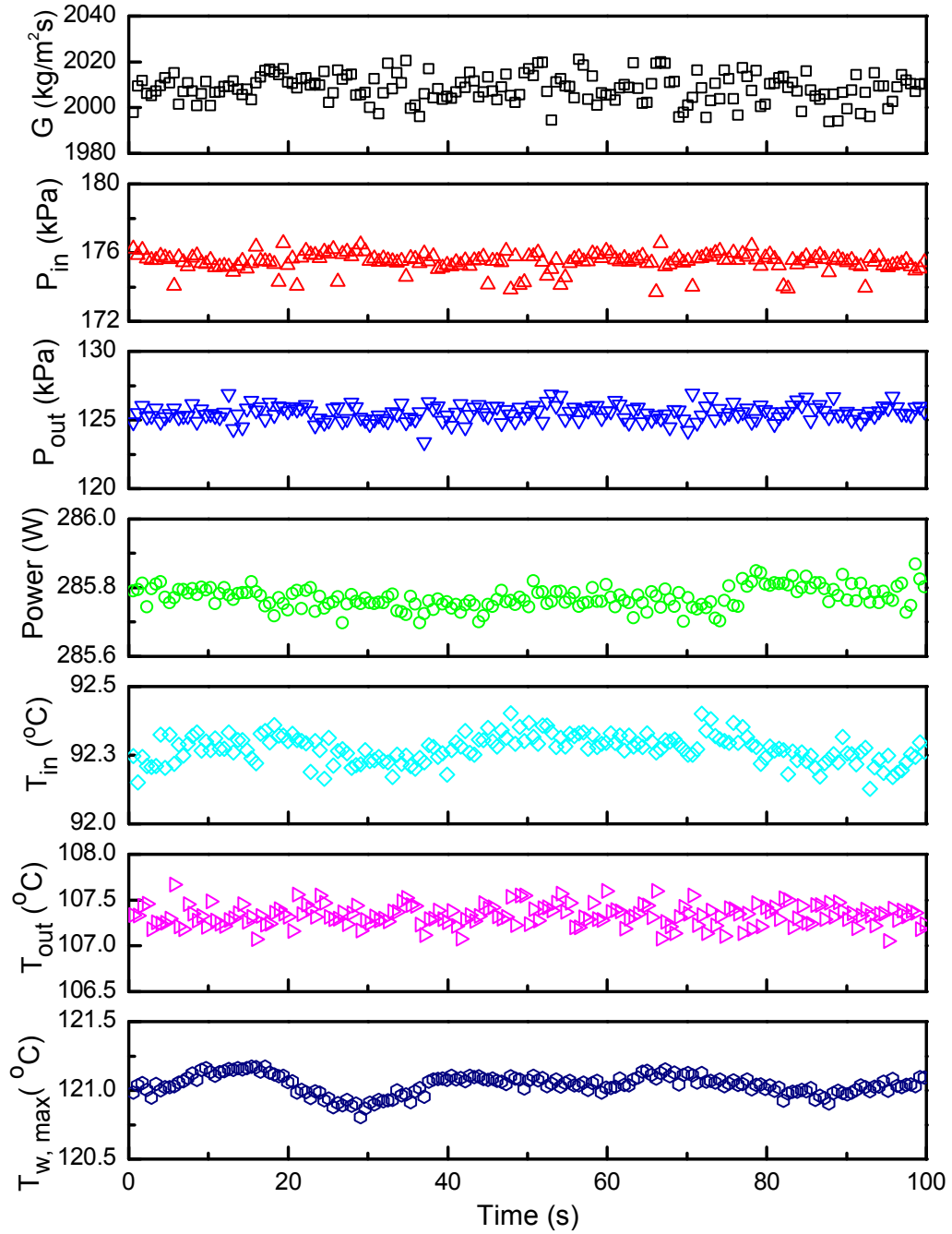


**Figure 6. 20.** Different parameters of 0.01 v% nanofluids variation with time at  $G = 2007.4 \text{ kg/m}^2\text{s}$ ,  $T_{in} = 92.3^\circ\text{C}$ ,  $q''=29.9 \text{ W/cm}^2$  (stable region).

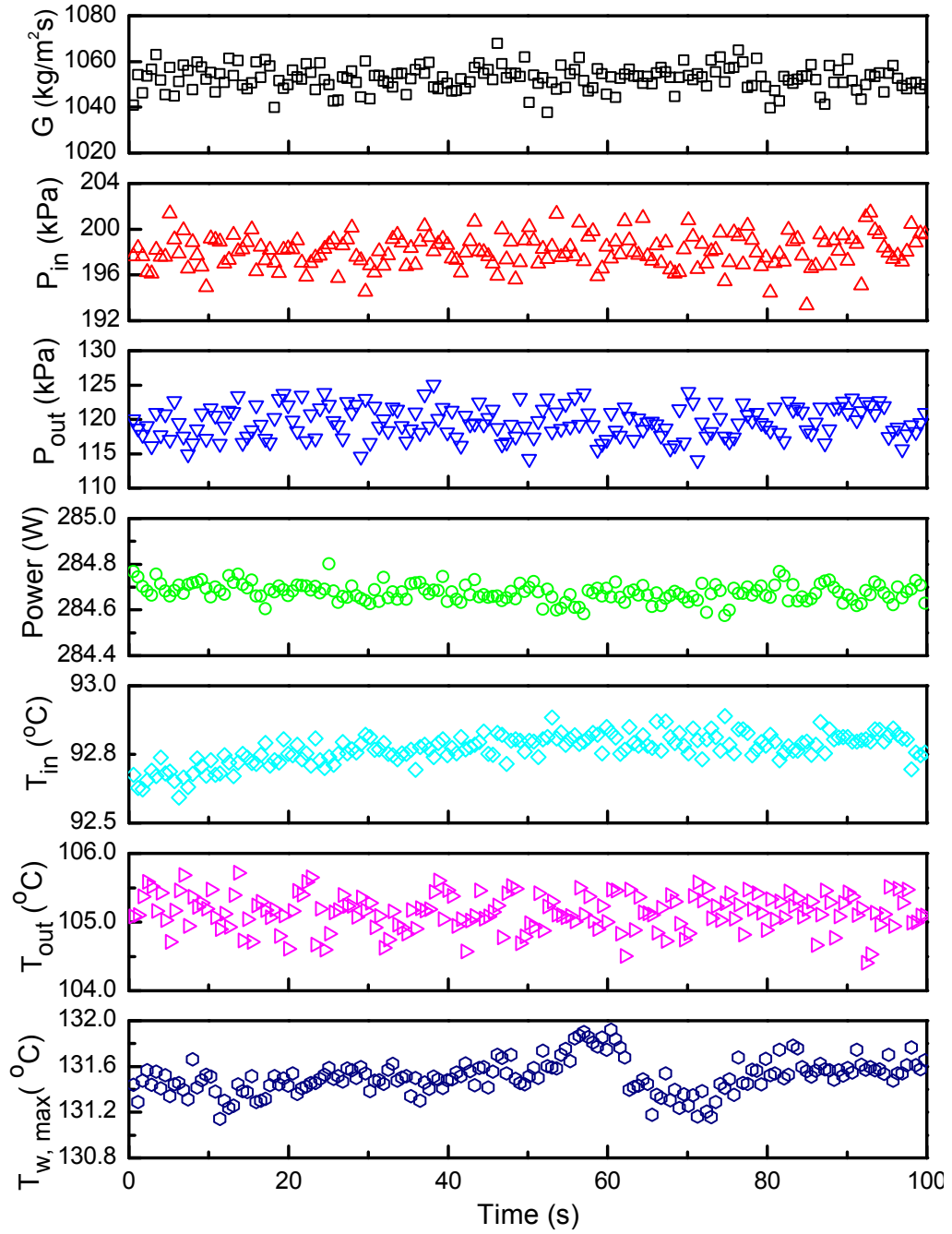


**Figure 6. 21.** Two-phase flow oscillations of 0.01 v% nanofluids at  $G = 1052.4 \text{ kg/m}^2\text{s}$ ,  $T_{in} = 92.7^\circ\text{C}$ ,  $q'' = 29.9 \text{ W/cm}^2$ .

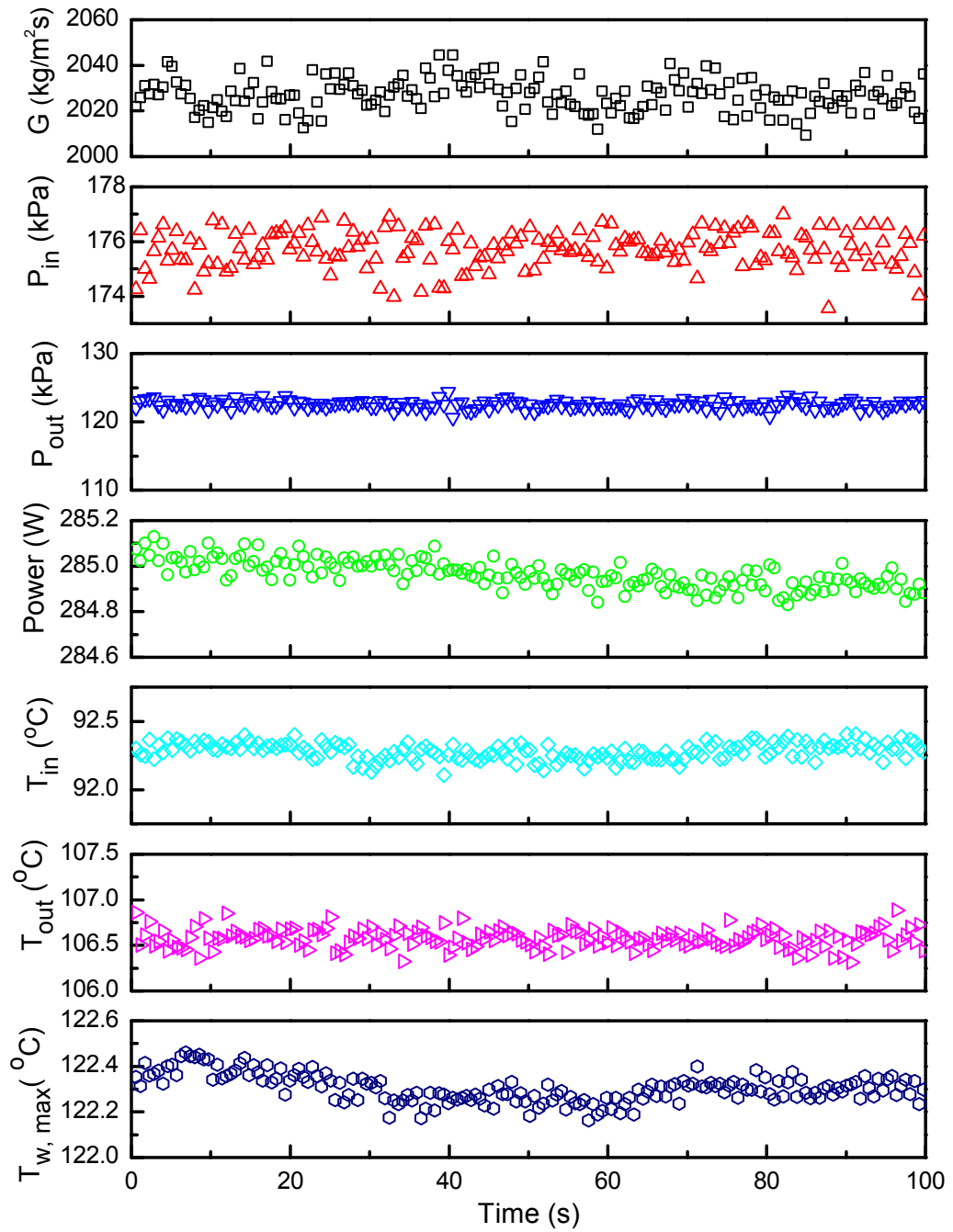


**Figure 6. 22.** Different parameters of 0.1 v% nanofluids variation with time at  $G = 2028.5 \text{ kg/m}^2\text{s}$ ,  $T_{in}=92.3^\circ\text{C}$ ,  $q''=29.9 \text{ W/cm}^2$  (stable region).

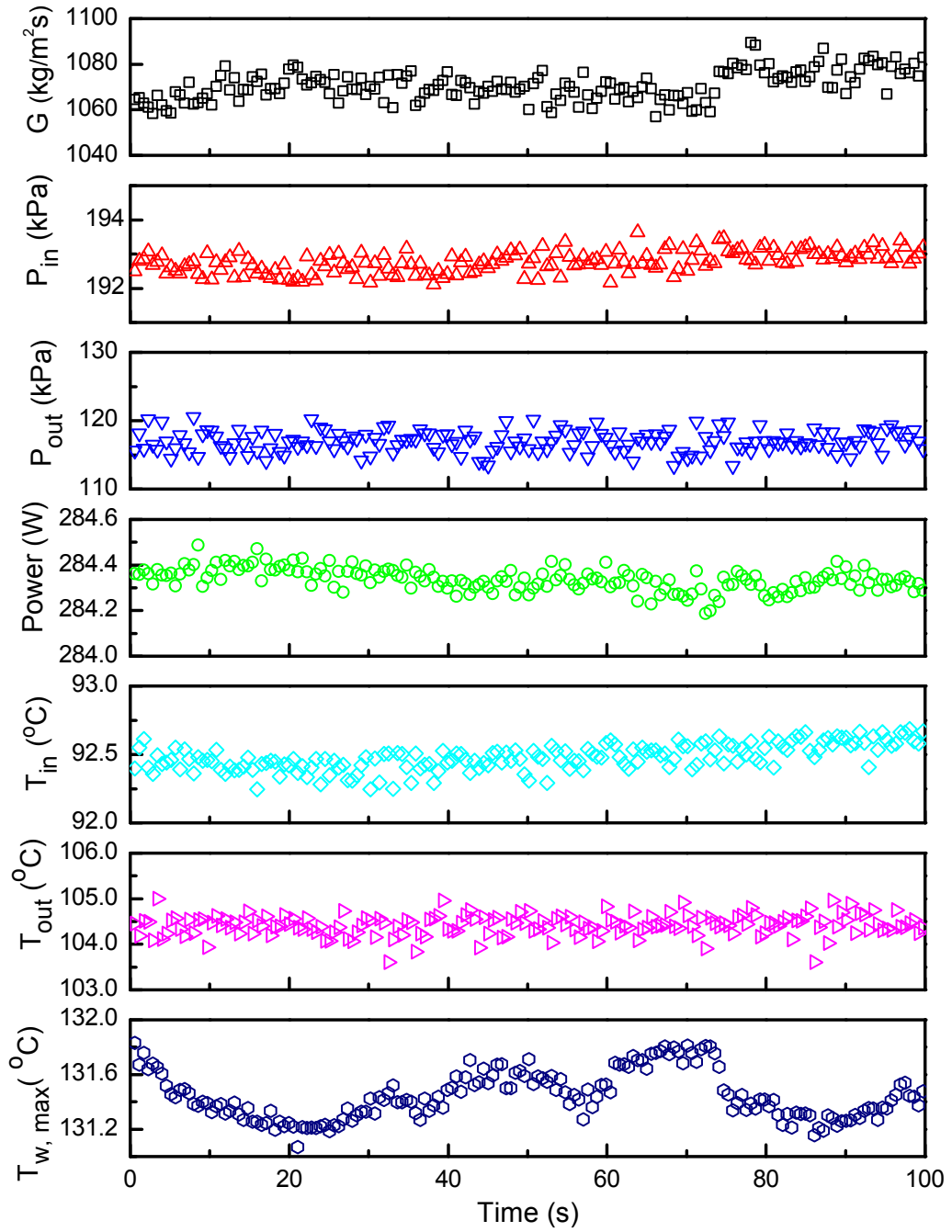


**Figure 6. 23.** Two-phase flow oscillations of 0.1 v% nanofluids at  $G = 1065.9 \text{ kg/m}^2\text{s}$ ,  
 $T_{in} = 92.5^\circ\text{C}$ ,  $q'' = 29.9 \text{ W/cm}^2$ .

The suppression of two-phase flow instability in nanofluids can be better illustrated in Figure 6. 24, which shows the instantaneous measurements of pressure drop and mass flux over a period of 85seconds. An elliptical limit loop can be clearly observed in the data for water, indicating a well-defined oscillatory behavior of the pressure-drop type instability. Particularly, the pressure drop varies between 74.8 kPa to 102.4 kPa and the mass flux between 1005.8 kg/m<sup>2</sup>s and 1105.9 kg/m<sup>2</sup>s (the set mass flux is 1065.9 kg/m<sup>2</sup>s). In contrast, the data points for nanofluids of both concentrations are clustered together with little scattering.

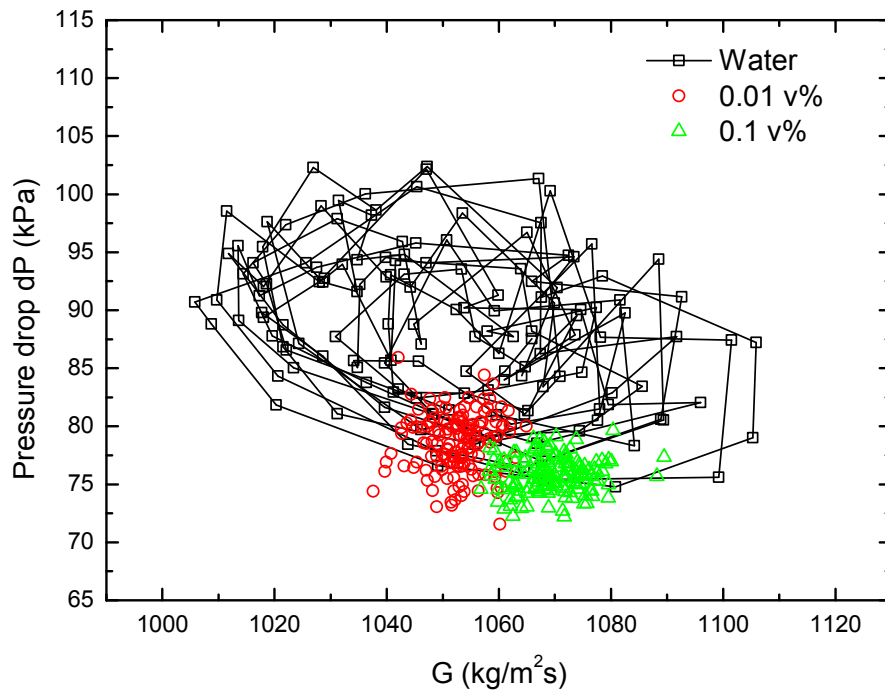
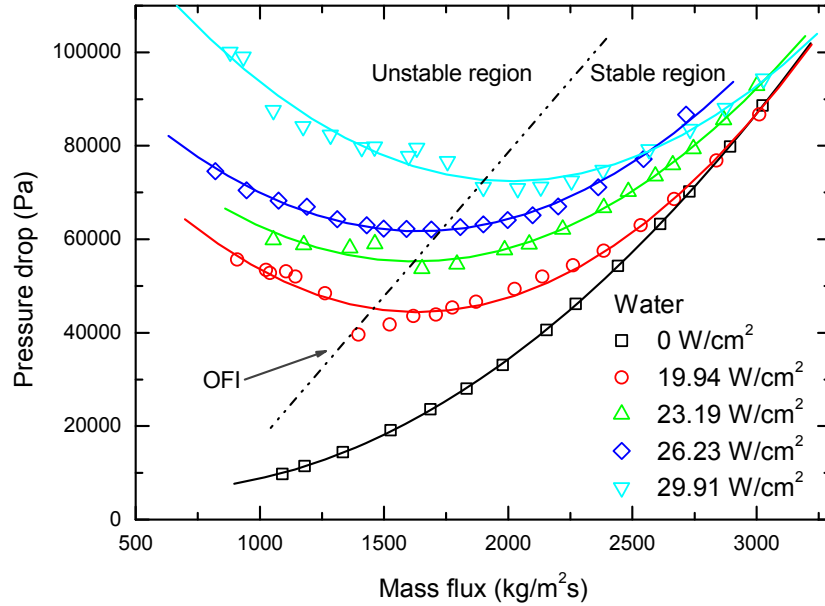


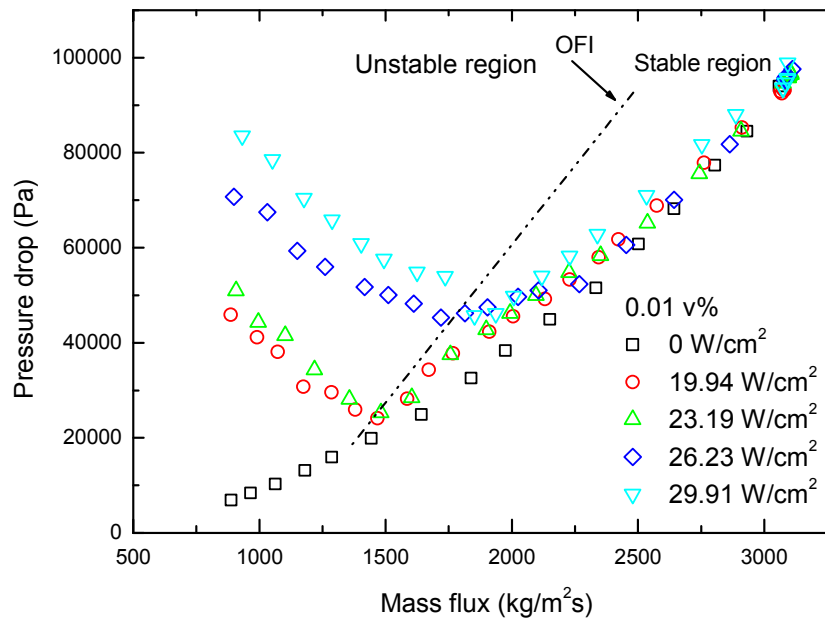
**Figure 6. 24.** Two-phase flow oscillations at  $G = 1065.9 \text{ kg/m}^2\text{s}$ ,  
 $T_{in} = 91.9 \text{ }^\circ\text{C}-92.5 \text{ }^\circ\text{C}$ ,  $q'' = 29.9 \text{ W/cm}^2$ .

Two-phase flow instabilities associated with flow boiling heat transfer were also studied under different heat fluxes. The two-phase pressure drop vs. mass flux plot for water is shown in Figure 6. 25. It follows the behavior of the internal characteristics illustrated in Figure 6. 17. The flow starts off as single-phase liquid, and the pressure drop gradually decreases as the mass flux reduces. This trend persists even after boiling occurs (which is evidenced by the deviation from the zero-heat-flux data line). The flow remains stable until further decreasing mass flux causes the pressure drop to rebound quickly due to intensified vaporization in the test tube. After that, the slope of the internal characteristics changes from positive to negative and flow oscillations are observed. When the heat flux is increased, Figure 6. 25(a) shows the transition from stable two-phase flow to unstable two-phase flow will occur at higher threshold values of mass flux. For example, the threshold mass flux is about  $1500 \text{ kg/m}^2\text{s}$  at  $q'' = 19.9 \text{ W/cm}^2$  but increases to  $1800 \text{ kg/m}^2\text{s}$  at  $q'' = 29.9 \text{ W/cm}^2$ . A transition boundary can thus be determined in Figure 6. 25 (a) by connecting all the transition points, which indicates the onset of flow instabilities (OFI). Accordingly, the region to the left of the OFI boundary is unstable, and the region to its right is stable. Similar plots for nanofluids are presented in Figure 6. 25 (b) and (c). It is noted that, as the nanoparticle concentration increases, the OFI transition line draws closer to the single-phase characteristics line and, consequently, the stable region bounded by these two lines diminishes; however, the threshold mass flux decreases considerably for all heat fluxes. This means the nanofluid flow can remain in the stable region even at much lower mass flux than water, but once the OFI occurs, the flow oscillations in nanofluids will happen more abruptly, e.g., Figure

6. 25(c) almost suggests that two-phase flow of 0.1 v% nanofluid will jump directly from the stable single-phase region to the unstable two-phase region.



(a)



(b)

**Figure 6. 25.** Two-phase flow characteristics under different heat fluxes: (a) water, (b) 0.01 v% nanofluid, and (c) 0.1 v% nanofluid.

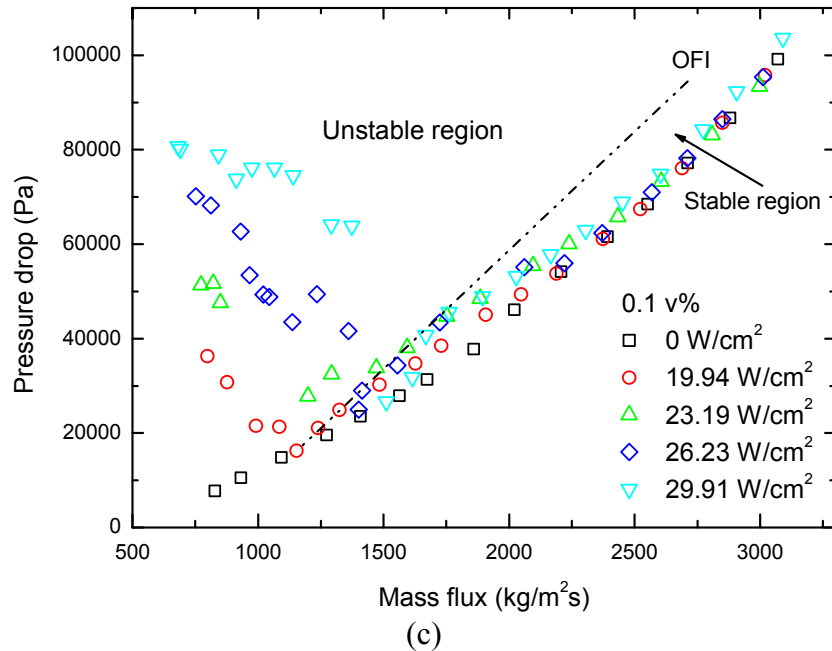


**Figure 6.25.** Two-phase flow characteristics under different heat fluxes: (a) water, (b) 0.01 v% nanofluid, and (c) 0.1 v% nanofluid [continued].

Figure 6. 26 compares the internal pressure drop vs. mass flux characteristics for water and nanofluids under different heat fluxes. All the aforementioned features can be clearly observed again, including the stable/unstable regions and the increasing threshold mass flux for OFI at higher heat flux, etc. More importantly, Figure 6. 26 shows the use of nanofluids delays the OFI, i.e., the threshold mass flux for OFI shifts towards lower values as the nanoparticle concentration increases. The mechanism responsible for the delayed OFI in nanofluids is possibly related to the delayed ONB. As discussed earlier, deposition of nanoparticles on the channel inner surface delays ONB by diminishing the number of available cavities and narrowing down the size range of active nucleation sites, which results in less vapor volume to be generated. Since pressure-drop type oscillations dominates the early stage of two-phase instability, reduced compressibility in the test

tube will certainly help suppress the flow instabilities. However, due to energy conservation, abrupt nucleation usually follows the delayed ONB where the excess thermal energy will eventually be converted to latent heat of the vapor phase. This explains the sudden transition of nanofluid two-phase flow from the stable region to the unstable region once the ONB occurs.

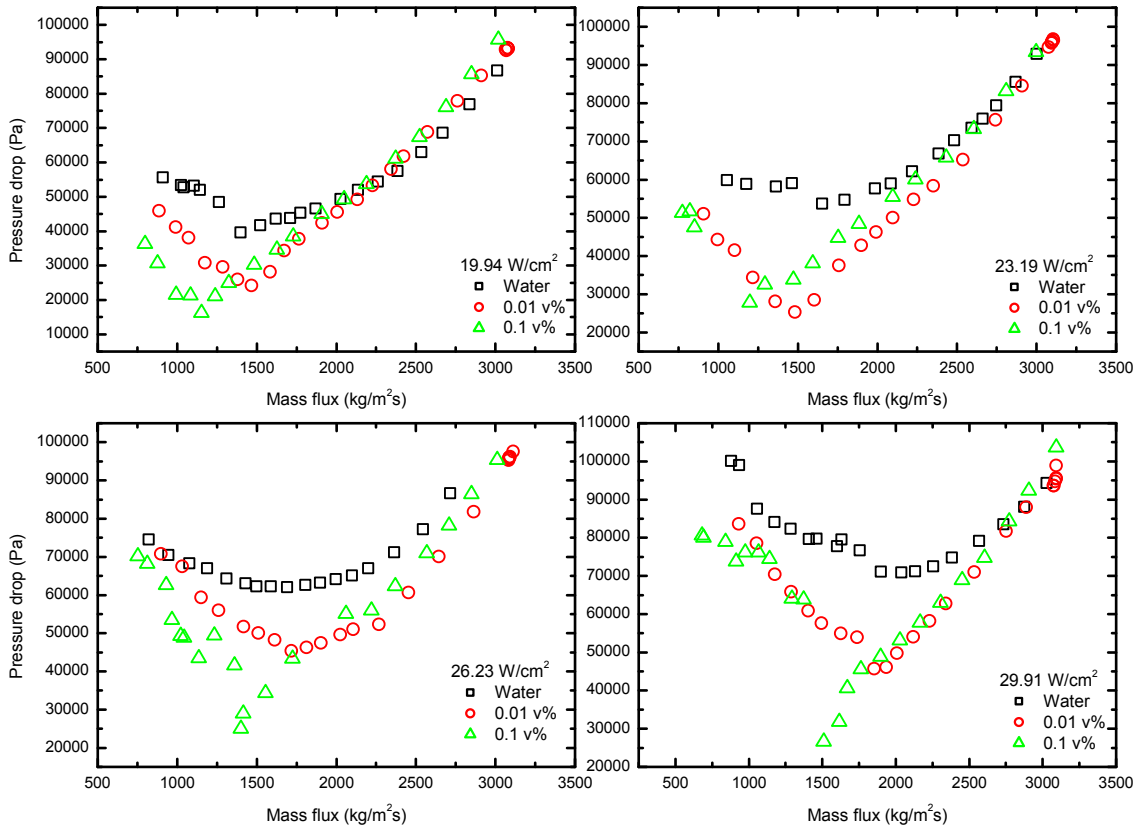


**Figure 6. 26.** Comparison of two phase flow characteristics between water and nanofluids under different heat flux.

## 6.6 SUMMARY

Forced convective flow boiling and two-phase flow of nanofluids in a minichannel were studied experimentally with an emphasis on the effect of the

nanoparticle deposition on two-phase flow instabilities. It was found that addition of nanoparticles into the base fluid delays the ONB and suppresses the OFI, and the extent of delay/suppression is related to the nanoparticle concentration. These effects were attributed to the wettability change due to nanoparticle deposition on the heating surface as well as the thinning of thermal boundary layer. An analytical model was developed to understand the delayed ONB in nanofluids. It was also demonstrated that in nanofluids the pressure-drop type flow instabilities prevail, and the oscillation amplitudes of pressure, temperature and mass flux are reduced.

## CHAPTER 7. CONCLUSIONS AND FUTURE WORK

Thermal transport during flow of nanofluids in a minichannel was investigated to explore the fundamentals of thermophysical properties, single-phase and two-phase flow characteristics and heat transfer. Major accomplishments from this study as well as recommendations for future research work are summarized as follows.

### **Single-phase transport of nanofluids**

- 1) Experimental investigations were conducted to study the single-phase convective heat transfer of both  $\text{Al}_2\text{O}_3$ -water and  $\text{Al}_2\text{O}_3$ -PAO nanofluids in a circular minichannel. In the laminar region, these nanofluids exhibited pronounced entrance region behavior. The convective heat transfer of nanofluids is enhanced in the laminar flow with the penalty of increased pressure drop. The increments in both heat transfer and pressure drop are proportional to the nanoparticle volume concentration.
- 2) The critical  $\text{Re}$  at which the onset of transition to turbulence occurs is delayed in nanofluids, due to the particle-fluid interaction, which damps the instabilities in the flow. The suppression of turbulence is alleviated as the flow becomes fully developed turbulent.
- 3) Established conventional correlations cannot fully predict the single-phase pressure drop and heat transfer of nanofluids, particularly in the transition and turbulent regions for aqueous nanofluids, as well as PAO nanofluids containing nanorods.

- 4) Nanofluids should be used in either the laminar flow or the fully developed turbulent flow with sufficiently high  $Re$  in order to yield enhanced heat transfer performance for engineering applications.

### **Thermal performance of nanofluids**

- 1) The study of the thermal effectiveness of  $Al_2O_3$ -water and  $Al_2O_3$ -PAO nanofluids was experimentally conducted in laminar forced convection. The effective thermophysical properties play an important role in the thermal performance of nanofluids. While the enhancement in thermal conductivity helps to improve convective heat transfer, while the higher viscosity necessitates more pumping power to enable the cooling, and the reduced specific heat adds to the caloric thermal resistance that hampers the heat to be transported out of the system.
- 2) Convective thermal performance of nanofluids depends on the constraints that are imposed on the flow, i.e., constant  $Re$ , constant  $Q$ , or constant  $P$ . Nanofluids can enhance heat transfer coefficients, however, from the overall thermal effectiveness for cooling applications, no difference in thermal performance can be found between the nanofluids and the base fluid when the cooling application is constrained by the constant pumping power condition.

### **Flow boiling of nanofluids**

- 1) Flow boiling of nanofluids in a minichannel was studied. Boiling curves and ONB for nanofluids were obtained. Optical image measurement for contact angles for various concentration nanofluids on a fresh stainless steel surface was conducted. Addition of nanoparticles into the base fluid can effectively delay ONB for nanofluids. An analytical model incorporating contact angles, as well as

other possible reasons were presented to explain the possible mechanisms for ONB delay.

- 2) Pressure drop oscillation type instability of nanofluids in minichannel was investigated. The fluid and minichannel wall temperatures, as well as pressure drop across the channel were measured. In two-phase flow, flow characteristics of nanofluids with different concentrations were compared with base fluid. Nanofluids can effectively delay OFI, as well as reduction of two-phase fluctuations. Possible reasons were given to explain the possible mechanisms for OFI delay.

### **Future Work**

The major research tasks for future work are outlined as follows.

- 1) Develop a numerical scheme to fully track nanoparticles migration in the channel flow, and the interaction with the surrounding fluid.
- 2) Perform detailed flow visualization with high speed photography technology to explore ONB and bubble dynamics in flow boiling for nanofluids.
- 3) Explore the analytical and numerical model for flow boiling instability in channel flow for nanofluids.
- 4) Carry out experimental investigation of nanofluids containing metal particles, for instance, copper, aluminum, and gold.

## REFERENCES

1. Choi, S.U.S., Zhang, Z. G., Keblinski, P., *Nanofluids*, in *Encyclopedia of Nanoscience and Nanotechnology*, H.S. Nalwa, Editor. 2004, American Scientific Pub: Los Angeles.
2. Eastman, J.A., Phillpot, S. R., Choi, S. U. S., Keblinski, P., *Thermal transport in nanofluids*. Annual Review of Materials Research, 2004. **34**: p. 219-246.
3. Keblinski, P., J.A. Eastman, and D.G. Cahill, *Nanofluids for thermal transport*. Materials Today, 2005. **8**(6): p. 36-44.
4. Das, S.K., S.U.S. Choi, and H.E. Patel, *Heat transfer in Nanofluids - A review*. Heat Transfer Engineering, 2006. **27**(10): p. 3-19.
5. Yu, W., France, D. M., Routbort, J. L., Choi, S. U. S., *Review and comparison of nanofluid thermal conductivity and heat transfer enhancements*. Heat Transfer Engineering, 2008. **29**(5): p. 432-460.
6. Cheng, L., E.P. Bandarra Filho, and J.R. Thome, *Nanofluid Two-Phase Flow and Thermal Physics: A New Research Frontier of Nanotechnology and Its Challenges*. Journal of Nanoscience and Nanotechnology, 2008. **8**(7): p. 3315-3332.
7. Yu, W., France, D. M., Timofeev, E. V., Singh, D., Routbort, J. L., *Thermophysical property-related comparison criteria for nanofluid heat transfer enhancement in turbulent flow*. Applied Physics Letters, 2010. **96**(21).
8. Choi, S.U.S. *Enhancing thermal conductivity of fluids with nanoparticles*. in *1995 ASME International Mechanical Engineering Congress and Exposition*. 1995. San Francisco.

9. Yatsuya, S., Tsukasaki, Y., Mihama, K., Uyeda, R., *Preparation of extremely fine particles by vacuum evaporation onto a running oil substrate*. Journal of Crystal Growth, 1978. **45**(0): p. 490-494.
10. Eastman, J.A., Choi, S. U. S., Li, S., Yu, W., Thompson, L. J., *Anomalously increased effective thermal conductivities of ethylene glycol-based nanofluids containing copper nanoparticles*. Applied Physics Letters, 2001. **78**(6): p. 718-720.
11. Chang, H., Tsng, T. T., Yang, Y. C., Chen, L. C., Lin, H. M., Lin, C. K., Jwo, C. S., *Nanoparticle suspension preparation using the arc spray nanoparticle synthesis system combined with ultrasonic vibration and rotating electrode*. The International Journal of Advanced Manufacturing Technology, 2005. **26**(5): p. 552-558.
12. Zhu, H.-t., Y.-s. Lin, and Y.-s. Yin, *A novel one-step chemical method for preparation of copper nanofluids*. Journal of Colloid and Interface Science, 2004. **277**(1): p. 100-103.
13. Lee, S., Choi, S. U. S., Li, S., Eastman, J. A. , *Measuring Thermal Conductivity of Fluids Containing Oxide Nanoparticles*. Journal of Heat Transfer, 1999. **121**(2): p. 280-289.
14. Granqvist, C.G. and R.A. Buhrman, *Ultrafine metal particles*. Journal of Applied Physics, 1976. **47**(5): p. 2200-2219.
15. Srdić, V.V., Winterer, Markus, Moller, Andreas, Mieke, G., Hahn, Horst, *Nanocrystalline Zirconia Surface-Doped with Alumina: Chemical Vapor*

- Synthesis, Characterization, and Properties*. Journal of the American Ceramic Society, 2001. **84**(12): p. 2771-2776.
16. Sugimoto, T., *Fine particles: Synthesis, characterization and mechanism of growth*. Surfactant Science. Vol. 92. 2000, New York, NY: CRC Press.
  17. Mapkar, J.A., G. Iyer, and M.R. Coleman, *Functionalization of carbon nanofibers with elastomeric block copolymer using carbodiimide chemistry*. Applied Surface Science, 2009. **255**(9): p. 4806-4813.
  18. Batchelor, G.K., *The effect of Brownian motion on the bulk stress in a suspension of spherical particles*. Journal of Fluid Mechanics, 1977. **83**(01): p. 97-117.
  19. Einstein, A., *A New Determination of Molecular Dimensions*. Annalen der Physik, 1906. **4**(19): p. 17.
  20. Batchelor, G.K., *The effect of Brownian motion on the bulk stress in a suspension of spherical particles*. Journal of Fluid Mechanics, 1977. **83**: p. 97-117
  21. Helvaci, S.M.P.a.S.S., *Solid and Liquid Two Phase Flow*. 2008, Amsterdam, Netherlands: Elsevier.
  22. Wierenga, A.M. and A.P. Philipse, *Low-shear viscosity of isotropic dispersions of (Brownian) rods and fibres; a review of theory and experiments*. Colloids and Surfaces a-Physicochemical and Engineering Aspects, 1998. **137**(1-3): p. 355-372.
  23. Onsager, L., *Viscosity and particle shape in colloid solutions*. Physical Review, 1932. **40**.
  24. Kuhn, w. and K. H, *Die Abhängigkeit der Viskosität vom Stromungsgefälle bei hochverdünnnten Suspensionen und Lösungen*. Helv. Chim. Acta, 1945. **28**: p. 30.

25. Hinch, E.J. and L.G. Leal, *EFFECT OF BROWNIAN MOTION ON RHEOLOGICAL PROPERTIES OF A SUSPENSION OF NON-SPHERICAL PARTICLES*. Journal of Fluid Mechanics, 1972. **52**(APR25): p. 683-&.
26. Berry, D.H. and W.B. Russel, *THE RHEOLOGY OF DILUTE SUSPENSIONS OF SLENDER RODS IN WEAK FLOWS*. Journal of Fluid Mechanics, 1987. **180**: p. 475-494.
27. Krieger, I.M., *Rheology of monodisperse lattices*. Advances in Colloid and Interface Science, 1972. **3**(2): p. 25.
28. Philipse, A.P., *The random contact equation and its implications for (colloidal) rods in packings, suspensions, and anisotropic powders (vol 12, pg 1127, 1996)*. Langmuir, 1996. **12**(24): p. 5971-5971.
29. Philipse, A.P. and A. Verberkmoes, *Statistical geometry of caging effects in random thin-rod structures*. Physica a-Statistical Mechanics and Its Applications, 1997. **235**(1-2): p. 186-193.
30. Chen, H, Ding, Y., He, Y., Tan C., *Rheological behaviour of ethylene glycol-titanate nanotube nanofluids*. Journal of Nanoparticle Research, 2009. **11**(6): p. 1513-1520.
31. Chen, H., Y.L. Ding, and A. Lapkin, *Rheological behaviour of nanofluids containing tube rod-like nanoparticles*. Powder Technology, 2009. **194**(1-2): p. 132-141.
32. Chen, H., Yang, W., He, Y., Ding Y., Zhang, L., Tan, C., Lapkin, A., Bavykin, D., *Heat transfer and flow behaviour of aqueous suspensions of titanate nanotubes (nanofluids)*. Powder Technology, 2008. **183**(1): p. 63-72.

33. Zhou, S.-Q., R. Ni, and D. Funfschilling, *Effects of shear rate and temperature on viscosity of alumina polyalphaolefins nanofluids*. Journal of Applied Physics, 2010. **107**(5): p. 054317-6.
34. R. L. Hamilton, O.K.C., *IEC Fundamentals 2*. 1962. 187.
35. Nan, C.W., Birringer, R., Clarke, D. R., Gleiter, H., *Effective thermal conductivity of particulate composites with interfacial thermal resistance*. Journal of Applied Physics, 1997. **81**(10): p. 6692-6699.
36. Jaeger, H.S.C.a.J.C., *Conduction of Heat in Solids*. 1959, New York: Oxford University Press Inc.
37. Williams, W., J. Buongiorno, and L.-W. Hu, *Experimental Investigation of Turbulent Convective Heat Transfer and Pressure Loss of Alumina/Water and Zirconia/Water Nanoparticle Colloids (Nanofluids) in Horizontal Tubes*. Journal of Heat Transfer, 2008. **130**(4): p. 042412-7.
38. Pak, B.C. and Y.I. Cho, *Hydrodynamic and heat transfer study of dispersed fluids with submicron metallic oxide particles*. Experimental Heat Transfer, 1998. **11**(2): p. 151-170.
39. Anoop, K.B., T. Sundararajan, and S.K. Das, *Effect of particle size on the convective heat transfer in nanofluid in the developing region*. International Journal of Heat and Mass Transfer, 2009. **52**(9-10): p. 2189-2195.
40. Nan, C.W., Z. Shi, and Y. Lin, *A simple model for thermal conductivity of carbon nanotube-based composites*. Chemical Physics Letters, 2003. **375**(5-6): p. 666-669.

41. Bart, G.C.J., *Thermal conduction in nonhomogeneous and phase change media*. 1994, Delft university of Technology, Netherlands.
42. Carson, J.K., Lovatt, S. J., Tanner, D. J., Cleland, A. C., *Thermal conductivity bounds for isotropic, porous materials*. International Journal of Heat and Mass Transfer, 2005. **48**(11): p. 2150-2158.
43. Hashin, Z. and S. Shtrikman, *A Variational Approach to the Theory of the Effective Magnetic Permeability of Multiphase Materials*. Journal of Applied Physics, 1962. **33**(10): p. 3125-3131.
44. Landauer, R., *The Electrical Resistance of Binary Metallic Mixtures*. Journal of Applied Physics, 1952. **23**(7): p. 779-784.
45. Kirkpatrick, S., *Percolatio and conduction*. Rev. Mo. Phys, 1973: p. 574-588.
46. Li, Q. and Y. Xuan, *Convective heat transfer and flow characteristics of Cu-water nanofluid*. Science in China Series E: Technological Sciences, 2002. **45**(4): p. 408-416.
47. Xuan, Y. and Q. Li, *Investigation on Convective Heat Transfer and Flow Features of Nanofluids*. Journal of Heat Transfer, 2003. **125**(1): p. 151-155.
48. Yang, Y., Zhang, Z. G., Grulke, E. A., Anderson, W. B., Wu, G. F., *Heat transfer properties of nanoparticle-in-fluid dispersions (nanofluids) in laminar flow*. International Journal of Heat and Mass Transfer, 2005. **48**(6): p. 1107-1116.
49. Wen, D. and Y. Ding, *Experimental investigation into convective heat transfer of nanofluids at the entrance region under laminar flow conditions*. International Journal of Heat and Mass Transfer, 2004. **47**(24): p. 5181-5188.

50. Ding, Y., Alias, H., Wen, D., Williams, R., *Heat transfer of aqueous suspensions of carbon nanotubes (CNT nanofluids)*. International Journal of Heat and Mass Transfer, 2006. **49**(1-2): p. 240-250.
51. He, Y., Jin, Y., Chen, H., Ding, Y., Cang, D., Lu, H., *Heat transfer and flow behaviour of aqueous suspensions of TiO<sub>2</sub> nanoparticles (nanofluids) flowing upward through a vertical pipe*. International Journal of Heat and Mass Transfer, 2007. **50**(11–12): p. 2272-2281.
52. Zeinali Heris, S., M. Nasr Esfahany, and S.G. Etemad, *Experimental investigation of convective heat transfer of Al<sub>2</sub>O<sub>3</sub>/water nanofluid in circular tube*. International Journal of Heat and Fluid Flow, 2007. **28**(2): p. 203-210.
53. Putra, N., W. Roetzel, and S. Das, *Natural convection of nano-fluids*. Heat and Mass Transfer, 2003. **39**(8): p. 775-784.
54. Duangthongsuk, W. and S. Wongwises, *Effect of thermophysical properties models on the predicting of the convective heat transfer coefficient for low concentration nanofluid*. International Communications in Heat and Mass Transfer, 2008. **35**(10): p. 1320-1326.
55. Wen, D. and Y. Ding, *Formulation of nanofluids for natural convective heat transfer applications*. International Journal of Heat and Fluid Flow, 2005. **26**(6): p. 855-864.
56. Nnanna, A.G.A., *Experimental Model of Temperature-Driven Nanofluid*. Journal of Heat Transfer, 2007. **129**(6): p. 697-704.

57. Khanafer, K., K. Vafai, and M. Lightstone, *Buoyancy-driven heat transfer enhancement in a two-dimensional enclosure utilizing nanofluids*. International Journal of Heat and Mass Transfer, 2003. **46**(19): p. 3639-3653.
58. Wen, D. and Y. Ding, *Effect of particle migration on heat transfer in suspensions of nanoparticles flowing through minichannels*. Microfluidics and Nanofluidics, 2005. **1**(2): p. 183-189.
59. Mansour, R.B., N. Galanis, and C.T. Nguyen, *Effect of uncertainties in physical properties on forced convection heat transfer with nanofluids*. Applied Thermal Engineering, 2007. **27**(1): p. 240-249.
60. Kim, J., Y.T. Kang, and C.K. Choi, *Analysis of convective instability and heat transfer characteristics of nanofluids*. Physics of Fluids, 2004. **16**(7): p. 2395-2401.
61. Hwang, K.S., J.-H. Lee, and S.P. Jang, *Buoyancy-driven heat transfer of water-based Al<sub>2</sub>O<sub>3</sub> nanofluids in a rectangular cavity*. International Journal of Heat and Mass Transfer, 2007. **50**(19–20): p. 4003-4010.
62. Jung, J.-Y., H.-S. Oh, and H.-Y. Kwak, *Forced convective heat transfer of nanofluids in microchannels*. International Journal of Heat and Mass Transfer, 2009. **52**(1–2): p. 466-472.
63. Santra, A.K., S. Sen, and N. Chakraborty, *Study of heat transfer augmentation in a differentially heated square cavity using copper–water nanofluid*. International Journal of Thermal Sciences, 2008. **47**(9): p. 1113-1122.

64. Abu-Nada, E., Z. Masoud, and A. Hijazi, *Natural convection heat transfer enhancement in horizontal concentric annuli using nanofluids*. International Communications in Heat and Mass Transfer, 2008. **35**(5): p. 657-665.
65. Maiga, S.E.B., Nguyen, C. T., Galanis, N., Roy, G., *Heat transfer behaviours of nanofluids in a uniformly heated tube*. Superlattices and Microstructures, 2004. **35**(3–6): p. 543-557.
66. Maiga, S.E.B., Palm, S. J., Nguyen, C. T., Roy, G., Galanis, *Heat transfer enhancement by using nanofluids in forced convection flows*. International Journal of Heat and Fluid Flow, 2005. **26**(4): p. 530-546.
67. S. E. B. Maiga, S.J.P., C. T. Nguyen, T. Roy and M. Coqueux, *Heat transfer enhancement in turbulent tube flow using Al<sub>2</sub>O<sub>3</sub> nanoparticle suspension*. International Journal of Numerical Methods for Heat & Fluid Flow, 2005. **16**(3): p. 275 - 292.
68. Shah, R.K., and London, A. L., *Laminar Flow Forced Convection in Ducts*. Adv. Heat Transfer. 1978: Academic Press.
69. AK Santra, S.S., N. Chakraborty, *Comparison of heat transfer augmentation in a square cavity using nanofluid following two different thermal conductivity models*. Journal of Energy Heat Mass Transfer, 2007. **29**: p. 289-310.
70. Hwang, K.S., S.P. Jang, and S.U.S. Choi, *Flow and convective heat transfer characteristics of water-based Al<sub>2</sub>O<sub>3</sub> nanofluids in fully developed laminar flow regime*. International Journal of Heat and Mass Transfer, 2009. **52**(1–2): p. 193-199.

71. Lai, W.Y., Vinod, S., Phelan, P. E., Prasher, R., *Convective Heat Transfer for Water-Based Alumina Nanofluids in a Single 1.02-mm Tube*. Journal of Heat Transfer, 2009. **131**(11): p. 112401-9.
72. P.Mills and P. Snabre, *Rheology and Structure of Concentrated Suspensions of Hard Spheres. Shear Induced Particle Migration*. J. Phys. II France, 1995. **5**(10): p. 1597-1608.
73. Sharma, K.V., L.S. Sundar, and P.K. Sarma, *Estimation of heat transfer coefficient and friction factor in the transition flow with low volume concentration of Al<sub>2</sub>O<sub>3</sub> nanofluid flowing in a circular tube and with twisted tape insert*. International Communications in Heat and Mass Transfer, 2009. **36**(5): p. 503-507.
74. Williams, W., J. Buongiorno, and L.W. Hu, *Experimental investigation of turbulent convective heat transfer and pressure loss of alumina/water and zirconia/water nanoparticle colloids (nanofluids) in horizontal tubes*. Journal of Heat Transfer-Transactions of the Asme, 2008. **130**(4).
75. Rea, U., McKrell, T., Hu, L., Buongiorno, J., *Laminar convective heat transfer and viscous pressure loss of alumina–water and zirconia–water nanofluids*. International Journal of Heat and Mass Transfer, 2009. **52**(7–8): p. 2042-2048.
76. Torii, S. and W.-J. Yang, *Heat Transfer Augmentation of Aqueous Suspensions of Nanodiamonds in Turbulent Pipe Flow*. Journal of Heat Transfer, 2009. **131**(4): p. 043203-5.
77. Duangthongsuk, W. and S. Wongwises, *An experimental study on the heat transfer performance and pressure drop of TiO<sub>2</sub>-water nanofluids flowing under*

- a turbulent flow regime*. International Journal of Heat and Mass Transfer, 2010. **53**(1–3): p. 334-344.
78. Xinyu, W., W. Huiying, and C. Ping, *Pressure drop and heat transfer of Al<sub>2</sub>O<sub>3</sub>-H<sub>2</sub>O nanofluids through silicon microchannels*. Journal of Micromechanics and Microengineering, 2009. **19**(10): p. 105020.
79. Liu, D. and S.V. Garimella, *Investigation of liquid flow in microchannels*. Journal of Thermophysics and Heat Transfer, 2004. **18**(1): p. 65-72.
80. Blevins, R.D., *Applied Fluid Dynamics Handbook*. 1992, Malabar, FL: Krieger.
81. Incropera, F., DeWitt, D. P., Bergman, T. L., and Lavine, A. S., *Fundamentals of Heat and Mass Transfer*. 6 ed. 2007: John Wiley & Sons.
82. Talyor, J.R., *An Introduction to Error Analysis*. 1997: University Science Books.
83. White, F.M., *Viscous Fluid Flow*. 1991, New York, NY: McGraw-Hill.
84. Stephan, K., and Preuber, P., *Warmeübergang und Maximale Warmestromdichte Beim Behaltersieden Binarer und Ternarer Flüssigkeitsgemische*. Chem. Ing. Tech., 1979(51).
85. Kakac, S., Shah, R. K., and Aung, W., *Handbook of Single-Phase Convective Heat Transfer*. 1987, New York, NY: John Wiley & Sons.
86. Dittus, F.W., and Boelter, L. M. K. *Heat Transfer in Automobile Radiators of the Tubular Type*. in *Publications on Engineering*. 1930. University of California, Berkeley.
87. Hausen, H., *Neue Gleichungen für die Wärmeübertragung bei Freier oder Erzwungener Strömung*. Allg. Warmetchn., 1959. **9**: p. 75-79.

88. Gnielinski, V., *New Equations for Heat and Mass Transfer in Turbulent Pipes and Channels Flow*. Int. Chem. Eng., 1976(16): p. 359-367.
89. Sieder, E.N., and G. E. Tate, *Heat Transfer and Pressure Drop of Liquids in Tubes*. Ind. Eng. Chem., 1936. **28**: p. 1429-1435.
90. Bhadani, M.M. and N.G.T. Ludlow, *Precipitation of Sub-Micron Dust in Still Air by Cloud-Size Water Droplets*. Nature, 1961. **190**(4780): p. 974-976.
91. Hetsroni, G. and M. Sokolov, *Distribution of Mass, Velocity, and Intensity of Turbulence in a Two-Phase Turbulent Jet*. Journal of Applied Mechanics, 1971. **38**(2): p. 315-327.
92. Rogers, C.B. and J.K. Eaton, *The effect of small particles on fluid turbulence in a flat-plate, turbulent boundary layer in air*. Physics of Fluids A: Fluid Dynamics, 1991. **3**(5): p. 928-937.
93. Pan, Y. and S. Banerjee, *Numerical simulation of particle interactions with wall turbulence*. Physics of Fluids, 1996. **8**(10): p. 2733-2755.
94. Elghobashi, S.E. and T.W. Abou-Arab, *A two-equation turbulence model for two-phase flows*. Physics of Fluids, 1983. **26**(4): p. 931-938.
95. Rizk, M.A. and S.E. Elghobashi, *The motion of a spherical particle suspended in a turbulent flow near a plane wall*. Physics of Fluids, 1985. **28**(3): p. 806-817.
96. Gore R, A., *Effect of particle size on modulating turbulent intensity*. Int. J. Multiphase Flow, 1989. **15**(2): p. 279-285.
97. Rashidi, M., G. Hetsroni, and S. Banerjee, *Particle-turbulence interaction in a boundary layer*. International Journal of Multiphase Flow, 1990. **16**(6): p. 935-949.

98. Cherkasova, A.S. and J.W. Shan, *Particle Aspect-Ratio and Agglomeration-State Effects on the Effective Thermal Conductivity of Aqueous Suspensions of Multiwalled Carbon Nanotubes*. Journal of Heat Transfer, 2010. **132**(8): p. 082402-11.
99. Chen, H., Y. Ding, and A. Lapkin, *Rheological behaviour of nanofluids containing tube / rod-like nanoparticles*. Powder Technology, 2009. **194**(1-2): p. 132-141.
100. Chen, H., Ding, Y., Lapkin, A., Fan, X., *Rheological behaviour of ethylene glycol-titanate nanotube nanofluids*. Journal of Nanoparticle Research, 2009. **11**(6): p. 1513-1520.
101. Nelson, I.C., D. Banerjee, and R. Ponnappan, *Flow Loop Experiments Using Polyalphaolefin Nanofluids*. Journal of Thermophysics and Heat Transfer, 2009. **23**(4): p. 752-761.
102. Yang, Y., Grulke, E. A., Zhang, Z. G., Wu, G. F., *Thermal and rheological properties of carbon nanotube-in-oil dispersions*. Journal of Applied Physics, 2006. **99**(11).
103. Shaikh, S., K. Lafdi, and R. Ponnappan, *Thermal conductivity improvement in carbon nanoparticle doped PAO oil: An experimental study*. Journal of Applied Physics, 2007. **101**(6).
104. Liu, D. and L.Y. Yu, *Single-Phase Thermal Transport of Nanofluids in a Minichannel*. Journal of Heat Transfer-Transactions of the Asme, 2011. **133**(3).
105. Shah, R.K., and London, A. L., *Laminar Flow Forced Convection in Ducts*. Suppl. 1, Adv. Heat Transfer, Academic Press, 1978.

106. Tao, Y.G., W.K. den Otter, and W.J. Briels, *Kayaking and wagging of rods in shear flow*. Physical Review Letters, 2005. **95**(23).
107. Tao, Y.G., W.K. den Otter, and W.J. Briels, *Periodic orientational motions of rigid liquid-crystalline polymers in shear flow*. Journal of Chemical Physics, 2006. **124**(20).
108. Tao, Y.G., W.K. den Otter, and W.J. Briels, *Kayaking and wagging of liquid crystals under shear: Comparing director and mesogen motions*. Epl, 2009. **86**(5).
109. Tao, Y.G., W. K. den Otter, Dhont, J. K. G. and W. J. Briels , *Brownian dynamics simulations of the self- and collective rotational diffusion coefficients of rigid long thin rods*. Journal of Chemical Physics, 2005. **122**(24).
110. Jeffery, G.B., *The Motion of Ellipsoidal Particles Immersed in a Viscous Fluid*. Proc. R. Soc. Lond. A, 1922. **102**(715): p. 18.
111. Liu, D., Garimella, S. V., *Electromechanical Actuation of Nanofluids*, in *Nanoparticles: Synthesis, Characterization and Applications*, R.S. Chaughule, Ramanujan, R. V. , Editor. 2009, American Scientific Publishers: Los Angeles. p. 32.
112. Liu, D. and Yu, L., *Single-Phase Thermal Transport of Nanofluids in a Minichannel*. Journal of Heat Transfer-Transactions of the Asme, 2011. **133**(3).
113. Yu, L., Liu, D., Botz, F., *Laminar convective heat transfer of alumina-polyalphaolefin nanofluids containing spherical and non-spherical nanoparticles*. Experimental Thermal and Fluid Science, 2012. **37**(February): p. 11.

114. Green, C.E., A.G. Fedorov, and Y.K. Joshi, *Scaling Analysis of Performance Tradeoffs in Electronics Cooling*. Ieee Transactions on Components and Packaging Technologies, 2009. **32**(4): p. 868-875.
115. Saylor, J.R., Barcohen, A., Lee, T. Y., Simon, T. W., Tong, W., Wu, P. S., *Fluid selection and property effects in single-phase and 2-phase immersion cooling*. IEEE Transactions on Components Hybrids and Manufacturing Technology, 1988. **11**(4): p. 557-565.
116. Li, J. and C. Kleinstreuer, *Thermal performance of nanofluid flow in microchannels*. International Journal of Heat and Fluid Flow, 2008. **29**(4): p. 1221-1232.
117. Nguyen, C.T., Desgranges, F., Galanisc, N., Roy, G., Mare, T., Boucher, S., Mintsa, H. A., *Viscosity data for Al<sub>2</sub>O<sub>3</sub>-water nanofluid-hysteresis: is heat transfer enhancement using nanofluids reliable?* International Journal of Thermal Sciences, 2008. **47**(2): p. 103-111.
118. Namburu, P.K., Kulkarni, D. P., Dandekar, A., Das, D. K., *Experimental investigation of viscosity and specific heat of silicon dioxide nanofluids*. Micro & Nano Letters, 2007. **2**(3): p. 67-71.
119. Prasher, R., Song, D., Wang J., Phelan, P., *Measurements of nanofluid viscosity and its implications for thermal applications*. Applied Physics Letters, 2006. **89**(13).
120. Ellsworth, M.J., *Comparing liquid coolants from both a thermal and hydraulic perspective*. Electronics Cooling, 2006(August).

121. Bergman, T.L., *Effect of reduced specific heats of nanofluids on single phase, laminar internal forced convection*. International Journal of Heat and Mass Transfer, 2009. **52**(5-6): p. 1240-1244.
122. Singh, P.K., Anoop, K. B., Sundararajan, T., Das, Sarit K., *Entropy generation due to flow and heat transfer in nanofluids*. International Journal of Heat and Mass Transfer, 2010. **53**(21-22): p. 4757-4767.
123. Yeh, L.T., Chu R. C., *Thermal Management of Microelectronic Equipment*. 2002, New York: ASME Press.
124. Mouromtseff, I.E., *Water and forced-air cooling of vacuum tubes*. Proceedings of the Institute of Radio Engineers, 1942. **30**: p. 15.
125. Gherasim, L., Roy, Gilles, Nguyen, C. T., Dinh, V., *Heat transfer enhancement and pumping power in confined radial flows using nanoparticle suspensions (nanofluids)*. International Journal of Thermal Sciences, 2011. **50**(3): p. 369-377.
126. Ho, C.J., et al., *On laminar convective cooling performance of hybrid water-based suspensions of Al(2)O(3) nanoparticles and MEPCM particles in a circular tube*. International Journal of Heat and Mass Transfer, 2011. **54**(11-12): p. 2397-2407.
127. Ho, C.J., Huang, J. B., Tsai, P. S., Yang, Y. M., *Water-based suspensions of Al(2)O(3) nanoparticles and MEPCM particles on convection effectiveness in a circular tube*. International Journal of Thermal Sciences, 2011. **50**(5): p. 736-748.
128. Garg, J., Poudel, B., Chiesa, M., Gordon, J. B., Ma, J. J., Wang, J. B., Ren, Z. F., Kang, Y. T., Ohtani, H., Nanda, J., McKinley, G. H., Chen, G., *Enhanced thermal*

- conductivity and viscosity of copper nanoparticles in ethylene glycol nanofluid.* Journal of Applied Physics, 2008. **103**(7).
129. Timofeeva, E.V., Smith, D. S., Yu W., France, D. M., Singh, D., Routbort, J. L, *Particle size and interfacial effects on thermo-physical and heat transfer characteristics of water-based alpha-SiC nanofluids.* Nanotechnology, 2010. **21**(21).
130. Chein, R. and J. Chuang, *Experimental microchannel heat sink performance studies using nanofluids.* International Journal of Thermal Sciences, 2007. **46**(1): p. 57-66.
131. Pantzali, M.N., A.A. Mouza, and S.V. Paras, *Investigating the efficacy of nanofluids as coolants in plate heat exchangers (PHE).* Chemical Engineering Science, 2009. **64**(14): p. 3290-3300.
132. Liu, D. and S.V. Garimella, *Analysis and optimization of the thermal performance of microchannel heat sinks.* International Journal of Numerical Methods for Heat & Fluid Flow, 2005. **15**(1): p. 7-26.
133. Das, S.K., N. Putra, and W. Roetzel, *Pool boiling characteristics of nano-fluids.* International Journal of Heat and Mass Transfer, 2003. **46**(5): p. 851-862.
134. Das, S.K., N. Putra, and W. Roetzel, *Pool boiling of nano-fluids on horizontal narrow tubes.* International Journal of Multiphase Flow, 2003. **29**(8): p. 1237-1247.
135. Das, S., G. Prakash Narayan, and A. Baby, *Survey on nucleate pool boiling of nanofluids: the effect of particle size relative to roughness.* Journal of Nanoparticle Research, 2008. **10**(7): p. 1099-1108.

136. Narayan, G.P., K.B. Anoop, and S. K. Das, *Mechanism of enhancement/deterioration of boiling heat transfer using stable nanoparticle suspensions over vertical tubes*. Journal of Applied Physics, 2007. **102**(7): p. 074317-7.
137. Chopkar, M., Das, A., Manna, I., Das, P., *Pool boiling heat transfer characteristics of  $ZrO_2$ -water nanofluids from a flat surface in a pool*. Heat and Mass Transfer, 2008. **44**(8): p. 999-1004.
138. Vassallo, P., R. Kumar, and S. D'Amico, *Pool boiling heat transfer experiments in silica-water nano-fluids*. International Journal of Heat and Mass Transfer, 2004. **47**(2): p. 407-411.
139. Wen, D. and Y. Ding, *Experimental investigation into the pool boiling heat transfer of aqueous based gamma-alumina nanofluids*. Journal of Nanoparticle Research, 2005. **7**(2-3): p. 265-274.
140. Bang, I.C. and S. Heung Chang, *Boiling heat transfer performance and phenomena of  $Al_2O_3$ -water nano-fluids from a plain surface in a pool*. International Journal of Heat and Mass Transfer, 2005. **48**(12): p. 2407-2419.
141. Milanova, D. and R. Kumar, *Role of ions in pool boiling heat transfer of pure and silica nanofluids*. Applied Physics Letters, 2005. **87**(23): p. 233107-3.
142. Milanova, D. and R. Kumar, *Heat Transfer Behavior of Silica Nanoparticles in Pool Boiling Experiment*. Journal of Heat Transfer, 2008. **130**(4): p. 042401-6.
143. Liu, Z.-h., J.-g. Xiong, and R. Bao, *Boiling heat transfer characteristics of nanofluids in a flat heat pipe evaporator with micro-grooved heating surface*. International Journal of Multiphase Flow, 2007. **33**(12): p. 1284-1295.

144. Lee, J. and I. Mudawar, *Assessment of the effectiveness of nanofluids for single-phase and two-phase heat transfer in micro-channels*. International Journal of Heat and Mass Transfer, 2007. **50**(3-4): p. 452-463.
145. Park, K.-J. and D. Jung, *Enhancement of nucleate boiling heat transfer using carbon nanotubes*. International Journal of Heat and Mass Transfer, 2007. **50**(21–22): p. 4499-4502.
146. Xue, H.S., Fan, J. R., Hu, Y. C., Hong, R. H., Cen, K. F., *The interface effect of carbon nanotube suspension on the thermal performance of a two-phase closed thermosyphon*. Journal of Applied Physics, 2006. **100**(10): p. 104909-5.
147. H. Kim, J.K.a.M.K., *Experimental study on CHF characteristics of water-TiO<sub>2</sub> nano-fluids*. Nuclear engineering and technology, 2006. **38**(61).
148. Kim, S.J., Bang, I. C., Buongiorno, J., Hu, L. W., *Effects of nanoparticle deposition on surface wettability influencing boiling heat transfer in nanofluids*. Applied Physics Letters, 2006. **89**(15).
149. Kim, S.J., Bang, I. C., Buongiorno, J., Hu, L. W., *Surface wettability change during pool boiling of nanofluids and its effect on critical heat flux*. International Journal of Heat and Mass Transfer, 2007. **50**(19-20): p. 4105-4116.
150. Kim, S.J., McKrell, T., Buongiorno, J., Hu, L. W., *Alumina Nanoparticles Enhance the Flow Boiling Critical Heat Flux of Water at Low Pressure*. Journal of Heat Transfer, 2008. **130**(4): p. 044501-3.
151. Sefiane, K., *On the role of structural disjoining pressure and contact line pinning in critical heat flux enhancement during boiling of nanofluids*. Applied Physics Letters, 2006. **89**(4): p. 044106-3.

152. You, S.M., J.H. Kim, and K.H. Kim, *Effect of nanoparticles on critical heat flux of water in pool boiling heat transfer*. Applied Physics Letters, 2003. **83**(16): p. 3374-3376.
153. Xue, H.S., Fan, J. R., Hong, R. H., Hu, Y. C., *Characteristic boiling curve of carbon nanotube nanofluid as determined by the transient calorimeter technique*. Applied Physics Letters, 2007. **90**(18): p. 184107-3.
154. Liu, D. and S.V. Garimella, *Flow Boiling Heat Transfer in Microchannels*. Journal of Heat Transfer, 2007. **129**(10): p. 1321-1332.
155. Steinke, M.E. and S.G. Kandlikar, *Control and effect of dissolved air in water during flow boiling in microchannels*. International Journal of Heat and Mass Transfer, 2004. **47**(8-9): p. 1925-1935.
156. Kim, S.J., et al., *Experimental Study of Flow Critical Heat Flux in Alumina-Water, Zinc-Oxide-Water, and Diamond-Water Nanofluids*. Journal of Heat Transfer-Transactions of the Asme, 2009. **131**(4).
157. Khandekar, S., Y.M. Joshi, and B. Mehta, *Thermal performance of closed two-phase thermosyphon using nanofluids*. International Journal of Thermal Sciences, 2008. **47**(6): p. 659-667.
158. Coursey, J.S. and J. Kim, *Nanofluid boiling: The effect of surface wettability*. International Journal of Heat and Fluid Flow, 2008. **29**(6): p. 1577-1585.
159. Ahn, H.S., Kim, H., Jo, H., Kang, S., Chang, W., Kim, M. H., *Experimental study of critical heat flux enhancement during forced convective flow boiling of nanofluid on a short heated surface*. International Journal of Multiphase Flow, 2010. **36**(5): p. 375-384.

160. Liu, Z.H. and Y.H. Qiu, *Boiling heat transfer characteristics of nanofluids jet impingement on a plate surface*. Heat and Mass Transfer, 2007. **43**(7): p. 699-706.
161. Sheikhhbahai, M., M. Nasr Esfahany, and N. Etesami, *Experimental investigation of pool boiling of Fe<sub>3</sub>O<sub>4</sub>/ethylene glycol–water nanofluid in electric field*. International Journal of Thermal Sciences, (0).
162. Hsu, Y.Y., *On the Size Range of Active Nucleation Cavities on a Heating Surface*. Journal of Heat Transfer, 1962. **84**(3): p. 207-213.
163. Liu, D., P.-S. Lee, and S.V. Garimella, *Prediction of the onset of nucleate boiling in microchannel flow*. International Journal of Heat and Mass Transfer, 2005. **48**(25–26): p. 5134-5149.
164. Davis, E.J. and G.H. Anderson, *The incipience of nucleate boiling in forced convection flow*. AIChE Journal, 1966. **12**(4): p. 774-780.
165. Kakac, S. and B. Bon, *A Review of two-phase flow dynamic instabilities in tube boiling systems*. International Journal of Heat and Mass Transfer, 2008. **51**(3–4): p. 399-433.
166. Carey, V.P., *Liquid-Vapor Phase-Change Phenomena*. 1992, New York, NY: Talyor & Francis.
167. Karsli, S., M. Yilmaz, and O. Comakli, *The effect of internal surface modification on flow instabilities in forced convection boiling in a horizontal tube*. International Journal of Heat and Fluid Flow, 2002. **23**(6): p. 776-791.
168. Boure, J.A., A.E. Bergles, and L.S. Tong, *Review of two-phase flow instability*. Nuclear Engineering and Design, 1973. **25**(2): p. 165-192.

169. Ledinegg, M., *Instabilitat der Stromung bei Naturlichen und Zwangumlauf*.  
 Warme 1938. **61**: p. 891-899.
170. S. G. Kandlikar, V.K.D., Masahiro Shoji *Handbook of Phase Change: Boiling  
 and Condensation*. 1999, Philadelphia, PA: Talyor & Francis.
171. Ding, Y., S. Kakaç, and X.J. Chen, *Dynamic instabilities of boiling two-phase  
 flow in a single horizontal channel*. Experimental Thermal and Fluid Science,  
 1995. **11**(4): p. 327-342.
172. Kakac, S., *Two-Phase Flow Instabilities in Boiling Systems: Summary and  
 Review*. METUJ. Pure Appl. Sci., 1985. **18**(2).
173. L. G. Neal, S.M.Z.a.R.W.W., *The Mechanisms of Hydrodynamic Instabilities in  
 Boiling Channel*, in *EURATOM Report*. 1967: Eindhoven.
174. Maulbetsch, J.S., and Griffith, P., *System Induced Instabilities in Forced  
 Convection Flow with Subcooled Boiling*, in *3rd International Heat Transfer  
 Conference*. 1966: Chicago, IL. p. 247.
175. Stenning, A.H.a.V., T. N. *Flow Oscillation Modes in Forced Convection Boiling*.  
 in *Procedings of Heat Transfer and Fluid Mechanics Institute*, . 1965. Stanford  
 University Press.
176. Zhang, T., Wen, John T., Peles, Y., Catano, J., Zhou, R., Jensen, M., *Two-phase  
 refrigerant flow instability analysis and active control in transient electronics  
 cooling systems*. International Journal of Multiphase Flow, 2011. **37**(1): p. 84-97.
177. Mamoru Ozawa, S.N., Seikan Ishigai, Yuhsuke Mizuta and Hiroaki Tarui, *Flow  
 Instabilities in Boiling Channels: Part I Pressure Drop Oscillation*. Bulletin of  
 the JSME, 1979. **22**(170).

178. Liu, H., *Pressure-drop type and thermal oscillations in convective boiling systems*, in *Mechanical Engineering*. 1993, University of Miami: Miami.

